EXPERIMENTAL INVESTIGATION OF HIGH–SPEED ROTARY BELL ATOMIZATION BY LASER–OPTICAL METHODS

Zur Erlangung des akademischen Grades eines
Dr.-Ing.
von der Fakultät Bio- und Chemieingenieurwesen
der Technischen Universität Dortmund
genehmigte Dissertation

vorgelegt von
M.Sc. Lutz Gödeke
aus
Datteln

Tag der mündlichen Prüfung: 13. Februar 2023
1. Gutachter: Prof. Dr.-Ing. Peter Ehrhard
2. Gutachter: Prof. Dr.-Ing. David W. Agar

Dortmund 2023

Abstract

The coating process in the modern automotive industry is usually implemented using high-speed rotary atomizers. The requirements for coating qualities are on the one hand of a technical nature, on the other hand they have to satisfy the subjective perception of the consumer. For the application, it is therefore of great interest to fathom and understand the physical dependencies between the applied coating layer, the selectable process parameters and material properties by means of fundamental research. This enables targeted product development that meets financial, environmental and quality requirements while economizing on material during application. Within the scope of the present work, the basic theoretical background for the three topics of coating properties, measurement technology, as well as data preparation and processing will be evaluated in detail. The focus lies on highlighting necessary adjustments in the methodology and particularities during measurement, application and data processing. For this purpose, the experimental procedure including the derived methods is presented in detail. The results are then displayed and discussed with the help of mathematical modeling approaches with respect to their special characteristics. Finally, a comprehensive description of the relevant error sources and their individual influences is given.

Zusammenfassung

Der Lackierprozess in der heutigen, modernen Automobilindustrie wird üblicherweise unter Verwendung von Hochrotationszerstäubern umgesetzt. Die Anforderungen an die Qualität des Lackes sind hierbei einerseits von technischer Natur, andersseits müssen sie dem subjektiven Empfinden des Endkunden genügen. Für die Applikation ist es somit von großem Interesse, die Zusammenhänge zwischen der aufgebrachten Lackschicht, den wählbaren Prozessparametern und Materialeigenschaften, durch Grundlagenforschung zu ergründen und zu verstehen. Hierdurch wird unter Einsparung von Material während der Applikation gezielte Produktentwicklung ermöglicht, die finanzielle, umwelttechnische und qualitative Vorgaben erfüllt. Im Rahmen der vorliegenden Arbeit werden die grundlegenden theoretischen Hintergründe für die drei Themenbereiche Lackeigenschaften, Messtechnik und Datenaufbereitung/-verarbeitung im Detail betrachtet. Der Schwerpunkt liegt hierbei darauf, notwendige Anpassungen in der Methodik und Besonderheiten während der Messung, Applikation und der Datenverarbeitung hervorzuheben. Hierzu wird das experimentelle Vorgehen inklusive der daraus abgeleiteten Methoden genau vorgestellt. Die Ergebnisse werden anschließend mit Hilfe von mathematischen Modellansätzen in Bezug auf ihre Besonderheiten dargestellt und diskutiert. Abschließend erfolgt eine umfangreiche Beschreibung der relevanten Fehlerquellen und ihren individuellen Einflüssen.

To my beloved Jana

To my family and my friends

For those that were lost along the journey, not to be forgotten.

Acknowledgements

First of all, I would like to thank the everyone in the fluid mechanics group for the pleasant, productive environment and the numerous professional discussions. Thank you Ingo, Friedrich and Tatjana for the support and help throughout the years. Thank you Christian and Jayotpaul, for being simply awesome roomates and discussion partners. Thank you Tim, Konrad and Peter L., for guiding me through my first years and always having new ideas on how to approach problems. Thank you Ann Kathrin and Sabrina, for your understanding and trust, besides the fluid mechanical topics.

Thank you all, for changing my perspective on what really matters.

The entirety of the project would have taken many different directions if it were not for my dear collaboration partner, now Dr.-Ing., Walter Oswald.

Thank you Peter for being my mentor, for giving me the possibility to begin and end this project, for the trust, your expert supervision of this thesis and guidance throughout the project. Thank you for your patience.

My special thanks go to Prof. Dr. Norbert Willenbacher for several productive discussions and his expert opinion, Prof. Dr. Markus Thommes and Prof. Dr.-Ing. Norbert Kockmann for their willingness to supervise multiple graduation theses.

Furthermore, I want to thank Georg Wigger and Dr. Daniel Briesenick for the encompassing support, BASF Coatings GmbH for initiating this investigation and BASF SE for allocating the material, as well as the RACE staff – Salam, Florian, Marc, Marco – and surely Falco, for enabling the experimental work.

I would like to thank all my students for the open, helpful and friendly atmosphere, all along their contributions.

Table of contents

1

Introduction

1.1 Automotive painting in industry

Modern car paint serves as leveler, corrosivity inhibitor, colouring and visual effect, as well as outer protection layer against UV-light, mechanical and direct chemical influences. All this happens within thin layers that accumulate to a total thickness of about $80 - 100\ \mu m$, about as thick as a human hair (BASF SE, 2021).

During the last years, the industry has evolved to incorporate nearly exclusively waterborne paints for fillers, base coats and partially for clear coats. While extensive research is being made at all times to further improve the process, the losses due to solvent evaporation, overspray and, therefore, consecutive air filtering are immense. The potential for economic and environmental improvements is promising (Wigger and Briesenick, 2017).

State-of-the-art coatings in the automotive industry can essentially be reduced to the following components (Streitberger and Goldschmidt, 2018):

- film formers: mostly synthetic resins that cross-link under different chain or polymerization reactions to form a solid film.
- solvents: forms the carrier material of all important components and evaporates after painting during baking and physical drying.

- pigments and fillers: pigments give the paint its characteristic color and other fillers such as fine solid aluminum flakes give the paint a metallic shine.
- additives: various substances such as plasticizers or surface roughening agents are added to produce certain properties.

It is of note that research and development may change the composition and the overlap within the different sectors displayed in figure 1.1 below.

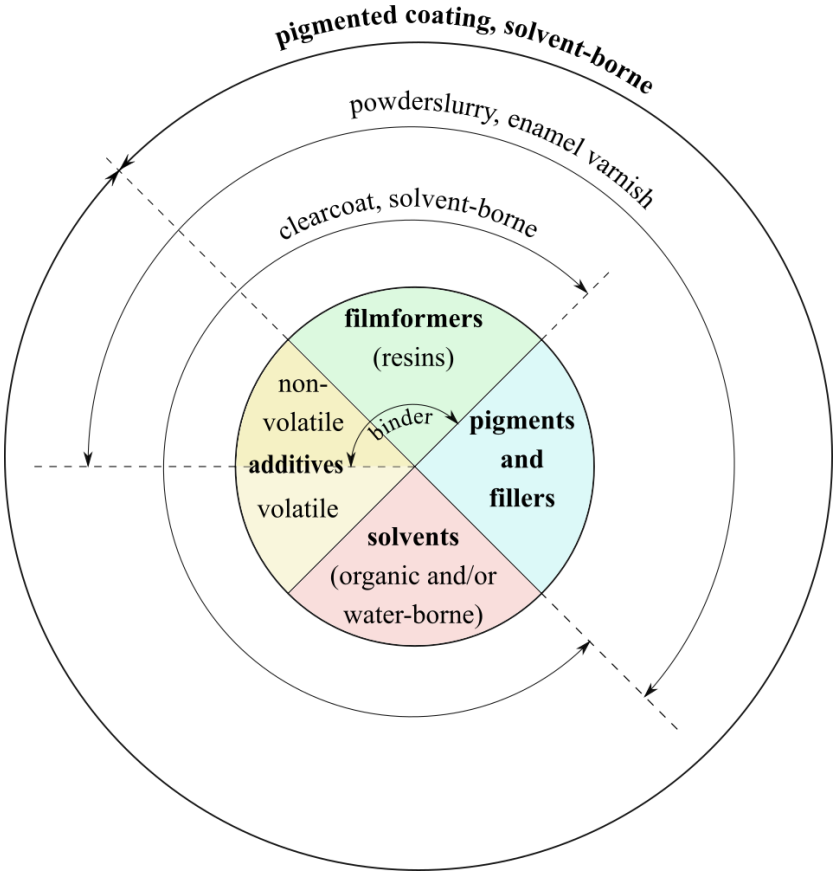

Figure 1.1: Composition of modern coating types (Streitberger and Goldschmidt, 2018)

Some of the individual components, such as synthetic resins, already exhibit non-Newtonian behaviour as pure substances. The final coating material usually is a suspension of various, partly non-Newtonian liquids with different

amounts of solid particles. This results in a rheological behavior that has to take into account shear and strain rates, as well as multi–disperse particle–fluid interactions.

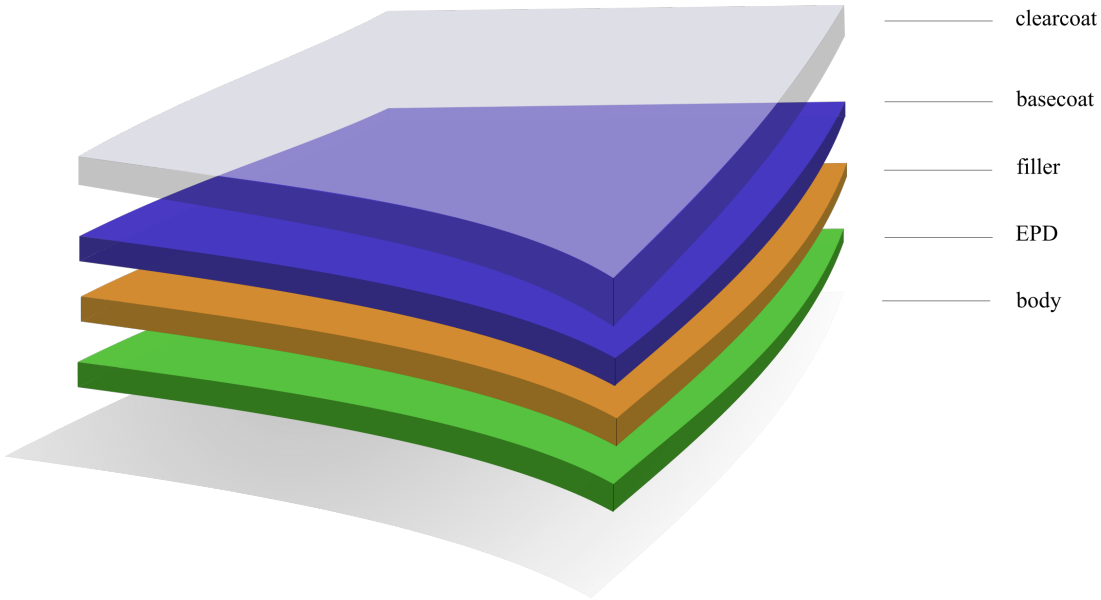

Figure 1.2: Structure of modern multi-layer automotive coatings (BASF SE, 2021)

The structure of an automotive series paint job usually consists of four paint layers. The different paint layers are applied one after the other. After the application of a paint layer, depending on the process, the paint is rested for a sufficient flash–off time under ambient conditions (the solvent evaporates) or directly baked in the oven (the solvent evaporates and resins cross-link chemically). The four layers of a total coating consist essentially of (Streitberger and Goldschmidt, 2018):

- Electrophoretic deposition (EPD): first coating applied by dip coating. Hard-to-reach areas are easily reached by dipping. It mainly acts as corrosion protection.
- Filler: applied by means of rotary atomization. It compensates for unevenness and provides mechanical strength.
- Base coat: applied by means of rotary atomization. Added color pigments and effect materials, such as aluminum flakes, provide the desired appearance. Most modern base coats are water-borne.

- Clear coat: the final layer of paint is likewise being applied by rotary atomization. The transparent clear coat is demanded to have high gloss and, in combination with the base coat, provide an attractive visual appearance.

The quality of a finished coating is evaluated primarily on the basis of its resistance, appearance and freedom from defects. As human eyes are different from one another, the appearance is influenced by subjective factors. In order to minimize this subjectivity, a sophisticated measurement tool is used in industry to quantify surface characteristics and light scattering performance (section 1.3). Errors that appear regularly are briefly described in the following passage, based upon their origin and how they can be avoided and/or repaired.

1.2 Errors during painting

The aforementioned painting errors that occur during the industrial process are briefly described regarding their appearance and their origin. It applies to all repair work to be avoided as far as possible, since remedy is generally time and cost intensive.

Orange Peel

The so-called orange-peel effect causes the final paint texture to resemble the skin of the well-known citrus fruit. This effect may be desirable for certain applications, but overall this is considered a paint defect for automotive coatings. The waviness of the final surface layer can be caused by different effects, namely Marangoni flows, during application, flash-off and oven drying.

Saranjam et al. propose a self-sustaining Marangoni flow pattern, driven by local solvent concentration differences, hence, surface tension differences at the free surface of the liquid film (see figure 1.3 and Saranjam et al., 2016). These local solvent concentration differences can be caused by pre–atomization mixing irregularities and/or separation effects inside the spray cone resulting in solvent–enriched film regions.

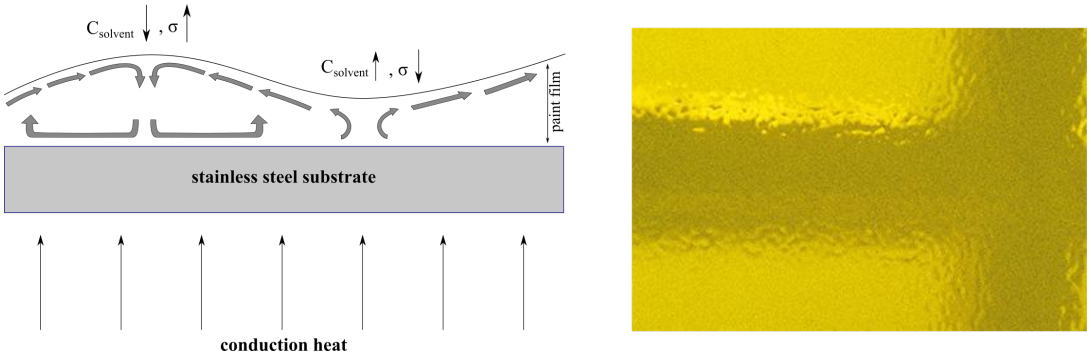

Figure 1.3: Schematic presentation of Marangoni flow pattern and the resulting orange peel paint appearance (Saranjam et al., 2016)

Bubble entrapment, popping and pinholes

Small bubbles can form in the wet film due to various mechanisms (e.g. drop impact (Burzinski, 2018; Grünendahl, 2017), see chapter (2.8) and solvent evaporation (Saranjam and Chandra, 2016)). After the initially undisturbed evaporation from the liquid film to the surrounding gas phase, a solid skin grows on the paint surface, severely hindering the solvent evaporation. Accordingly the solvent evaporates into small bubbles that are unable to escape through the solid skin (solvent cooking, figure 1.4). These entrapped bubbles tend to swell during oven drying and in some cases rise to the top and burst open near the film surface. The resulting cavities are easily visible to the human eye as defects in the paint film that dramatically distort the appearance. Even when not burst, the bubble distorts the surface evenness as it forms a small meniscus in its proximity. Substrate bound bubbles similarly function as a target for evaporating solvent. The formation of bubbles by droplet impact can be minimized by selecting adapted application parameters. Evaporation of solvent into existing micro-bubbles can be minimized by maintaining ideal film thicknesses and appropriate flash–off times for the selected hardeners and solvents. Both these values are typically kept secret as experiential values.

In the case of burst substrate–bound bubbles, the underlying layer is locally exposed and, in addition to optical defects, is more susceptible to corrosion (figure 1.5). From a technical point of view, these are not classic pinholes, which can appear due to substrate surface–irregularities (e.g. cracks), but their result-

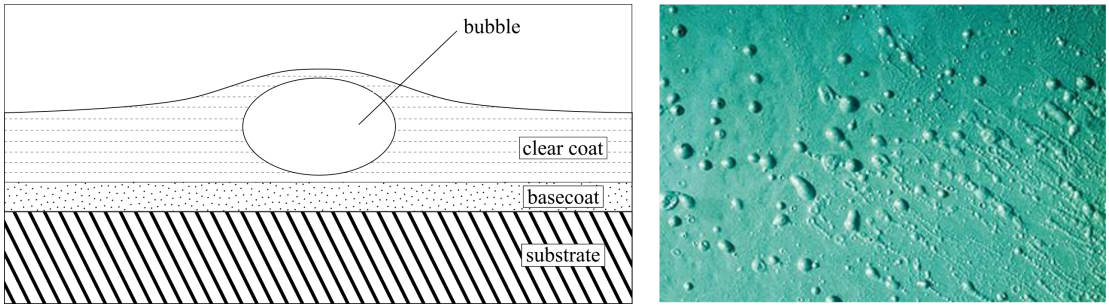

Figure 1.4: Schematic presentation of solvent cooking and real photographs (Glasurit, 2021). Trapped bubbles in proximity of the paint surface distort the appearance and need to be repaired.

ing effect on the paint quality is essentially identical. Sufficient post-treatment of burst bubbles close to the surface and sufficient flash-off times prevent the formation of pinholes.

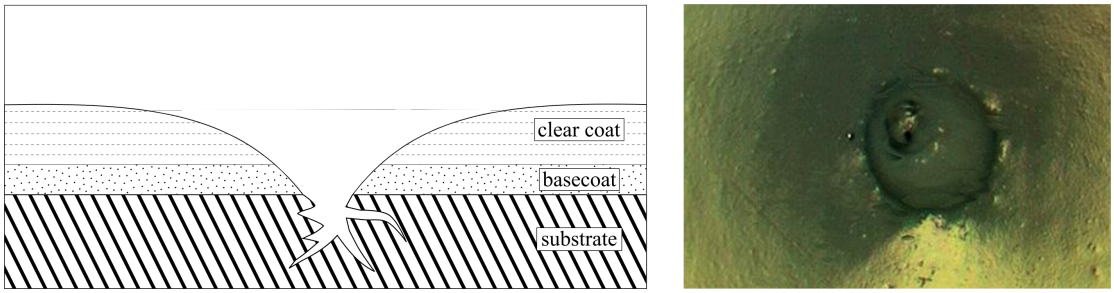

Figure 1.5: Schematic presentation of pinholes and real photographs (Glasurit, 2021). Substrate bound bubbles burst and expose the layers below. Due to corrosivity issues and optical defects these need to be repaired.

Mottling and cloudiness

The appearance of speckled light/dark areas, sometimes arranged in stripes, in a metallic paint finish is referred to as mottling or clouding. This is caused by a migration of the metallic effect particles to one another, resulting in areas with increased and decreased local particle density in the film, thus darker cloud–like areas (figure 1.6). Often this is due to uneven material application or previous unevenness of the substrate, which leads to a locally wet film. A subsequent often insufficient flash–off time increases mottling. Ideally, for the

case of parallel aligned flakes, the reflected light is scattered less, creating a visual effect of depth inside the metallic paint.

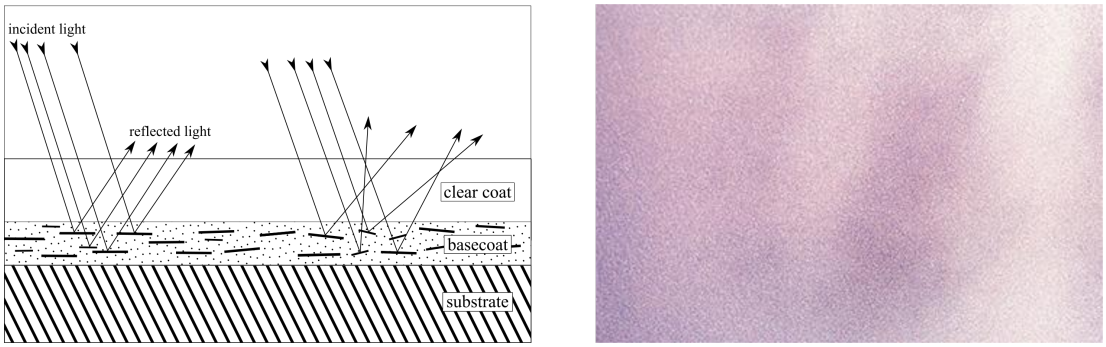

Figure 1.6: Schematic presentation of mottling and real photographs (Glasurit, 2021). Uneven local distribution and insufficient leveling of effect pigments lead to appearance errors.

Overspray

Last on the list is the so-called overspray. This is not a direct painting error in the actual sense of the name but rather droplets that have been deposited incorrectly on surfaces previously painted. This often results in spot discoloration or a changed surface structure. Overspray occurs due to low transfer efficiency (TE) rates and flawed spray patterns, causing undesirable overlap or bad coverage of exposed regions of the substrate. The TE can be improved by optimized atomization and/or paint properties, including electrostatic effects, as well as highly optimized spray patterns with optimal overlap for the spray cone passages as well as sufficient shielding of previously painted areas.

Paint runs

Paint runs occur primarily on vertically aligned body parts. Local film thickness excess in the wet film may lead to paint runs. Gravitational forces outweigh adhesive forces. This may be due to low viscosity or solvent concentration variations, as well as low spray booth ambient temperatures and high humidity, defects in the spray application apparatus (e.g. damaged rotary bell edge) and insufficient flash-off times between wet-in-wet coating application. Remedy can be achieved by sufficient drying and subsequent polishing.

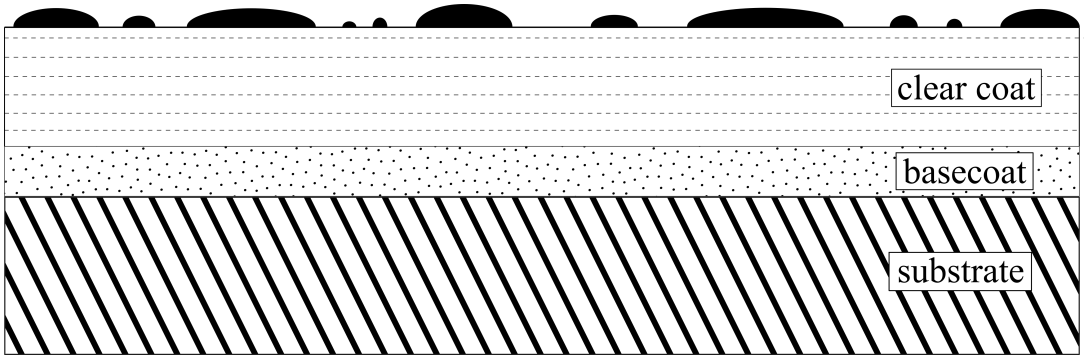

Figure 1.7: Schematic presentation of overspray (Glasurit, 2021). Undesirable deposition of paint on substrate that has been painted or still needs to be painted. Often found in proximity of strongly curved surface structures.

1.3 Challenges and solution approaches

The initial approach to the given investigation is the attempt to correlate experimentally measured characteristic values in the spray cone to fluid properties and process parameters. The underlying physics of the integrated process are to be identified and subsequently used to develop more in-depth understanding, then create fundamental knowledge about the overall process and use this to eventually predict spray properties by modelling the process by means of the definition of dimensionless groups.

These findings are then to be used to refine the development process for new paint types, based upon pigmentation, rheology and applicability. This reduces the costs for trial runs and measurement campaigns immensely, as the needed paint materials are of lower quantity, whilst a more targeted development for specific properties leads to a narrower time frame from an initial idea to a final product.

To acquire reliable droplet sizes and velocities we need to identify and develop suitable non-invasive measurement tools and derive a standardized method to ensure comparability independent of the used devices, of the used materials and of the person performing the data acquisition and evaluation. Due to a wide range of restrictions, the execution of this project has turned out to be much more complicated than anticipated.

At the early stages it is important to get to know the exact behaviour of the phase-Doppler-anemometer (PDA) for opaque automotive paints, which is usually unknown for a given paint and different atomization parameters as the bulk properties do not fully bring forth the fluid properties of the droplets to be measured. The complex refractive index usually is not clearly definable for a solid-liquid disperse system polar/non-polar emulsion. In addition, the added plate–shaped aluminum flakes do interact with light depending on their orientation, from close to total transmission to total reflection. This, coupled with separation effects inside the spray cone lead to difficulties in finding optimal PDA measurement angles, which differ from solid content concentration and kind of pigmentation. Therefore, data rates are highly dependent on the radial location inside the cone, which is further influenced by the air flow in proximity of the socket with the mounted measurement system.

The PDA system (subsection 2.9.2) by Dantec Dynamics is an extension to the existing Dantec 2-D laser-Doppler-anemometer (LDA) owned by the TU Dortmund. The time-shift (TS) device is the AOM Systems Griesheim SpraySpy (subsection 2.9.3). A lack of experience with the TS as a device, both for the handling team and by the producer lead to some evolutionary steps regarding the early version of the SpraySpy. A self build mask (Vetter, 2018) to guard the lenses and further development of the software and the internal settings with AOM enables the definition of a standardized measurement method, to be applied by anyone who went through basic training.

The biggest problem to overcome are temporary limitations for accessing the spray booth, which typically is accessible for a single or double shift without overnight availability for leaving the system at place. Hence, the system has to be set-up and partially removed on a daily basis to unblock the mounting socket for different R&D projects and automotive customer assignments. Coupling this with a highly sensitive laser measurement system which needs to be perfectly aligned (PDA) is destined to be problematic. Preemptive measurements show that the PDA is capable of measuring different opaque paints and analysis of the impacted drops on the substrate shows good agreement with the obtained sizes. Fine-tuning of the TS is performed on results obtained by the PDA. Both devices show good agreement of the obtained droplet

size distributions, with the PDA measuring a larger amount of small diameter droplets due to higher laser power.

During measurement trials and paint component variations to broaden the database for prediction models, as well as to test early hypotheses, several anomalies are occurring. Some paints increase filament length for a very narrow bell speed window, leading to a partial filament ejection with resulting larger droplet sizes and higher deviation from sphericity (Vetter, 2018). Some pigmentations decrease data rates significantly, while variation of rheological aspects usually has no influence on measurability as long as the desired atomization still takes place.

2

Fundamentals and theory

The following chapter will provide the necessary theoretical background for the use of optical measuring methods for the investigation of opaque paint fluids, the necessary simplifications and assumptions, as well as for the subsequent evaluation and analysis.

2.1 General process description

Section 2.1.1, to a large extent, is taken from "Dimensional analysis of droplet size and ligament length during high-speed rotary bell atomization", Goedeke et al., 2021.

The atomization process can be divided into three major portions: (i) the film flow beneath the bell, (ii) the formation of ligaments, leading to their disintegration and the subsequent formation of droplets and finally (iii) the flight phase with the droplet impact on the solid or liquid surfaces. The rotary bell atomizer injects the liquid of density ρ_l and volumetric flow rate $\dot{V}_l$ to the inner side of the spinning bell through a centered channel in the rotating shaft (figure 2.1). The shaping air $\dot{V}_{\text{air}}$ is guided from the inside of the atomizer head onto the bell edge and forces the spray in the direction of the substrate.

A thin film of liquid with thickness δ is formed inside the spinning bell due to strong centrifugal forces. This film emerges from the bell edge, either by directly forming droplets, or as ligaments or different forms of lamellae, that con-

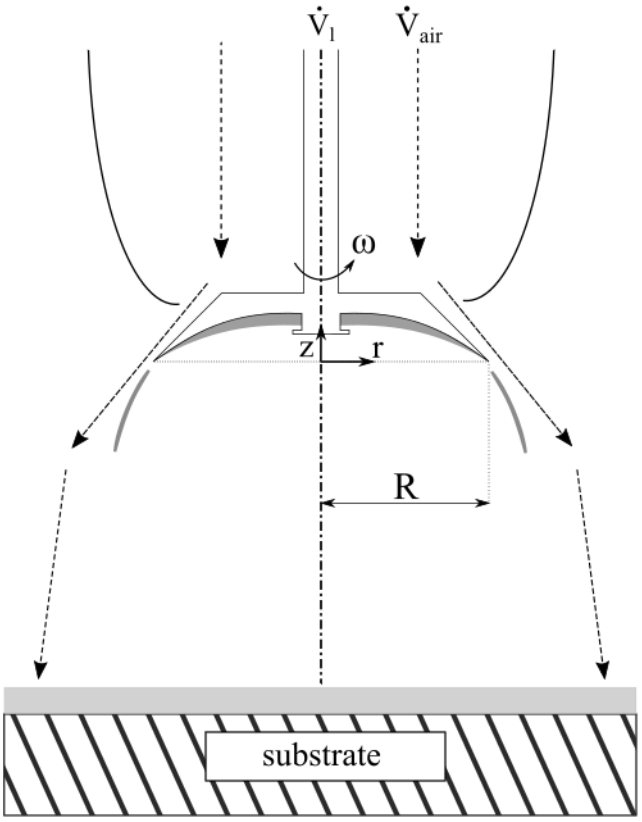

Figure 2.1: Schematic presentation of a typical high–speed rotary bell atomizer head in cross section. The atomizer bell with radius R is located on a rotating shaft (rot. speed ω) which conveys the material to be atomized (flow rate $\dot{V}_l$). Underneath the bell a film of thickness δ is formed, which disintegrates into droplets after emerging from the bell edge as ligaments. To increase transfer to the substrate the shaping air (flow rate $\dot{V}_{\text{air}}$) is blown onto the bell edge.

secutively disintegrate into droplets. The desirable type of droplet formation for most technical processes is ligament disintegration, as it leads to defined droplet size distributions with narrow span. For smooth–edged bells, the ligament properties (ligament spacing, initial diameter $d_{\text{Lig},0}$) are a result of flow instabilities that induce specific flow patterns depending on liquid properties and process parameters. This naturally leads to a partially–chaotic behavior, due to small disturbances in the film. A defined ligament buildup is realized by the use of serrated bells. Small triangular channels (serrations with char-

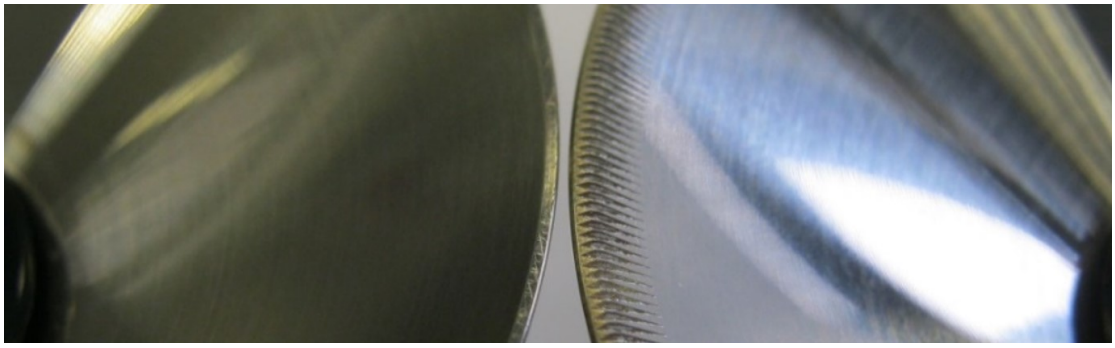

Figure 2.2: Smooth–edged and serrated bell cup. Serrations (characteristic diameter d_{Ser}) force the liquid into defined open channel flows, which then emerge as equidistant ligaments. Depending on liquid flow rate $\dot{V}_l$ and bell speed ω the exact filling level of the serration is unknown.

acteristic diameter d_{Ser}) are cut into the edge of the bell, which force the liquid film to split into a defined number of open channel flows, which consecutively discharge as ligaments (figure 2.2). In contrast to smooth–edged bells, these serrations will maintain a constant number of emerging ligaments, even during the variation of the process parameters within the limits of the ligament disintegration mode. The discharge velocity c_{ax} and ligament diameter d_{Lig} will change according to volumetric flow rate $\dot{V}_l$, bell dimension R and rotational speed ω.

The droplet formation during bell–atomization is a result of disintegrating paint ligaments. Therefore, it is necessary to identify the physical parameters that act at this location correctly for the dimensional analysis. The initial diameter of the ligaments $d_{\mathrm{Lig},0}$ varies weakly with relation to varying process conditions and is approximately of the order of the serration cross–sectional diameter d_{Ser}. In ambient air, the ligament breaks down into droplets, the average size of which is dependent on a critical ligament diameter that can depend on the initial ligament diameter $d_{\mathrm{Lig},0}$ and on the ligament length l_{Lig}.

The liquid volumetric flow rate $\dot{V}_l$ can be written as an axial ligament flow velocity c_{ax} using equation (2.1). Under the assumption of an ideal liquid distribution between the entirety of N different equilateral triangular serrations

and an initially undisturbed rotationally–symmetric ligament, we obtain

$$c_{ax} = \frac{4\dot{V}}{\sqrt{3} \cdot d_{\mathrm{Ser}}^2 \cdot N}. \tag{2.1}$$

This simplified solution yields a good estimate of the initial average velocity inside the ligament, yet does not take into account disturbances of the free surface inside the serration flow or local velocity distributions, as it is based on an integral balance. For constant ambient conditions and moderate bell speed, both gas viscosity η_g and gas density ρ_g can be treated as constant. Surface tension σ_{lg} and liquid density ρ_l are also assumed to be constant. The rheological behavior of the liquid phase is characterized by a shear and an elongational relaxation time ($t_{\lambda_S}, t_{\lambda_E}$) and by shear and elongational viscosities (η_S, η_E) at constant given shear and strain rates ($\dot{\gamma}$,$\dot{\varepsilon}$). Both relaxation times of viscoelastic liquids can be obtained experimentally (Macosko, 1994). The solid content of density ρ_s in the liquid phase is φ_s.

2.1.1 Verification of air density and viscosity at the bell edge

The ambient gas (air) at the edge of the bell interacts with the emerging liquid phase during filament formation. In case of an incompressible gas its density in the vicinity of the bell edge can be treated as constant. Siekmann indicates that incompressibility can be assumed for Mach $M < 0.4$ (Siekmann, 2000). This corresponds to a relative velocity $v_{\mathrm{rel}}(r = R) < 138.6$ m/s ($T = 25°\mathrm{C}$, $p_0 = 1.013$ hPa). As a worst-case estimation of $v_{\mathrm{rel}}(r = R)$, the tangential velocity at the bell edge is calculated and the gas velocity is zero.

From this we obtain

$$v_{\mathrm{rel}}(r = R) = R\omega - v_{\mathrm{air}}(r = R) \cong 221.2 \text{ m/s}. \tag{2.2}$$

For $\omega > 42 \cdot 10^3$ rpm the density change of the gas has to be considered. ANSYS CFX delivers a simplified approximation for the resulting change in local pressure under the following assumptions:

- Navier-Stokes equation, two-dimensional, stationary;
- spinning disk in resting gas;

- no-slip condition at bell edge;
- no external forces.

The maximum pressure difference at the bell edge is estimated at 1090 Pa. Assuming ideal gas law, the density change $\Delta\rho_g$ and the absolute density ρ_g can be calculated (Baehr and Kabelac, 2012) as

$$\Delta\rho_g = \frac{\Delta p \cdot M_g}{R_g \cdot T} \cong 0.0128 \text{ kg/m}^3, \tag{2.3}$$

$$\rho_g = \frac{p_\infty \cdot M_g}{R_g \cdot T} \cong 1.1851 \text{ kg/m}^3, \tag{2.4}$$

$$\frac{\Delta\rho_g}{\rho_g} \cong 1.080\%. \tag{2.5}$$

The relative change in gas density $\frac{\Delta\rho_g}{\rho_g}$ can be expected to be lower than 1.080%, hence the gas can be considered as incompressible and therefore the density remains constant to good approximation. According to Siekmann the viscosity of gas can be considered constant to good approximation for constant T, ρ_g, p (Siekmann, 2000).

2.2 Rheology of automotive paints

Due to the complex mixture of several liquid and solid components interacting on a physical and a chemical level, the rheological characterization of the system is equally difficult. Paint liquids are typically non-Newtonian, with a mostly shear-thinning behaviour to facilitate application and leveling on the substrate surfaces, while relaxation of the shear-thinning effect (thixotropy) helps to diminish undesirable flows, e.g. due to gravity. Added defoamers, stabilizers, pigments and filling materials further impede this characterization. Different thickening agents add visco-elastic behaviour, which is influenced by solid particles of different morphology.

All these effects are highly dependent on the prevailing shear and strain rates during each section of the atomization process. Therefore, typically used measurement methods for rheological characterization, such as rotary viscosimetry or the CaBER (capillary breakup elongational rheometry) device can not be

used to obtain the paint properties during the actual atomization process, as the achievable shear and strain rates are not in the same order of magnitude (Stelter et al., 2000).

A simple approach to estimate the rheological properties of shear-thinning fluids is to combine the power-law viscosity model (Gooch, 2007)

$$\eta = \varsigma \cdot \dot{\gamma}^{B-1} \tag{2.6}$$

with an additional term for the solid particle concentration (φ_s).

The solid content φ_s will be implemented as a dimensionless number after applying dimensional analysis to the analyzed system (see section 2.4). The amplitude is described by ς, B is the power-law exponent. A different approach is carried out by Tratnig by use of the Carreau-Yasuda model, which generally allows for better low-shear modelling (Tratnig et al., 2009). However, as shown in figure 2.3, both approaches deliver good estimates for the high-shear viscosity $\eta_{S,\infty}$.

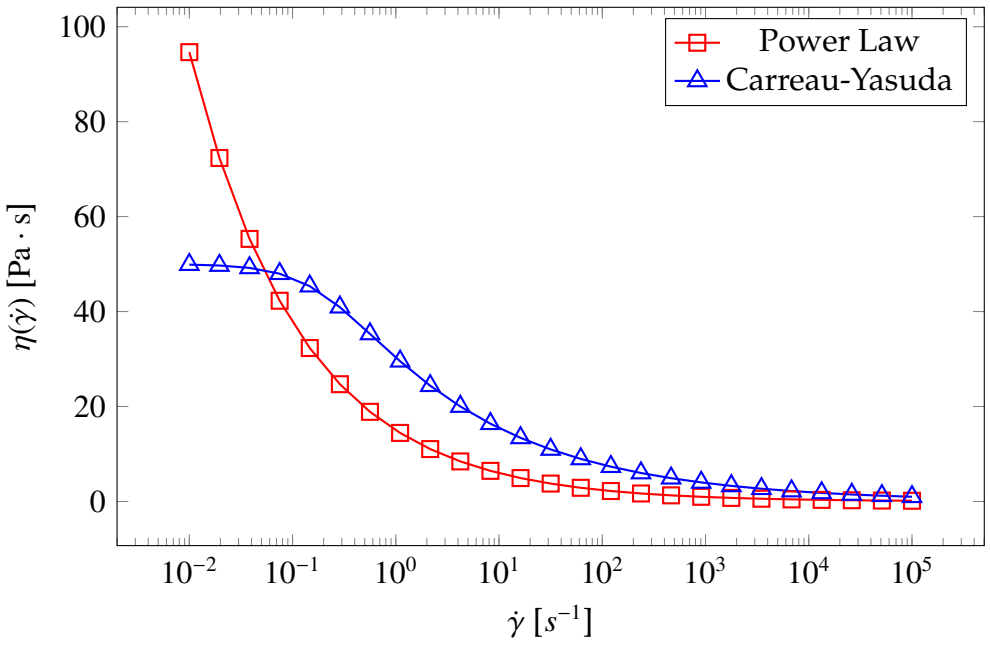

Figure 2.3: Shear-rate dependant viscosity for power law and Carreau-Yasuda fluids.

The temporarily high shear rates and, due to thread extension, high strain rates cannot be easily measured. Accordingly, shear and strain rates have to be estimated from experimental data obtained from high-speed imaging combined with analytical approaches to describe the flow properties (Kuhnhenn et al., 2018). These high-shear and high-strain values are used as reference values for the definition of the disintegration process.

A detailed description of rheological aspects of modern car paints for the given research project can be found in different publications of the partnering research group of the KIT (Oswald et al., 2020; Oswald et al., 2019b; Oswald and Willenbacher, 2019).

2.3 Shear– and strain–rate approximation

Due to the non-Newtonian flow behavior, knowledge about the process–defining shear and strain rates is needed.

2.3.1 Shear-rate estimation

Based upon the steady-state solution for the symmetric stagnation point flow of a Newtonian fluid onto a rotating plate, an estimate for the shear rate as function of bell speed ω and volumetric paint flow rate $\dot{V}_l$ can be derived following the method (Weckerle, 2003):

$$\delta = \sqrt[3]{\frac{3 \cdot \eta_{S,l} \cdot \dot{V}_l}{2 \cdot \pi \cdot R^2 \cdot \omega^2 \cdot \rho_l}}, \tag{2.7}$$

$$u_{\max} = \sqrt[3]{\frac{9 \cdot \omega^2 \cdot \dot{V}_l^2 \cdot \rho_l}{32 \cdot \pi^2 \cdot R \cdot \eta_{S,l}}}. \tag{2.8}$$

The average shear rate $\dot{\gamma}_{\text{avg}}$ inside the film across the film thickness δ at a given location $\vec{r}$ is approximately the quotient of the maximum radial fluid velocity inside the film divided by film thickness, i.e.

$$\dot{\gamma}_{\text{avg}} = u_{\max} \cdot \delta^{-1}. \tag{2.9}$$

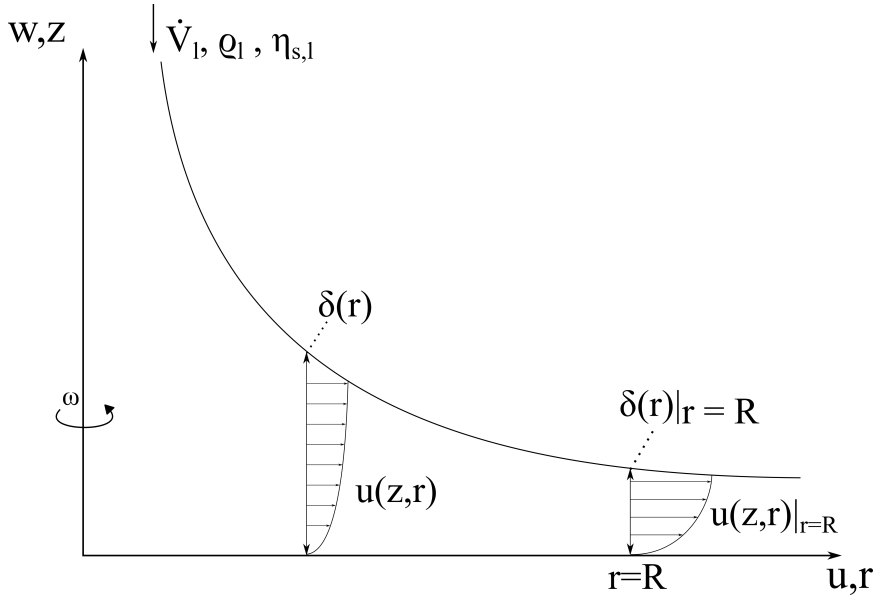

Figure 2.4: Rotationally symmetric stagnation point flow for shear rate approximation, analytical solution, see (Weckerle, 2003).

Equation (2.9) is valid if the velocity on the wall is zero. The solution of the stagnation point flow is valid for the Newtonian case, i.e. for a constant shear viscosity. In the solution carried out here, a constant radial position close to the bell edge is considered, where no temporal change in the flow is present. The shear rate, and thus the viscosity, are constant at this point. Hence, the calculation based upon the proposed approach can be performed for this particular point even for the case of non-Newtonian fluids. The obtained shear rate $\dot{\gamma}_{avg}$ is used to calculate the shear viscosity for a given rheology model. The following loop calculates the average film thickness and the maximum radial flow velocity for a non-Newtonian fluid by iterating until the solution converges (figure 2.5, cf. Illner, 2017 and Weckerle, 2003). For a conventional paint modeled as a power-law fluid (properties and parameters in chapter 3.1.1) we estimate shear rates in the range of $\dot{\gamma} = 10^4 - 5 \cdot 10^5$ s^{-1} by following the aforementioned iteration method (see figures 2.5 and 2.6). Shear rates for more sophisticated viscosity models can be estimated in the same way. Due to the apparent high shear rates, most viscosity models for shear-thinning liquids reach a plateau value for the high-shear viscosity (e.g. $\eta_{S,\infty}$ for Carreau-Yasuda, see Tratnig et al., 2009).

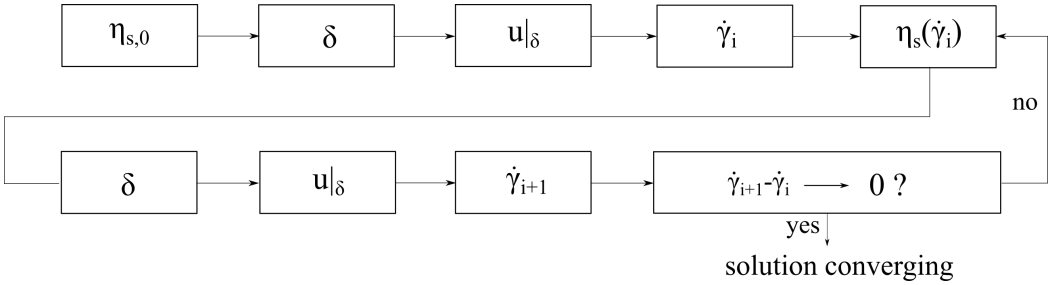

Figure 2.5: Iteration loop for the shear rate estimation. Initial shear viscosity delivers film thickness and maximum velocity in the film. Equation (2.9) is used to calculate the shear viscosity. The loop repeats until the solution converges.

2.3.2 Strain-rate estimation

During atomization, the liquids are subjected to complex flow fields, consisting of shear and elongational components (Mansour and Chigier, 1995). Since elongational flow behavior for non-Newtonian liquids depends on the strain rate $\dot{\varepsilon}$, this deformation must also be determined. The highest local strain rate is found at the critical length of a filament, where disintegration takes place. Based upon the kinematics of the emerging liquid jet (figure 2.7) a rather simple solution for the apparent strain rates can be found (see Kalmbach et al., 2016, Kuhnhenn et al., 2018, Mescher, 2012 for details).

We can calculate the strain rate at the bell edge according to equation (2.10) derived by Kuhnhenn et al. from kinetic modelling of the emerging jet from a rotating atomizer with a cylindrical bore (Kuhnhenn et al., 2018). We assume that strain rates at filament breakup are in the same order of magnitude, i.e. we obtain

$$\dot{\varepsilon} = \frac{R \cdot \omega^2}{c_{ax}}. \tag{2.10}$$

For the used atomizer and the operating parameters we expect strain rates at the bell edge in the range of $\dot{\varepsilon} = 1000 - 7000 s^{-1}$. The deformation behavior is not solely influenced by application parameters, but mainly by the elongational resistance as a material property.

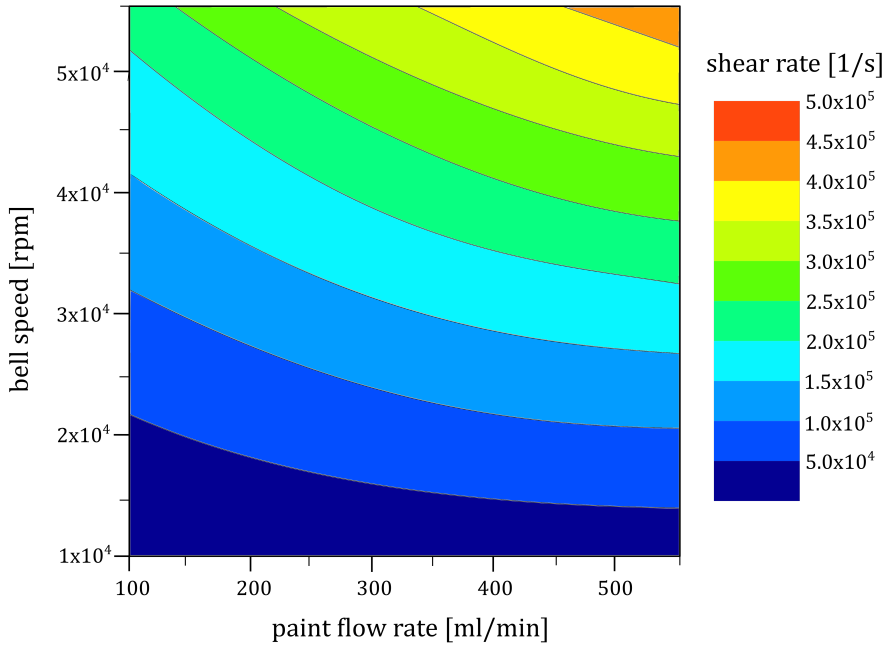

Figure 2.6: Shear rate approximation area plot as function of paint flow rate $\dot{V}_l$ and bell speed ω, viscosity model from measured data.

2.4 Dimensional analysis

Section 2.4, to a large extent, is taken from "Dimensional analysis of droplet size and ligament length during high-speed rotary bell atomization", Goedeke et al., 2021.

The dimensional analysis offers the possibility of significantly reducing the number of measurements in order to obtain desired correlations by organizing the influence parameters of a process in dimensionless groups. The correlation based on the dimensionless groups, thus, becomes generally valid, as long as the underlying physics is reflected correctly. The procedure is common for analyzing problems and can be achieved by e.g. the use of Buckingham's Π–theorem (Buckingham, 1914 and Spurk, 1992). The process and material parameters considered in the dimensional analysis are defined at the bell edge, therefore, primarily influence the length of the ligament emerging. The liga-

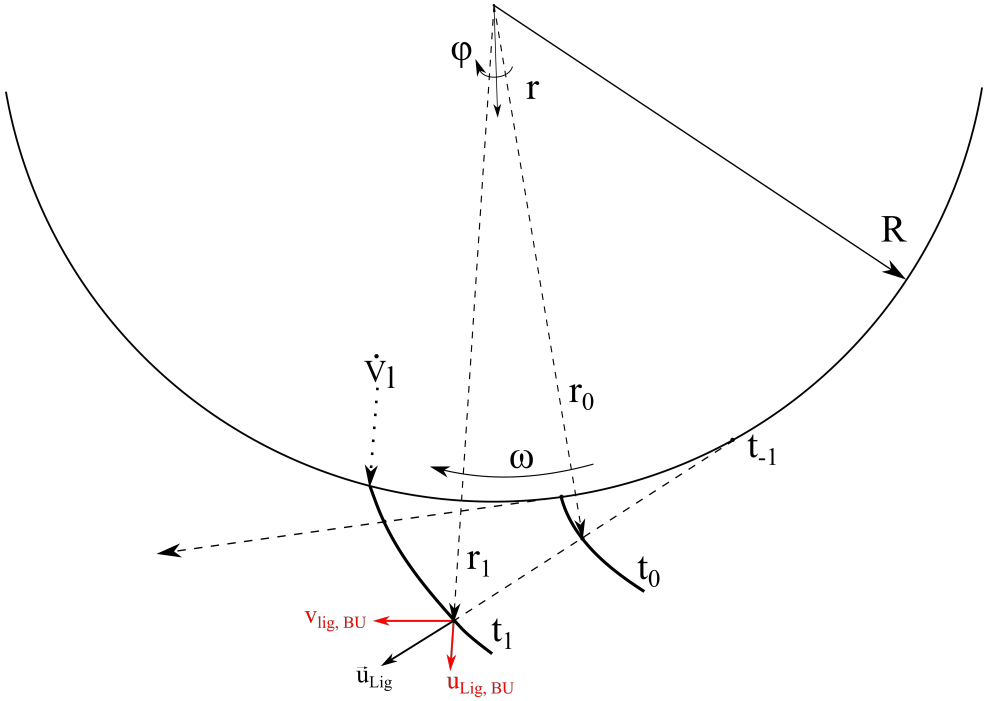

Figure 2.7: Kinematics of a emerging ligament and a fluid volume element in proximity of the break–up length.

ment length and the droplet diameter both can be used as target values for the dimensional analysis.

The dimensionless groups can be used in product of power laws to find correlations for one dimensionless group as function of the remaining groups.

$$\Pi_1 = \prod_{j=2}^{n} \Pi_i^{a_i}. \tag{2.11}$$

The axial velocity for the disturbed surface is directly proportional to c_{ax}, therefore the dependency on $\dot{V}_l$ is valid for equation 2.11.

Applying Buckingham's Π–theorem for the given system, a set of dimensionless groups can be derived, that yields the general form

$$\Pi_\Sigma = f(d_p, d_{\mathrm{Ser}}, l_{\mathrm{Lig}}, R, \omega, c_{\mathrm{ax}}, \sigma_{lg}, t_{\lambda_E}, t_{\lambda_S}, \eta_E, \eta_S, \eta_g, \rho_l, \rho_g, \rho_s, \varphi_s). \tag{2.12}$$

For the given case, we do not have a precise way of calculating the strain rate $\dot{\varepsilon}$, as the exact position of the free surface and, therefore, the exact flow field are

both unknown. Accordingly, we neglect the elongational viscosity η_E and obtain twelve dimensionless groups to characterize the general breakup process at constant ambient conditions (T = const., φ = const., p_0 = const.), i.e.

$$\Pi_{\sum} = g\left(\Pi_1, \ldots, \Pi_{12}\right), \tag{2.13}$$

$$\Pi_{\sum} = g\left(\frac{l_{\mathrm{Lig}}}{d_{\mathrm{Ser}}}, \frac{d_p}{d_{\mathrm{Ser}}}, \frac{\rho_g}{\rho_l}, \frac{\eta_g}{\eta_S}, \frac{d_{\mathrm{Ser}}}{R}, \frac{t_{\lambda_E}}{t_{\lambda_S}}, \frac{c_{\mathrm{ax}}}{\omega \cdot R}, \frac{c_{\mathrm{ax}} \cdot \rho_l \cdot d_{\mathrm{Ser}}}{\eta_S}, \frac{c_{\mathrm{ax}}^2 \cdot \rho_l \cdot d_{\mathrm{Ser}}}{\sigma}, t_{\lambda_E} \cdot \left(\frac{\sigma_{lg}}{\rho_l \cdot d_{\mathrm{Ser}}^3}\right)^{0.5}, \frac{\rho_s}{\rho_l}, \varphi_s\right). \tag{2.14}$$

Here $\Pi_1 - \Pi_6$ and Π_{11} are ratios of parameters of equal dimensions, Π_7 is the ratio of axial liquid velocity inside the ligament and tangential velocity at the bell edge and, therefore, defines the stretching characteristics of the ligament flow. Π_8 is a liquid–related Reynolds number inside the ligament at its origin ($Re_{\mathrm{ax},l}$), formed with the constant shear viscosity at the bell edge and the axial ligament flow velocity. Π_9 is a liquid–related Weber number inside the ligament ($We_{\mathrm{ax},l}$), formed with the axial ligament flow velocity and Π_{10} a Deborah number formed with a characteristic breakup time (c.f. equation 2.16). Both the Reynolds and the Weber number could also be formed as corresponding gas–related dimensionless groups. The Deborah number could also be formed with different characteristic time scales relative to a specific relaxation time. For the given case the capillary breakup time t_{cap} is chosen as the liquid–specific time scale. Hence, we obtain

$$t_{cap} = \left(\frac{\rho_l \cdot d_{\mathrm{Ser}}^3}{\sigma_{lg}}\right)^{0.5}, \tag{2.15}$$

$$\Pi_{10} = \frac{t_{\lambda,E}}{t_{\mathrm{cap}}} = De_{\mathrm{cap}}\,. \tag{2.16}$$

Dynamic and viscous time scales can be obtained through dimensional analysis by choosing the corresponding basis, e.g. the average time for a volumetric element to move through the filament or a viscous relation time. The ideal time scale for the ligament breakup is the actual breakup time $t_{\mathrm{Lig}} = l_{\mathrm{Lig}} \cdot {c_{\mathrm{ax}}}^{-1}$, which is a function of the axial velocity c_{ax} and of one of the two target modeling parameters l_{Lig} (besides d_p) and, therefore, not available as an independent

variable. For the majority of technically–used paint liquids $\Pi_6 \rightarrow 0$, as the shear relaxation time ($t_{\lambda,S} \approx 10^2 - 2 \cdot 10^4$s) is larger by several orders of magnitude compared to the elongational relaxation time ($t_{\lambda,E} \approx 10^{-2} - 5 \cdot 10^{-1}$s, as described by Oswald and Willenbacher, 2019). Additionally, for these liquids $t_{\mathrm{Lig}} \ll t_{\lambda,S}$ holds, therefore, we neglect the influence of shear relaxation on ligament breakup.

The automotive coatings investigated are shear thinning, but approach a high–shear viscosity $\eta_{S,\infty}(\dot{\gamma} = 3 \cdot 10^5\ \mathrm{s}^{-1})$ of about 15 – 30 mPas (see section 3.1.1).

2.5 Ligament breakup

Ligament break up takes place for both serrated and non-serrated bells under operating conditions. For serrated bells the liquid jet is forced into equidistant initial positions around the outer bell edge, whereas for smooth-edged bells these emerging ligaments form depending on the flow conditions and may vary in position and diameter due to flow disturbances. Ultimately, ligaments will break up and form droplets. Both ligament length l_{Lig} and droplet diameter d_p depend on the characteristics of this break-up process. This was already described in detail in 1931 by Haenlein and Weber (Haenlein, 1931; Weber, 1931).

Wallwork et al. extended their work for the application to a rotating flow field (Wallwork et al., 2002). Decent et al. propose a solution which includes viscous forces for Newtonian fluids. It turns out that the trajectory of the fluid jet and its stationary state are only slightly affected by the viscous forces (Decent et al., 2009). However, the perturbation analysis shows that the instability is dominated not only by the surface forces but also by the viscous forces, as already shown experimentally (Haenlein, 1931; Weber, 1931) for straight flux jets experimentally.

Hawkins et al. additionally considered the effect of non-Newtonian characteristics on the trajectory and the instability (Hawkins et al., 2010). A high rotational velocity is assumed so that the influence of the gravitational force can be neglected and the problem can be considered in two dimensions, assuming rotational symmetry. The non-Newtonian property is taken into account by a

general power law. From the stability analysis, it is found that the instability of a shear-thickening liquid jet occurs faster than for Newtonian liquids, causing shear-thickening liquid jets to break up at smaller critical ligament lengths. Inversely, shear-thinning liquid jets break up at larger critical ligament lengths than is the case for Newtonian liquids.

The model by Gramlich and Piesche includes a solid-laden liquid jet. The dependence of the viscosity on the shear rate is described with an empirical approach, but the influence is not considered in more detail due to the low speeds of the experiments carried out in the work (Gramlich and Piesche, 2012). Mescher pursued different approaches (mainly Wallwork et al., 2002; Gramlich and Piesche, 2012) and successfully applied them to a laminar flow rotational atomizer under influence of crosswind induced break-up mechanisms (Mescher, 2012). Kalmbach further extended the two-dimensional approach by Gramlich to a three-dimensional model by inducing crosswind influence normal to the rotating plane (Kalmbach et al., 2016). Both groups worked with model atomizers that eject a single liquid jet at moderate rotational speeds.

Bothe made an encompassing attempt to transfer the findings by the authors mentioned above to bell atomizers by regarding the rivulet flow at the bell edge and adapting the radial and axial force balances to the new given geometry (Bothe, 2018). Ultimately the solution found did not mirror the experimental findings during this research, as the influence of other emerging ligaments onto each other, as well as the highly–turbulent characteristics of the surrounding air flow and the simplifications made for the rheological characterization could not be investigated in detail. Nevertheless, the approach seems promising in regards to future modeling attempts.

Ligament lengths used in this thesis are therefore determined experimentally by high-speed imaging at the bell edge.

2.6 Fundamentals of spray characterization

2.6.1 Droplet evaporation

Depending on saturation of the ambient air, solid content and therefore evaporation rates, as well as flight times, the change of droplet diameter needs to be considered. A direct measurement of droplet sizes to track the change in diameter over time is not possible for the given process.

Ray et al. propose to track the change in area flux with increasing distance from the bell (Ray, 2015). These results have not been reproducible in the automated application facility, as the influence of the diverging spray and, therefore, the influence of diminishing spray density cannot be fully resolved. Instead of resolving the evaporation kinetics in detail, a worst–case consideration is applied to estimate the effect during the short flight time from the bell edge to the substrate.

Applying the classical d^2-law to a droplet with a constant K-value with non-volatile components of $40 - 50$ vol $-$ % in non-saturated ambient gas provides estimated droplet diameters after the given flight time from bell to substrate. Hence, we have

$$K = \frac{d}{dt} \cdot d_p^2, \tag{2.17}$$

with $K = 600\,\mu\text{m}^2/\text{s}$,

$$d_{p,1} = \sqrt{d_{p,0}^2 - 2K(t - t_0)}. \tag{2.18}$$

The lower droplet volume limit being the volumetric solid content with an added 10 vol% of solid-bound non-volatile liquid components. For droplet velocities $u_p > 10$ m/s there is no significant influence of evaporation to be expected for droplets larger than 10 μm. Droplets smaller than the threshold account for less than 10 % of the overall mass and remain with about 40 vol% of their initial volume.

2.6.2 Spatial and temporal sampling

While observing particle ensembles with optical measurement methods we need to differentiate between measuring at a defined location over a variable

amount of time (temporal sampling) and measuring for a defined time over a multitude of points, respectively over a volume (spatial sampling). A defined location is preferably a point with given coordinates in space, which in reality can only be a infinitesimally small volume. Accordingly, a defined time for an observation or measurement in reality always results in a time period $\Delta t \longrightarrow 0$. Data obtained from either of both methods need to be transformed to be comparable to the corresponding sampling method. Dodge et al. deliver a detailed description of the "convolution and deconvolution of spray data" (Dodge et al., 1987). To ensure comparability, the obtained results are evaluated based upon the method described. Most of the industrially used plug-and-play particle and droplet analyzers (e.g. Malvern® Spraytec®) are based upon laser diffraction techniques (subsection 2.9.4) that deliver volumetric size distributions obtained by spatial sampling.

2.6.3 Distribution functions and their moments

Particle and droplet ensembles can be characterized by the use of different distribution functions (e.g. normal and log–hyperbolic distributions) for their number and volume distributions, effectively reducing the entirety of individual droplet diameters to a set of parameters for the defining function of the selected distribution (Lefebvre and McDonell, 2017; Stieß, 2009). The majority of the obtained droplet distributions are unimodal and skewed right. In this work, number distributions and volume distributions are used to characterize droplet ensembles. For the number distributions, the number of particles in a particle size interval (or bin) is divided by the total amount of the particles in the collective. For volume distributions, the volume of the particles in a bin is divided by the total volume of the particle collective. All distributions can be displayed as cumulative distribution functions (*cdf*) and probability density functions (*pdf*). The probability density functions can be re–scaled to fit the experimental data sets as distribution density function (*ddf*), normalized in the sense that

$$\int_{-\infty}^{+\infty} pdf \; dx = 1. \tag{2.19}$$

The representation of a sample *pdf* and *cdf* over the particle diameter with a finite number of particle size intervals i qualitatively results in the following curves:

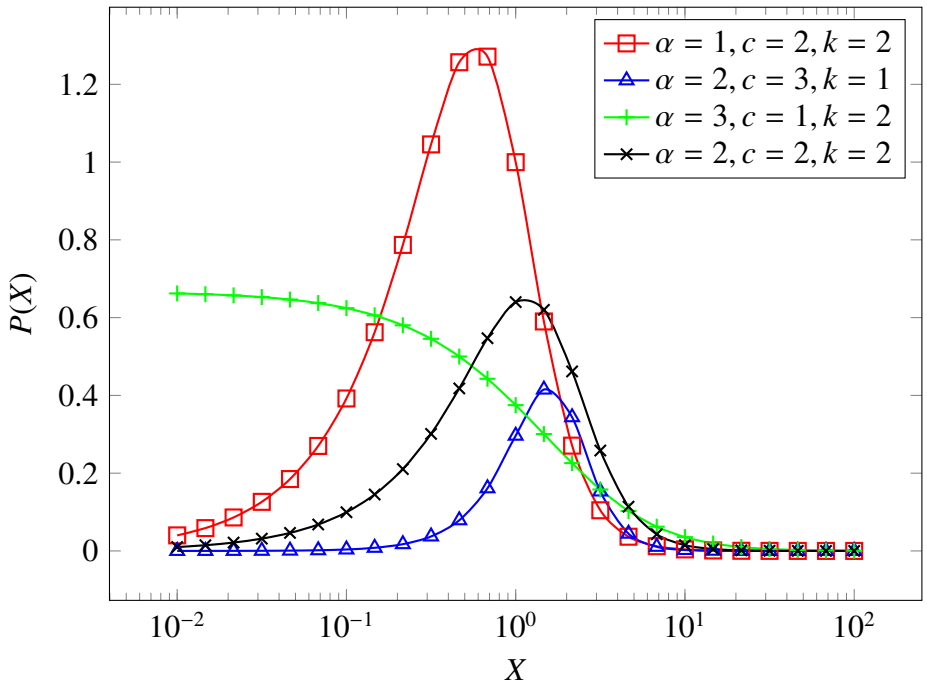

Figure 2.8: Scaled Burr Type XII probability density functions for different shape parameters α, k, c.

The Burr Type XII distribution, first introduced as a two–parameter function (Burr, 1942), then extended with an additional scaling parameter (Tadikamalla, 1980), can be adapted to almost all drop size distributions from this project without severe deviations (c.f. figure 2.8).

The *cdf* is given by

$$F(x \mid \alpha, c, k) = 1 - \left[1 + \left(\frac{x}{\alpha}\right)^{c}\right]^{-k}, \tag{2.20}$$

the *pdf* by

$$f(x \mid \alpha, c, k) = \frac{kc}{\alpha} \cdot \left(\frac{x}{\alpha}\right)^{c-1} \cdot \left[1 + \left(\frac{x}{\alpha}\right)^{c}\right]^{-k-1}, \tag{2.21}$$

with $x > 0,\ \alpha > 0,\ c > 0$ and $k > 0$. The inversion $F^{-1}(p)$ of the cdf directly delivers the $p - th$ quantile function

$$Q(p) = \left[\left(\frac{1}{1-p}\right)^{\frac{1}{k+1}} - 1\right]^{\frac{1}{c}} \cdot \alpha. \tag{2.22}$$

Here, the variable p is set to the desired values, e.g. $p = 0.25$, $p = 0.50$ and $p = 0.75$ for the first, second and third quartiles (Q_1, Q_2 and Q_3). Eventually, the ddf can be obtained by multiplying the pdf with a scaling factor ξ , corresponding to the underlying data set, i.e.

$$\widehat{f}(x \mid \alpha, c, k) = \xi \cdot f(x \mid \alpha, c, k) = \xi \cdot \frac{kc}{\alpha} \cdot \left(\frac{x}{\alpha}\right)^{c-1} \cdot \left[1 + \left(\frac{x}{\alpha}\right)^{c}\ \right]^{-k-1}. \tag{2.23}$$

The $j - th$ absolute moments $E(x^j)$ of the distributions can easily be obtained by integration, i.e. by

$$E(x^j) = \int_0^\infty x^j f(x) dx. \tag{2.24}$$

Depending on the distribution function, the analytical solution may result in sophisticated sum-functions, however, the numerical integration typically is fast and robust. Please note that the lower integral limit is set to zero, due to the fact that droplet diameters and particle sizes are always positive.

From the definition of the moments of a distribution, different mean particle sizes D_{mn}, as well as kurtosis and skewness of the distribution can be calculated. Typically, the arithmetic mean D_{10} and the so-called Sauter diameter D_{32} are used. The latter can be understood as the quotient of the total volume of the distribution and the total surface area of the distribution. In particular, the Sauter diameter emphasizes the coarse fraction of the distribution and, therefore, highlights problems with surface wetting and evaporation. The arithmetic droplet diameter is particularly suitable for comparing the main fraction of a spray under different conditions. It exhibits greater statistical insensitivity to large outliers (Stieß, 2009).

In general, the mean diameters D_{mn} are defined as the $(m-n)-th$ root of the quotient of the $m-th$ and $n-th$ moment of the distribution function, i.e.

$$D_{mn} = \left[\frac{E(x^m)}{E(x^n)}\right]^{\frac{1}{m-n}} = \left[\frac{\int_0^\infty x^m f(x)dx}{\int_0^\infty x^n f(x)dx}\right]^{\frac{1}{m-n}}. \tag{2.25}$$

The arithmetic mean value of the particle size D_{10} can be calculated as the quotient of the number-related first and zeroth moments, the Sauter diameter D_{32} accordingly is calculated as the number-related (32)-moment. The *span*-value is generally defined as

$$span = \frac{d_{90} - d_{10}}{d_{50}}. \tag{2.26}$$

These diameters can be either number ($d_{N,50}$, index N) or volume ($d_{V,50}$, index V) related and describe the width of the corresponding droplet size distribution.

2.6.4 Area-specific averaging of global mean values

According to Tratnig et al. the point-wise acquired data are to be weighted by their respective area segments and the corresponding number fluxes to define a global mean spray diameter (Tratnig et al., 2009), as

$$\bar{D}_{global,mn} = \left[\frac{\sum_{j=1}^{J}\sum_{i=1}^{I}\bar{d}_i^m(r_j)\cdot\dot{n}_i(r_j,\bar{d}_i)\cdot r_j}{\sum_{j=1}^{J}\sum_{i=1}^{I}\bar{d}_i^n(r_j)\cdot\dot{n}_i(r_j,\bar{d}_i)\cdot r_j}\right]^{\frac{1}{m-n}}. \tag{2.27}$$

Preliminary measurements have shown that the deviations for the arithmetic and median diameters are within the measurement uncertainties (max. rel. error $1,5\%$) and may be neglected, whereas the Sauter diameter D_{32} must be evaluated based on an equally area–distributed spray density due to its sensitivity for big droplets ($d_p > 100\ \mu$m, see Illner, 2017, section 3.5).

2.7 Statistical framework

2.7.1 Sample size

Panckow et al. specify the necessary number of measured droplets to calculate mean droplet diameters with sufficient statistical certainty based upon a thorough sensitivity analysis of bubble measurements. Increasing the processed quantity beyond $N_{\text{count}} = 10^4$ detections does not significantly increase the accuracy for measured and calculated mean diameters (Panckow et al., 2013). Adams et al. confirm this result for the statistics of obtained droplet size distributions measured with a PDA system (Adams et al., 1990). The arithmetically averaged droplet diameter D_{10} often stays practically unchanged after reaching a sample size of $N_{\text{count}} > 5000$. Depending on the spread of the distribution and the tendency for large droplet formation, the D_{32} is slightly more sensitive to the number of validated detections and can change for an increase beyond 10.000 counts, mostly within the limits of the measurement uncertainty of the used device. As a result, a count number of $N_{count,min} = 10.000$ is defined as target for the experimental measurements. For cases, where $N_{count,min}$ cannot be reached, consequences have to be discussed.

2.7.2 Histogram properties

Typically, a histogram is derived from the raw or refined data of a measurement, following specific rules for the number of bins and their widths (e.g. square root–choice or Sturge's formula). The general conditions for the design of histograms describing the experimental data sets and serving as a basis for the analytical distribution functions must be clearly defined, as the histogram properties influence the parameter fitting for the distribution functions for cases where the fit is applied after assigning individual droplets to their respective bin. The number of bins N_{bin} and the bin width h are connected by the formula

$$N_{\text{bin}} = \left\lceil \frac{x_{\text{max}} - x_{\text{min}}}{h} \right\rceil, \tag{2.28}$$

with $x_{\text{max}} - x_{\text{min}}$ defining the particle size interval, typically with $x_{\text{min}} = 0$ as a lower limit. The braces indicate the ceiling function, delivering the next integer

greater than the inserted real number within the brackets, effectively rounding up.

The bin width can be obtained from equation (2.28) for the bin number calculated with the Rice rule for example (2.29) as

$$N_{\text{bin}} = \left\lceil 2 \cdot \sqrt[3]{N_{\text{count}}} \right\rceil. \tag{2.29}$$

Due to the frequent occurrence of outliers in the measured diameters, it is recommended to calculate the bin width with the Freedman-Diaconis rule (Freedman and Diaconis, 1981), i.e.

$$h_{\text{FDR}} = 2 \cdot \frac{IQR(x)}{\sqrt[3]{N_{\text{count}}}}. \tag{2.30}$$

The obtainable histogram data is coherent with the parameter fit (α, c, k) of the scaled Burr Type XII function (2.23), which is used to calculate the interquartile range

$$IQR(x) = Q_3 - Q_1 \tag{2.31}$$

of the distribution, defining the bin width h_{FDR}. The calculated class width h_{FDR} is dependent on the maximum particle diameter x_{max}, as the interquartile range $IQR(x)$ is defined by parameters of the ddf (equation 2.22) or the numerical interpolation $IQR(x)$ from the distribution data (Dunning and Ertl, 2019; Langford, 2006). Conventionally used tools for particle and droplet analysis usually incorporate the different estimation methods for the number of classes and the resulting bin widths (see chapter 4.4).

2.8 Droplet impact and air entrapment

Bubble entrapment plays an important role during painting processes in the automotive industry. During droplet impact on solid substrate, bubble entrapment can occur in the liquid film under certain conditions. The resulting bubbles are substrate-bound and not mobile. During subsequent drying, these bubbles cannot escape through the surface and lead to the formation of pinholes in the paint film (section 1.2). The tendency for bubble formation and the characterization of the dynamic process of air entrapment can be characterized by dimensionless groups (Re, We, $Oh = We^{0.5} \cdot Re^{-1}$) and wetting dynamics.

For a detailed description of the underlying mechanism see Thoroddsen et al., 2005.

Burzinski (Burzinski, 2018) and Grünendahl (Grünendahl, 2017) both show that it is possible to provoke bubble formation and entrapment for different Newtonian fluids under scaled–up laboratory conditions and capture the formation by high-speed imaging. Though occasional bubble formation can be observed during automotive painting, the mechanism is not fully understood. A transfer of the experimental results from their findings to the smaller–scale droplets is not yet realized. The characterization for non-Newtonian fluids based on the underlying shear and strain relaxation times is possible in principle via the Deborah number (De) but is not within scope of the present project.

2.9 Measurement of opaque paint fluids

The fundamental principles of light scattering, phase Doppler anemometry, as well as time–shift measurement techniques are more than adequately described in *Laser Doppler and Phase Doppler Measurement Techniques* by Albrecht, Borys, Damaschke and Tropea (Albrecht et al., 2014). The information contained in **the** reference work embraces all relevant aspects of the applied laser measurement techniques, which is why only the particular features for the investigation of paint droplets will be highlighted and explained here.

The majority of industrially used paints are neither homogeneous, nor transparent, which poses additional difficulties for the applicability of optical measurement systems. The following section discusses these problems regarding the spray-painting process with opaque and particle–laden fluids. It is of note that for both, PDA and TS the minimum reliably detectable droplet diameter d_p has to be larger than the wavelength λ of the used laser. For the given setups the cut-off is made for droplets smaller than 1 μm.

2.9.1 Principles of light–scattering for opaque liquids

Electromagnetic waves passing through a not fully-transparent medium will be attenuated and are subject to an exponential decay in intensity, according to

Beer-Lambert law. This is the case for the majority of industrially used fluids, usually described by a complex refractive index $\underline{n}$ (Hecht, 2003), i.e.

$$\underline{n} = \mathfrak{n} + i\kappa. \tag{2.32}$$

Here $\Re\{\underline{n}\}$ describes the real part of $\underline{n}$, the phase velocity related refractive index n and $\Im\{\underline{n}\}$ describes imaginary part, the extinction coefficient for exponential intesity decay κ. It is of note, that n and κ are both dependant on λ, hence $\underline{n}(\lambda)$.

Furthermore, the presence of solid particles inside a droplet, like pigments or droplets of another, immiscible fluid of different refractive index, lead to the addition of scattering centres.

This further decreases intensity and unambiguity of the scattered light distribution compared to the ideal homogeneous droplet for higher scattering orders ($1st, ..., n-th$). However, reflected light ($0th$-order) mostly remains unaffected by effects inside the droplet, except for high surface absorption, e.g. due to large amounts of soot particles at the droplet surface.

With different methods, a determination of the refractive index $\underline{n}$ or the concentration of solid particles and emulsion droplets from measured scattering light signals is possible (see Albrecht et al., 2014 section 5.4, and Schäfer et al., 2015).

2.9.2 Phase Doppler anemometry

Phase Doppler anemometry (PDA) is based on laser Doppler anemometry (LDA), a standardized optical technique to obtain multi–directional velocity components with a high spatial and temporal resolution. The use of three receiving units (detectors, index $r = 1, 2, 3$) for two laser beams ($b = 1, 2$) delivers information about the phase shift $\Delta\Phi_{b,r}$ of the detected light signals (see Albrecht et al., 2014, sections 2.2 and 5.3): Intersecting laser beams define a measurement volume in the coordinate origin. Droplets enter the volume and the light signal is captured by the three detectors. The phase shift in the detected light signals is used to calculate the curvature of the spherical droplets. For the phase shift

$$\Delta\Phi_{1,2} = -\Delta\Phi_{2,1} = \Phi_1 - \Phi_2, \tag{2.33}$$

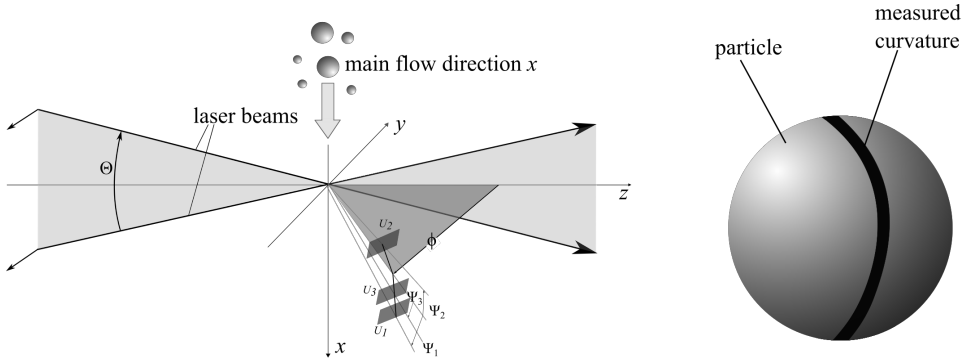

Figure 2.9: Schematic representation of the PDA principle (Albrecht et al., 2014).

$$\Delta\Phi_{1,2} = (\phi_{1,2} - \phi_{1,1} + \phi_{2,1} - \phi_{2,2}) + (\Psi_{1,2} - \Psi_{1,1} + \Psi_{2,1} - \Psi_{2,2}), \tag{2.34}$$

hold while analogue equations can be obtained for (1,3) and (2,3). Here $\phi_{b,r}$ is the detector off-axis angle, $\pm\Psi_{b,r}$ the detector elevation angle and Θ the beam intersection angle. The first detector pair (1,2) is sufficient to determine the particle or droplet diameters (${d_p}^{(0)}$ for reflection and ${d_p}^{(1)}$ for 1*st*-order refraction), i.e.

$${d_p}^{(0)} = \frac{\Delta\Phi \cdot \lambda}{2\pi} \cdot \frac{\sqrt{2 \cdot (1 - \cos\Theta/2 \cdot \cos\Psi \cdot \cos\phi)}}{\sin\Theta/2 \cdot \sin\Psi}, \tag{2.35}$$

$${d_p}^{(1)} = -\frac{\Delta\Phi\cdot\lambda}{2\pi} \cdot \frac{\sqrt{2\cdot(1+\cos\Theta/2\cdot\cos\Psi\cdot\cos\phi)(1+n_{\mathrm{rel}}^2-n_{\mathrm{rel}}\cdot\sqrt{2\cdot(1+\cos\Theta/2\cdot\cos\Psi\cdot\cos\phi)}}}{n_{\mathrm{rel}}\cdot\sin\Theta/2\cdot\sin\Psi}, \tag{2.36}$$

with

$$n_{\mathrm{rel}} = \frac{n_{\mathrm{disperse}}}{n_{\mathrm{continuous}}} = \frac{n_d}{n_{\mathrm{air}}}. \tag{2.37}$$

The second pair (1,3 or 2,3) is used to validate the results obtained by the first detector pair, i.e.

$$\Delta\Phi_{1,2} = \Delta\Phi_{1,3} - \Delta\Phi_{2,3}. \tag{2.38}$$

The phase shift delivers the diameter of spherical droplets or an estimate of the deformation of droplets by regarding the phase differences from each pair for a known diameter. Therefore, the deviation from the ideal spherical shape can be determined. The used device is flexible for focal lengths of different lenses, scattering angles and detector offset angles by use of different aperture masks (see subsection 4.4.2). The exact alignment of the components is critical. Again, transparent and opaque droplets can be detected and processed selectively, based upon the order of refraction.

2.9.3 Time–shift technique

The time-shift (TS) method analyzes the backward reflected or refracted light of droplets passing a laser beam. For the SpraySpy® device, the measurement volume corresponds to the overlap cross–sectional area of two skewed laser beams of different wave length. The resulting light signal is recorded by photo multipliers and analyzed in its frequency. For each droplet passing a single beam, a unique burst signal can be obtained and evaluated regarding droplet size, velocity and, in case of refraction, regarding the refractive index of the fluid. A detailed description of the signal processing, as well as diameter and velocity calculation can be found in Schaefer et al., 2021. The dual-beam mode is a SpraySpy® specific setup to improve the validation for both velocity and diameter measurement. The detector head contains transmitter and receiver

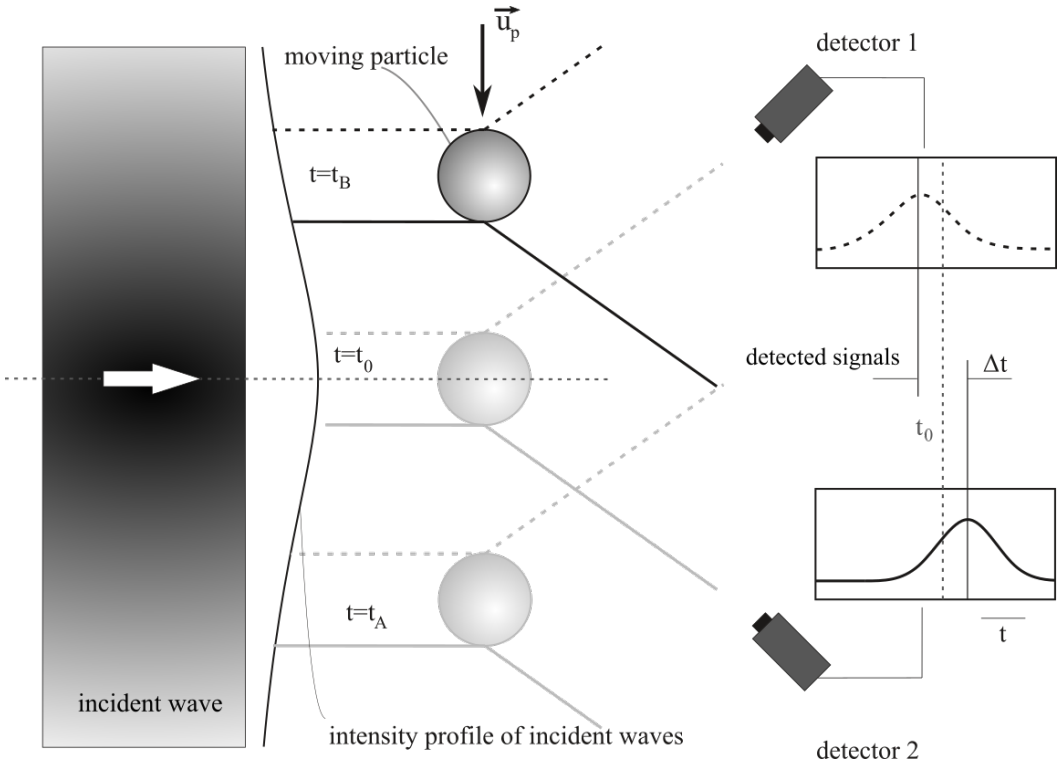

Figure 2.10: Time-shift measurement principle. Left: moving particle interacting with the incident beam. Right: signals recorded by both detectors for a particle of velocity $\vec{u}_p$ and diameter d_p. Δt is the time shift between the detectors. It holds that $\Delta t \propto d_p$ and $\Delta t^{-1} \propto \left|\vec{u}_p\right|$, (Albrecht et al., 2014).

simultaneously, which makes the experimental setup simple. No alignment of corresponding units is needed (c.f. figure 2.11). According to Schäfer and Rosenkranz transparent, partially– and fully–opaque droplets can be detected (Schäfer et al., 2015). However, due to its plug–and–play characteristics with

Figure 2.11: Commercial time shift device SpraySpy® by AOM Systems, Rosenheim, Germany.

the compact detector head there are limitations with regard to lens positioning by variation of the off-axis and the elevation angles. The low laser power is a payoff towards the explosive atmosphere applicability, leading to a very short focus length ($f < 125$ mm) as a major drawback of the system for applications in larger scale spray environments. The SpraySpy® system is delivered with a developed software package for measurement settings as well as post processing. During the time of the experiments there was no way to export raw (valid and invalid) measurement data due to computational and data transfer limitations.

2.9.4 Laser diffractometry in sprays

Laser diffractometry (LD) is based upon both Fraunhofer and Mie diffraction, depending on the size and the composition of the analyzed droplets. Because the underlying Lorenz-Mie theory relies on homogeneous isotropic spheres with a constant complex refractive index $\underline{n}$ (see equation 2.32), which typically is unknown with regards to its imaginary part, it is impossible to evaluate the signals correctly. Fraunhofer diffraction on the other hand does not require knowledge of optical constants. It is applicable for mixtures of different materials and deviations from the spherical shape. The determined

droplet diameters correspond to the equivalent diameters of the diffraction-equivalent spheres. Simultaneous diffraction of more than one droplet results in superposition of diffraction patterns. Analogue to the limitations for the minimal droplet size for PDA and TS, the Fraunhofer diffraction only is reliable for opaque droplets that are large in relation to the wavelength of the laser ($d_p > 10\ \mu$m). Commercially available devices (e.g. Sympatec Helos® or Malvern SprayTec®) use designated algorithms to fit volumetric droplet size distributions to the diffraction patterns. Comparing results from LD to PDA and TS demands convolution and deconvolution of data (Dodge et al., 1987).

3

Experimental setup

3.1 Experimental setup

The particle size measurements are performed by using a Dantec FiberFlow phase Doppler anemometer (PDA) powered with a Lexel 95 Ar-ion laser (λ = 488/514.5 nm, parallel polarization, output laser power 150 mW) and the AOM Systems SpraySpy time shift device (TS). Both optical devices are non–invasive and capable of simultaneously acquiring droplet size and one component of the velocity vector without distorting the spray geometry. The experimental setup is placed inside a conventional, fully automatic and climated spray booth (RaCE/BASF Coatings GmbH in Münster, Germany, T = 25°C, φ_{air} = 65%). The positioning accuracy of the application unit (ABB IRB 5500) is within ±0.5 mm, with a minimum absolute movement velocity of $\vec{v}_{rob}$ = 0.5 mm/s. The spray booth is free of dust with constant ambient conditions. A constant stream of filtered air passes the room vertically from top to bottom with a mean velocity of 0.3 m/s.

The atomizer is an EcoBell2 (Dürr AG, Stuttgart, Germany) with both, serrated and non-serrated bells (R = 32.5 mm, d_{Ser} = 0.12 mm, $\mathrm{N_{Ser}}$ = 480). Liquid volume flow rates and bell speeds are varied in the ranges $\dot{V}_l$ = 200 − 550 mL/min and $\omega = 10 - 65 \cdot 10^3$ rpm. The shaping gas flow rate is held constant at 0.34 scm/min (scm = standard cubic meter). Previous work has shown no significant influence of the shaping gas flow rate on droplet size at the bell edge.

A mounting socket is centered inside the spray booth, with known location and dimensions in regards to the automated robotic painting system. Both, the PDA and the TS setups were mounted on the socket to provide equal airflow conditions by maintaining identical measurement locations.

3.1.1 Properties of atomized liquids

All initial measurements at the BASF Coatings RACE facility are performed by atomization of cleaning solution (water + organic solvent), commercial waterborne base coat (M_0, dark grey metallic), custom–formulated waterborne coatings M_1, M_2 and M_3, containing different pigmentations and/or binders, as well as Sterocoll mixtures without solids S_{1-5} and Sterocoll S_2 with different glass flake solid content S_2G_{1-2}. The relevant Sterocoll liquid properties are displayed in table 3.3. These properties are considered for the formation of the dimensionless groups (see section 2.4). Due to a non-disclosure agreement the exact liquid properties of the coatings $M_0 - M_3$ are not publicly available. During further data evaluation the corresponding dimensionless groups will be used to represent the different influences. The approximate values for these liquids are in the ranges as listed in table 3.1.

Table 3.1: Fluid property ranges of the used automotive coatings $M_0 - M_3$

property	value range	unit
ρ_l	$1000 - 1050$	kg/m^3
φ_s	$0.03 - 0.08$	m^3/m^3
σ_{lg}	$25 \cdot 10^{-3} - 35 \cdot 10^{-3}$	N/m
$\eta_{S,\infty}$	$1.5 \cdot 10^{-2} - 2.7 \cdot 10^{-2}$	$Pa \cdot s$

Accordingly, Re, We, De number and $\Pi_7 = c_{ax}/(\omega \cdot R)$ are in the ranges as listed in table 3.2.

It is of note that the Reynolds number is formed with the radial discharge velocity at the bell edge. Division of Re by Π_7 delivers a bell tangential velocity Reynolds number, which is more accurate to characterize the surrounding flow conditions. Combination of the different dimensionless groups (see section 2.4) enables variable definition of the common groups for the different phases.

Table 3.2: Value ranges of the resulting dimensionless groups for $M_0 - M_3$

dimensionless group	value range
Re	$4 \cdot 10^3 - 4 \cdot 10^4$
We	$3 - 40$
De	$1.1 \cdot 10^3 - 7.2 \cdot 10^4$
Π_7	$4.5 \cdot 10^{-3} - 8 \cdot 10^{-2}$

Table 3.3: Liquid properties for the different mixtures $S_1 - S_5$ of Sterocoll® SHT and SXT used in the experimental setup. Shear viscosities $\eta_{S,\infty}(\dot{\gamma} = 3 \cdot 10^5\ \mathrm{s}^{-1})$ are measured by use of a piston driven capillary rheometer at $T = 25°C$ (Oswald et al., 2020).

Liquid	SHT [vol. – %]	SXT [vol. – %]	φ_s [m³/m³]	ρ_l [kg/m³]	σ_{lg} [mN/m]	η_S [Pa · s]	t_λ [s]
S_1	2.3	0	0	1025.7 ± 4.8	33.4 ± 0.3	$2.65 \cdot 10^{-2} \pm 5 \cdot 10^{-4}$	0.013 ± 0.001
S_2	1.8	0.22	0	1013.7 ± 6.5	32.2 ± 0.3	$2.57 \cdot 10^{-2} \pm 5 \cdot 10^{-4}$	0.038 ± 0.002
S_3	1.6	0.40	0	1016.3 ± 5.3	33.0 ± 0.4	$2.61 \cdot 10^{-2} \pm 1 \cdot 10^{-4}$	0.420 ± 0.071
S_4	1.0	0.23	0	1013.7 ± 5.4	34.6 ± 0.4	$2.01 \cdot 10^{-2} \pm 9 \cdot 10^{-4}$	0.044 ± 0.003
S_5	0.2	0.51	0	1010.5 ± 6.7	35.2 ± 0.2	$1.57 \cdot 10^{-2} \pm 2 \cdot 10^{-4}$	0.034 ± 0.002
S_2G_1	1.8	0.22	0.013	1030.7 ± 6.5	32.7 ± 0.3	$2.65 \cdot 10^{-2} \pm 5 \cdot 10^{-4}$	0.052 ± 0.005
S_2G_2	1.8	0.22	0.035	1065.7 ± 6.5	32.2 ± 0.3	$2.65 \cdot 10^{-2} \pm 5 \cdot 10^{-4}$	0.136 ± 0.012

3.2 PDA setup

The experimental setup is flexible for both focal lengths and scattering angles. Exact alignment of all components is crucial. The basic setup for the PDA is defined by its operating geometry. Both, the transmitter (Dantec FiberPDA, $f = 400$ mm) and the receiver (Dantec FiberFlow, $f = 500$ mm) units have to be in plane, non–tilted along to their lengthwise rotational axis and setup in regards to the desirable measurement angle. The specific focal length of both units is defined by their front lenses, however, both units have to be focused onto the same point inside the spray booth, the measurement volume.

Transmitter and receiver are mounted to an L-shaped metal rack which is set up on the central socket in the booth. Both units can be rotated in plane to

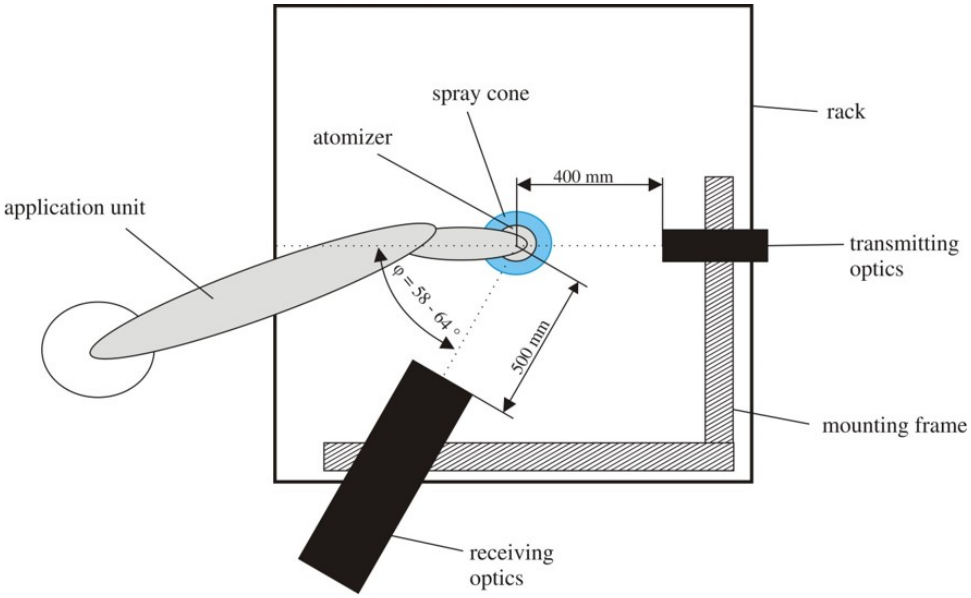

Figure 3.1: Schematic measurement setup for the PDA. L-shaped mounting rack with both units inside their protection housings.

enable a wide variety of different measurement angles (10-170°). Early measurements with base coat paint spray establish the optimal scattering angle at 58° – 64°, hence, operation under forward scattering conditions (see figures 3.1 and 3.2, cf. Illner, 2017 and Witt, 2017).

To shield both units against paint spray deposition and the resulting clogging of the front lenses, they are placed inside a PVC casing with a 2 mm thick quartz–glass front window, aligned under a zero degree angle to the front lenses. The casing is closed after alignment of receiver and transmitter and sealed with duct tape. Preemptive measurements have shown that the influence of the quartz–glass front window is negligible. In case of misalignment, the Dantec BSA Flow Software can correct the influence of the front window, given the deviation angle. The laser is captured at the left side behind the transmitter optic casing. The mounting rack is also shielded against paint. Both optical cables are inside a protection tubing, the laser pathway is visible in the spray cone of the base coat paint (figure 3.2).

The laser beam is captured behind the measurement volume by means of a simple laser trap, consisting of two bend pipes, painted with black matte paint,

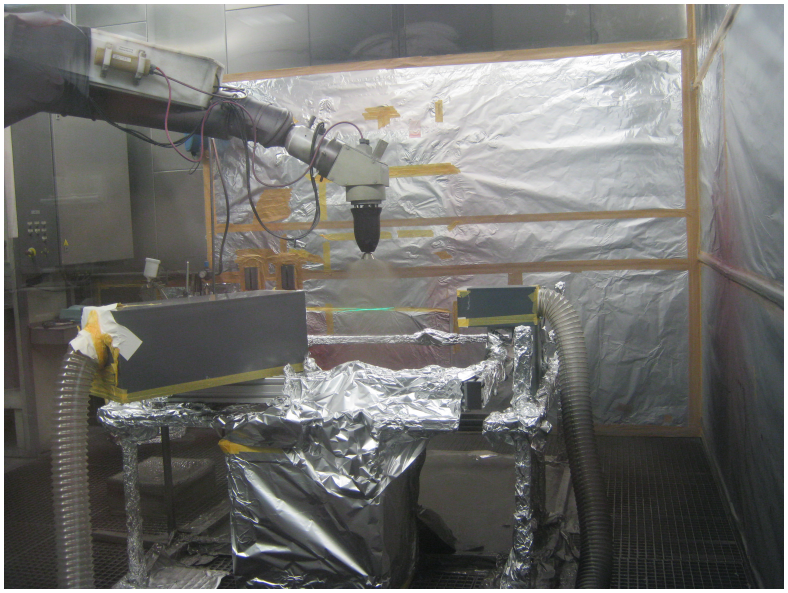

Figure 3.2: PDA setup during a measurement inside the spray booth.

thus absorbing the laser light scattered inside the pipe back wall. The robotic painting unit moves in a way, so that the laser path can not be intersected by any part of the robotic arm. This ensures that no uncontrolled laser light reflection can take place.

Conventional PDA systems measure phase shifts in received light signals by use of different receiving apertures (masks, figure 3.3), based upon the desired target particle size ranges (see section 3.5.1). To refine the measuring process, we investigate the influence of the possible particle size ranges (subsection 4.4.2). Due to a change in received light intensity, mask A will prioritize smaller particles, whereas mask C is able to measure particles with a diameter up to 1.2 mm by reducing overall light intensity (table 3.4). This results in a drastic change of data rates and obtained particle size distributions.

The receiving unit is connected to the burst spectrum analyzer (Dantec BSA P60) by optical fibres. The power unit, the laser and the BSA unit are placed outside the spray booth to ensure explosion protection and connected to the dual channel interlock system, which is connected to the door locking system of the booth.

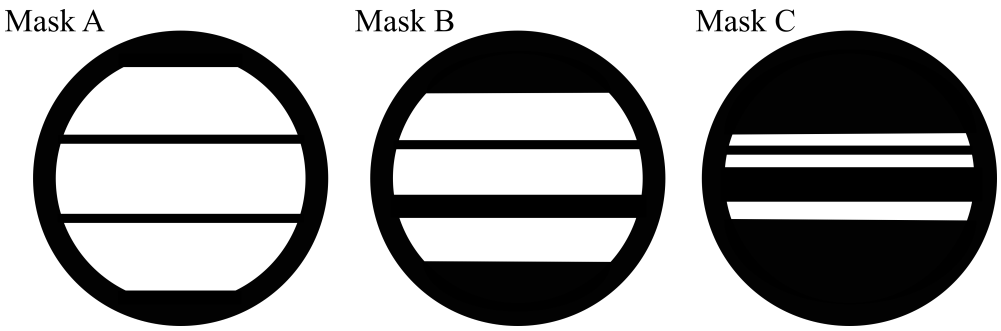

Figure 3.3: Different receiver aperture masks for the Dantec PDA. Intensity of received light decreases from A over B to C. Maximum detectable particle diameter: mask A d_p = 320.2 μm, mask B d_p = 518.8 μm, mask C d_p = 1243.7 μm (*BSA Flow Software users Guide v6.12* 2014).

Table 3.4: Maximum detectable particle/droplet sizes for the Dantec PDA measurement apertures.

aperture	max. diameter [μm]
mask A	320.2
mask B	518.8
mask C	1243.7

Due to the wire casing of the glass fibre cables from both the receiver and transmitter and resulting safety concerns, measurements under high–voltage electric fields were not performed.

3.2.1 LDA setup

The used emitter also functions as a receiver for a LDA setup. The blue laser light that is emitted from the Lexel 95 Ar-ion laser (λ = 488/514.5 nm) is used to define a secondary measurement volume rotated 90 degree in plane relative to the PDA (and primary LDA) measurement volume. Preemptive LDA measurements have shown difficulties in sufficient data rates for the used liquids and the 488 nm laser light. As the PDA measurements capture the vertical droplet velocity, a single measurement with the LDA was performed to obtain qualitative information on the radial and tangential velocity in the spray cone. The radial velocity inside the spray is captured by moving the measurement

volume through the cone in radial direction orthogonal to the main laser light propagation direction. Accordingly, moving the measurement volume along a radial axis in line with the laser light propagation, the tangential velocity component is measured (see figure 3.4). A detailed description of the measurement principle is found in *Laser Doppler and Phase Doppler Measurement Techniques* (Albrecht et al., 2014), software settings and Dantec LDA specific explanations are found in the BSA Flow Software Guide (*BSA Flow Software users Guide v6.12* 2014).

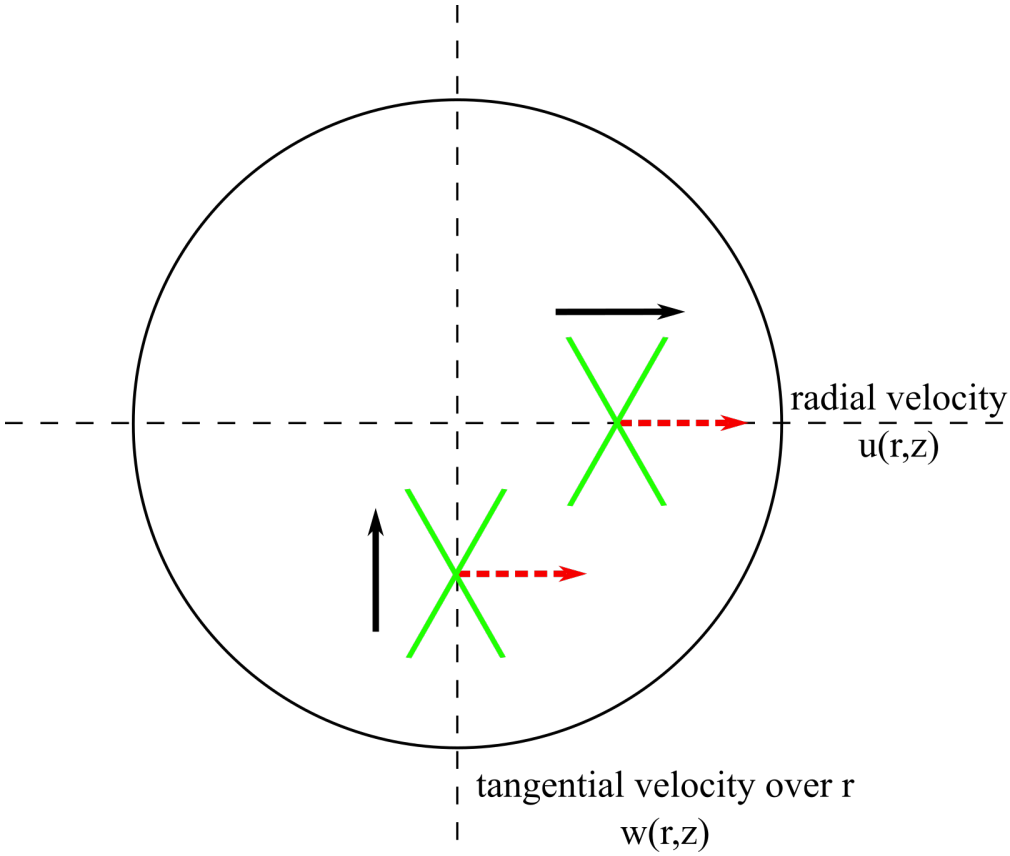

Figure 3.4: LDA measurement volume traversing directions for radial and tangential velocity component measurements. The black arrow denotes the movement direction of the measurement volume, the red dashed one the corresponding velocity component. Measured velocity component is always orthogonal to laser propagation direction in plane of both beams.

3.2.2 BSA software configuration

The Dantec BSA P60 processes the raw data and communicates with a Lenovo P50 Thinkpad (i7-6700HQ, 8GB DDR4) running Dantec BSA Flow Software v6.12.

The software settings for the optics are chosen according to the used lenses, masks and geometrical setup. Maximum acquisition time is set to a sufficiently large value, so that the traversed distance is covered, depending on the movement velocity of the atomizer head. Maximum number of samples is set to 10^6. The center velocity and velocity span are set according to the expected spray velocity, depending on the measurement position in the spray cone (cf. Utan, 2019 and Witt, 2017, as well as *BSA Flow Software users Guide v6.12* 2014, see chap. 13 and 14).

Contrary to the usual approach, the sphericity tolerance $\mathbb{S}_{\text{tol}}$ is set to 75% to enable the full capturing of the raw data while excluding the influence of the Gaussian beam and slit effects (Albrecht et al., 2014, see section 8.3) , which subsequently is further evaluated (see section 4.4). Typically $\mathbb{S}_{\text{tol}}$ is kept around $10 - 20\%$. To measure opaque droplets under reflection, the refractive index is set to $n = 2$, the software specific setting.

3.3 TS setup

The used time-shift device (AOM Systems SpraySpy®) combines emitter and receiver within a measurement unit. The two skewed laser beams (Nd:YAG, 380/488 nm, $2x10$ mW) are emitted by use of two lenses in the centre of the unit. For each laser two detectors are used, therefore, another four lenses are integrated in the head above and below the emitter lenses, slightly tilted to focus on the measurement volume.

As no changes can be made to the geometric constellation of the lenses by the user, the device has plug–and–play characteristics and is quick to setup (see figure 3.5).

The focal length is fixed, as the lenses are not easily interchangeable. For the given version, the focal length is set to 125 mm. This enables the use of low

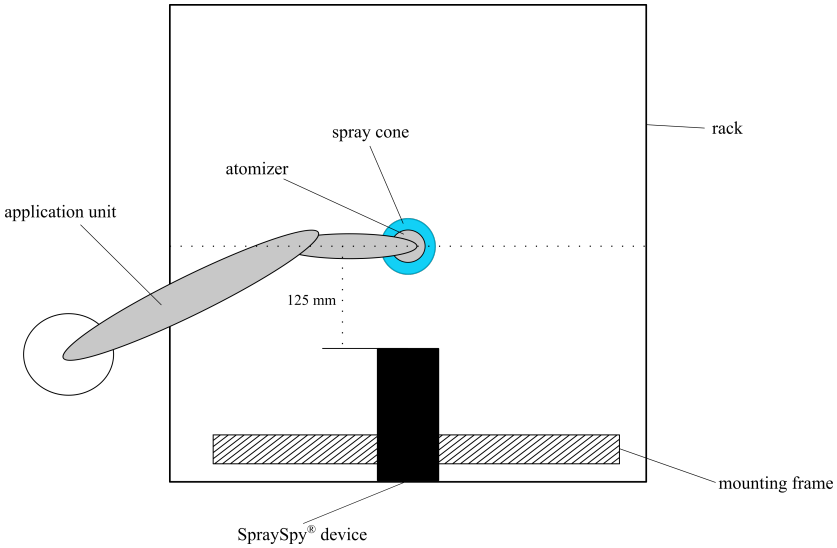

Figure 3.5: Schematic measurement setup for the TS. The measurement head is mounted directly to the socket inside the cabin.

powered lasers, with the payoff being a loss of focal length flexibility and a short distance between measurement unit and application device. Due to proximity and the resulting danger of electric discharge, measurements under influence of high–voltage electric fields are not possible during the experiments, even though the device is ex-certified (see figure 3.6).

To further minimize painting of the lenses and the distortion of air flow, the atomizer head is tilted away from the measurement head at a defined inclination angle. The distance from the bell edge to the laser is chosen large enough to ensure full disintegration of ligaments in proximity, while being close enough to the edge of the bell to keep the spray dense. The measurement axis, which is dependant on material and process properties, starts outside the emerging spray cone and ends vertically underneath the center of the tilted bell (see section 3.5.2).

Particle size range is set to $d_p = 1 - 500\ \mu$m inside the software with a valid velocity range from $\vec{v}_p = 6 - 45$m/s. Upper and lower limit change simultaneously depending on the value set for the upper limit.

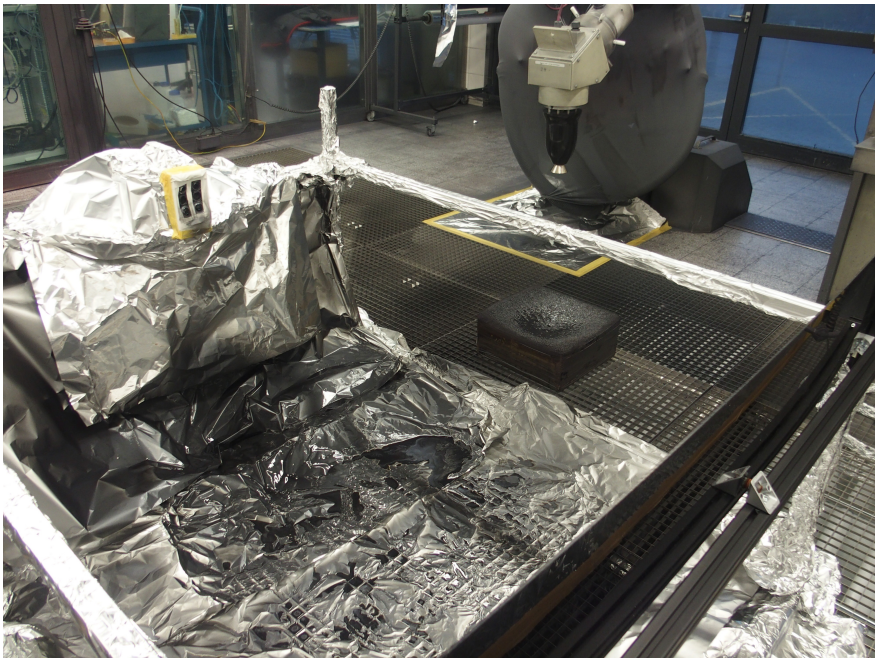

Figure 3.6: TS setup during measurement. Due to proximity between spray cone and the device the air flow is distorted. After a few runs the lenses need to be cleaned with solvent.

3.4 High–speed imaging setup

High–speed capturing of ligament breakup and droplet impact is performed with a Fastcam SA-Z (Photron Tokyo, Japan) combined with a telecentric objective (Sill S5LPJ1007/216, magnification: 1.0, operating distance: 91 mm) achieving a resolution of 19.8 μm/pixel. For images with a resolution of 512 x 256 pixels, frame rates of 10^5 fps can be recorded. Choosing 768 x 1024 pixels as resolution and decreasing the frame rate to 25.000 fps enables the capturing of longer ligaments. Illumination is performed with a pulsed green laser LED (LED-P40 SMETEC, Erkelenz, Germany) in back-lighting. The atomizer bell is tilted away from the camera slightly to avoid painting of the front lens (see figure 3.7).

Focusing of the optics is realized with the help of fine fibers of masking tape which are attached to the edge of the bell. These fibres are in a comparable

Figure 3.7: High-speed imaging with back-light laser illumination during atomization of clear coat - copyright by D. Briesenick, BASF Coatings GmbH.

size range of the ligaments, but can be held static to avoid motion blur while focusing.

3.5 Measurement method development

3.5.1 Traversing measurements

PDA and TS measurements are typically performed on a fine grid to ensure an overall sufficient spatial resolution. For traversing measurement systems this has always been the ”go-to” way to observe a complete spray cone. Conventional software packages typically support the definition of different three-dimensional coordinates within a measurement campaign, that are consecu-

tively measured for a given predefined setting, position after position until the number of counts or the maximum measurement time is achieved, either by use of a traverse system or moving the atomizer head by means of software interface communication.

For this application, however, a new way of measuring has been developed to increase time efficiency and, therefore, material efficiency by a factor of about ten, without losing desired information of the spray. Instead of measuring point-specific along a defined grid ($[0,0]$ to $[n,n]$), the measurement volume moves through the spray relatively, by continuously moving the atomizer head during the application (figures 3.8, 3.9). It is of note, that the movement slightly disturbs the spray flow pattern due to the relative movement in regards to the surrounding atmosphere. Whenever possible the spray is to be held at a steady location and the PDA/TS setup is moved along the measurement axis. For the application booth this is not easily achievable and we rely of the first variant.

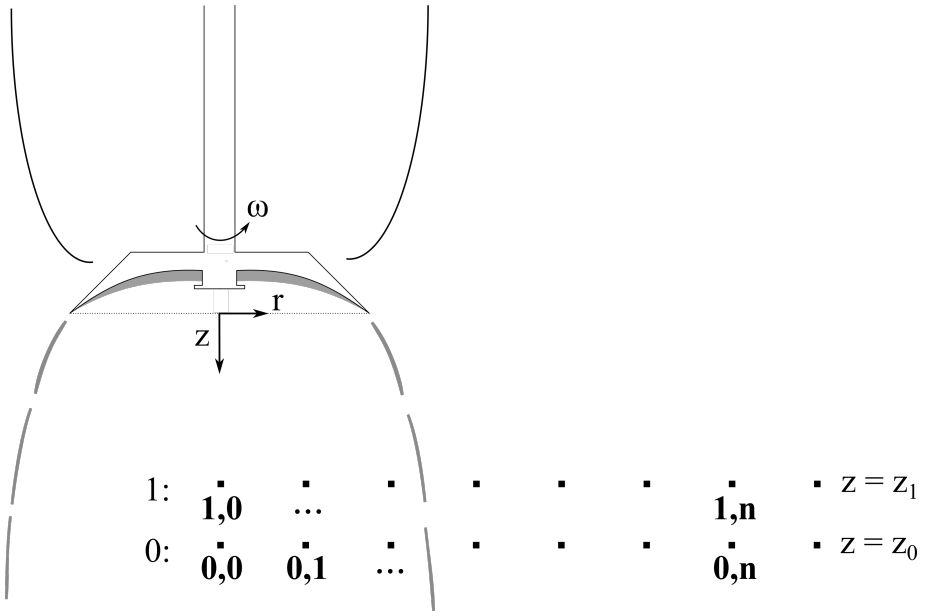

Figure 3.8: Standard grid measuring procedure. Individual point measurement (r,z - coordinates) until $N_{count,min}$ or t_{meas} is reached.

For both methods, each validated detection delivers droplet diameter, axial velocity and a unique time stamp. The corresponding radial positions in the supposedly symmetric spray cone for the droplets can be calculated as a func-

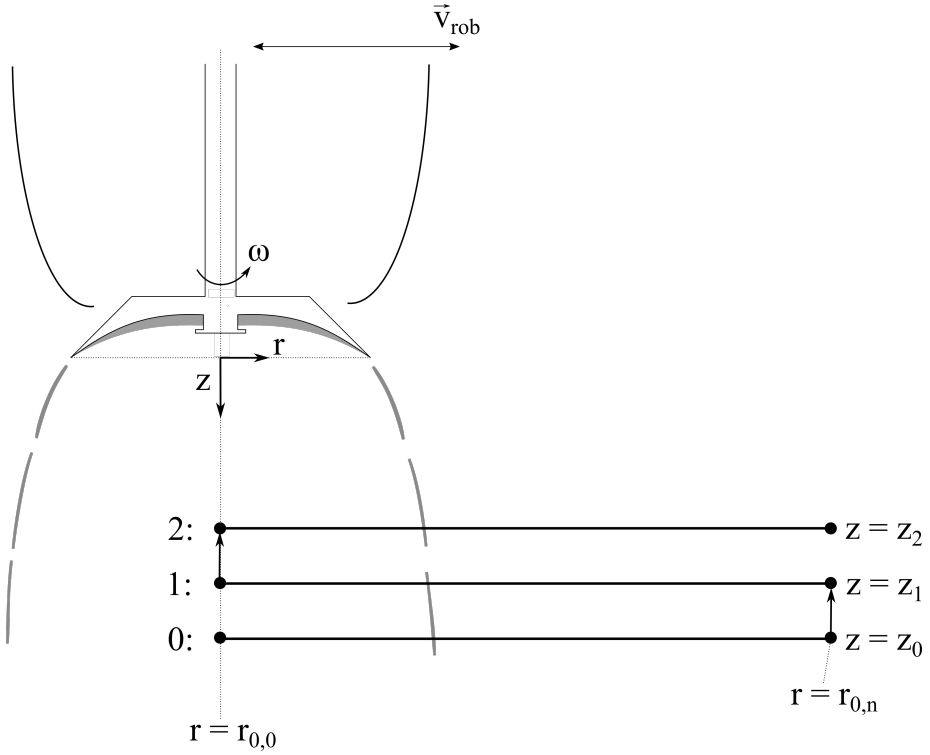

Figure 3.9: Traversing measurement method. Step-wise or continuous traversing route measurement. Measurement time is defined by path length and atomizer velocity $t_{meas,z_i} = (r_{i,n} - r_{i,0}) \cdot v_{rob}^{-1}$.

tion of time of detection and the time dependant atomizer velocity defined in the robot–arm control sequence. For a traversing measurement to be considered valid, the count rate has to start at zero outside the bell, has to reach a maximum while traversing and has to end at zero again. This represents a full cut through the spray cone along the axis, which can be moved or elongated if one of the data rate criteria is not met. The results can be weighted according to the corresponding spray cone cross sections by use of non–uniform atomizer velocities. Alternatively, the size of radial segments can be fitted to equal size rings by subsequently decreasing the averaging integral boundary width. This is a more defined variation of the area–specific averaging already described in section 2.6.4. Instead of a variation of the cross–sectional areas, the relative velocity of the atomizer head can be varied, so that the residence time within each section decreases with the area of the radial segment.

3.5.2 Standardized measurement method

Utilizing AOM's SpraySpy® device, a standardized method was developed and verified using PDA comparison by means of traversing measurements. The TS device remains at the project partners facility and is used on a regular basis by different users for both quality control and R&D purposes.

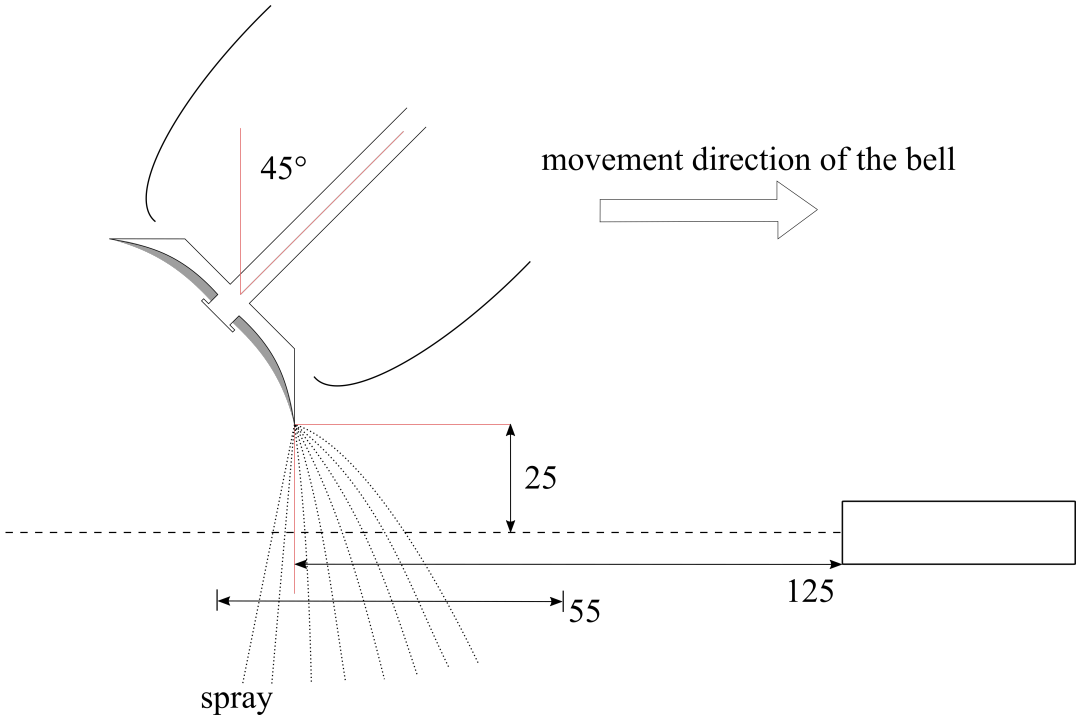

Figure 3.10: Standardized measurement scheme for TS traversing measurement (Wigger et al., 2021). Reference values are given in [mm].

The SpraySpy® (f = 125 mm) is mounted to the socket via the rack, while the painting robot (ABB IRB 5400 with DÜRR EcoBell2) traverses along a 55 mm measurement axis with a bell/atomizer inclination angle of 45 degrees (see figure 3.10). The tilt of the atomizer increases the vertical component of the diverging spray cone in regards to the measurement devices, thus increasing validation rate slightly. Additionally, the inclination enables measurement closer to the bell edge without painting of the optics.

The axis starts underneath the center of the bell, approximately 15 mm inside from the bell edge and ends 40 mm outside the bell. The measurement starts

after initial calibration of the robot and the device to one another by moving the tilted atomizer towards the device until the measurement volume reaches the point below the bell center. A constant movement velocity of 2 mm/s is considered to be optimal, regarding the data ratios and material consumption. A lower velocity (increments of 0.5 mm/s possible) does not yield a sufficiently higher detection count to justify increasing the needed quantity of testing fluid.

Per sample, two measurements are performed, obtaining data for transparent (refractive part of the spray) and non-transparent particles (reflective part of the spray). The SpraySpy® device is capable of switching between both scattering light analysis modes without hardware reconfiguration, effectively enabling a simple repetition of each measurement with a switch in the software presets. A thorough investigation in the degree of transparency for each individual detection is not possible due to inhomogeneity of the spray and invalid detections being discarded directly. The ratio of validated transparent detections to the total number of transparent and opaque detections is used as a measure of spray homogeneity. The validity criterion for the measurements (zero–to–max–to–zero, section 3.5.1 and figure 4.19) can be checked in–situ in the user interface of the software. Reproducible results are achieved using this method.

The obtained results are nearly identical to PDA-measurements using the same principle for reflection (see figure 3.11). Distances are adjusted according to the focal length of the PDA lenses. The use of the PDA device enabled the definition of the standardized method by means of validating the measurement results with two different methods for the same spray. The detection of a larger number of smaller droplets for the PDA is due to the higher laser power and the greater receiving aperture.

The results of this method development and the definition of the standardized method are published in U.S. Patent 20210262911 (Wigger et al., 2021).

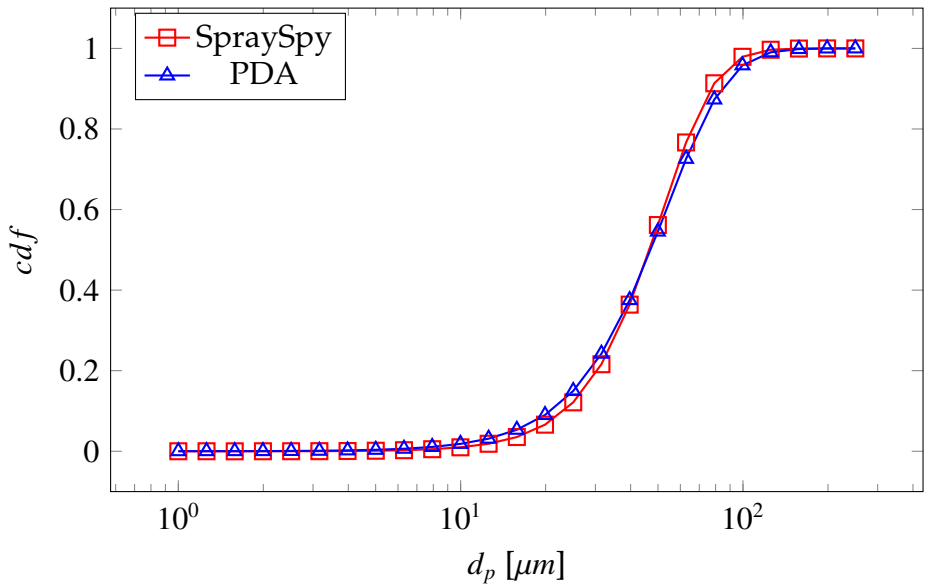

Figure 3.11: Exemplary comparison of the number distribution results obtained with TS and PDA after optimization of settings for both devices and measuring under the standardized method. Minimal shift to finer fractions for PDA below median and inverse behaviour above. M1. $\mathrm{Re} = 1.17 \cdot 10^4$, $\mathrm{We} = 12.6$, $\Pi_7 = 1.18 \cdot 10^{-2}$, $\alpha_1 = 87.0$, $c_1 = 2.8$, $k_1 = 4.3$, $\alpha_2 = 104.835$, $c_2 = 2.384$, $k_2 = 5$

4

Results and evaluation

4.1 Visualization of the flow field

The characteristics of the flow field below the bell can be captured by high speed imaging and cross sectional velocity measurements. A schematic presentation of the resulting flow structure inside the stable upper part of the spray cone is shown in figure 4.1. Due to high tangential and radial acceleration below the bell edge, a rotating tubular vortex forms. Outside and above the edge of the bell secondary smaller tubular vorteces form. This can be observed during the atomization process, but has not been measured during the trials.

After a certain distance, mostly dependant on application parameters, the flow below the tubular vortex becomes unstable and propagates away from the bell edge and towards the substrate (see Scholz, 1998).

In consequence, depending on the r and z coordinates, there are significant inhomogeneities of the measured droplet diameters over the radial direction (see Illner, 2017, chapter 4.4 and 4.6). At sufficiently large distances from the atomizer bell (e.g. $z \leq -200$ mm), the mean diameters behave much more uniformly in regards to their radial distribution. With increasing distance from the bell the deviation for radial dependencies of droplet diameters is in the range of 10 – 15%. This is mostly due to remixing inside the spray cone after leaving the influence of the tubular reflux region below the bell.

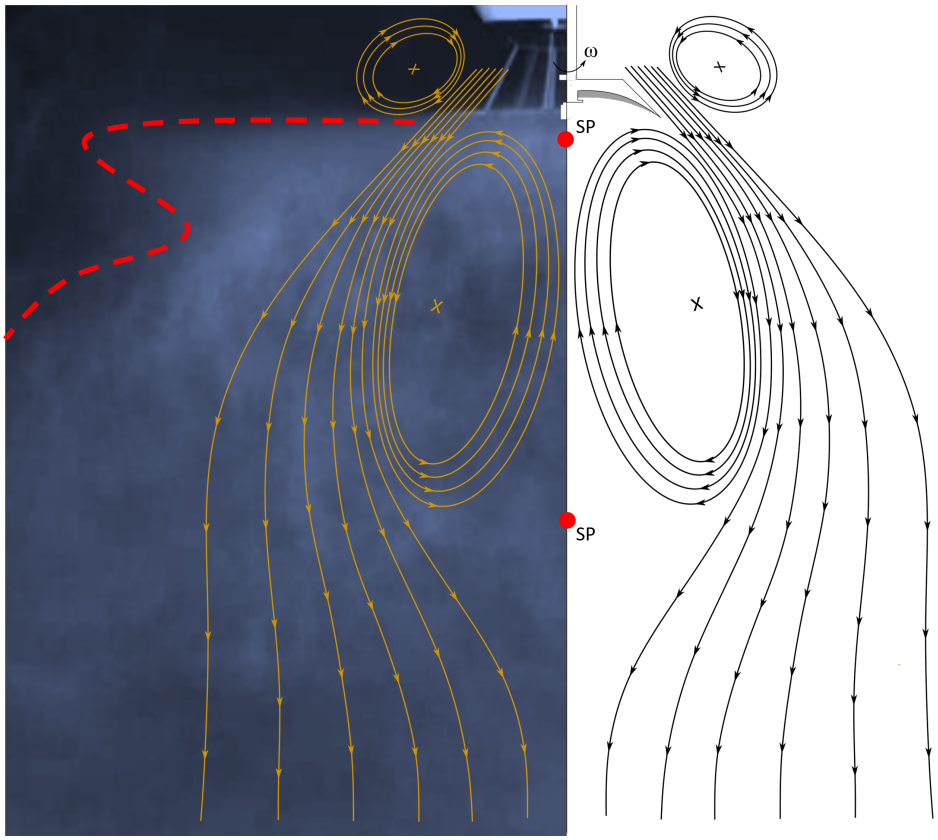

Figure 4.1: Schematic presentation of the flow field below the rotating bell. Rotational symmetry at the center axis. Tubular vortex structures in proximity of the bell. Outline of the spray cone shown as dashed line. Stagnation points on the center axis, as well as in front of a target substrate, if present.

4.2 LDA measurements of the flow field

Observing the droplet velocity profiles (figures 4.2, 4.3 and 4.4) shows, that with decreasing distances to the atomizer bell, positive vertical velocities $w(r, z)$ are measured in the inner area of the cone ($r < 60$ mm for the undisturbed flow, see figure 4.2). This local backflow, opposed to the main flow direction, is the result of a tubular vortex underneath the bell, driven by a locally low pressure in the center directly underneath the bell ($r = 0, z = 0$) due to centrifugal forces and the superposed shaping air jets. Increasing radial distance shows a decline of the back flow intensity, crossing the vortex and effectively leaving the inner vortex region. The change of the vertical flow direction can mostly be

observed for $r > 60$ mm, the outer half of the vortexm, after the vortex centre. The vortex in the interior of the cone and the associated backmixing are confirmed in the literature (Domnick et al., 2005 and Illner, 2017). After reaching a certain distance from the bell $w(r, z > 150mm)$ is negative in z-direction for all values of r. The maximum does not change its radial position with increasing distance from the bell, however, the flow does become more even after leaving the backflow region.

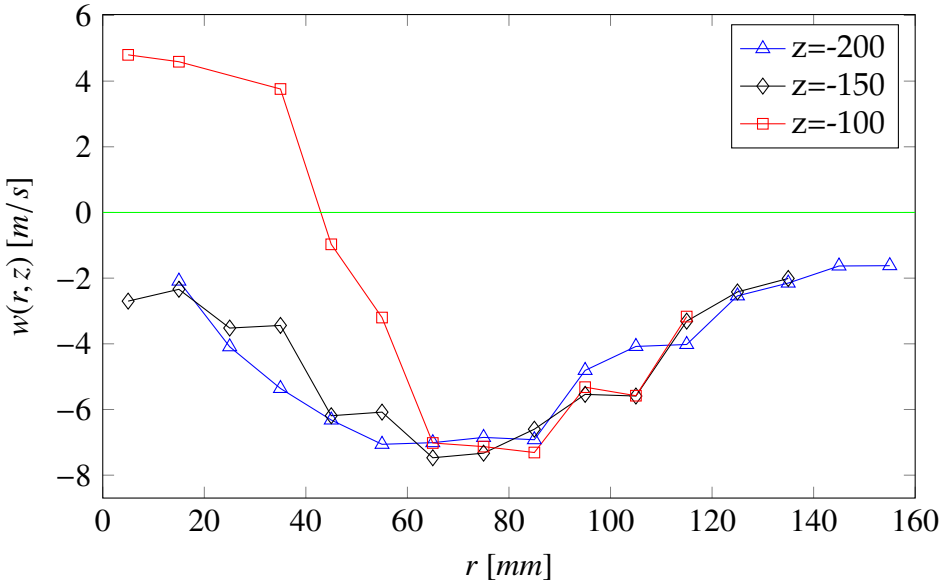

Figure 4.2: Median vertical velocities $w(r, z)$ for different vertical distances from the bell measured with LDA along a radial traversing axis. $\Pi_7 = 1.18 \cdot 10^{-2}$, M_0.

The exact positions of the velocity maximum and the center of the vortex structures change depending on the presence of a target substrate (e.g. stagnation flow), as well as with varying process and material parameters. The overall structure of the flow field, however, remains comparable and is well within the means of the before mentioned schematic presentation (see figure 4.1).

Radial velocity components $u(r, z)$ can be positive or negative depending on the measurement position inside the cone. The aforementioned tubular vortex is located in the range $-150\text{mm} < z < 0$ mm and $r < 80$ mm for the given parameter settings (red squared curve, figure 4.3). A flow in positive radial direction is visible below the bell, with a local maximum close to the bell edge.

After leaving the stable vortex region $-150\text{mm} < z$, the flow merges towards the center of the jet (e.g. streamlines in fig. 4.1), leading to slightly negative radial velocities. At the center of the cone radial velocities fluctuate around zero in both directions, indicating a breakup regime of the stable flow region.

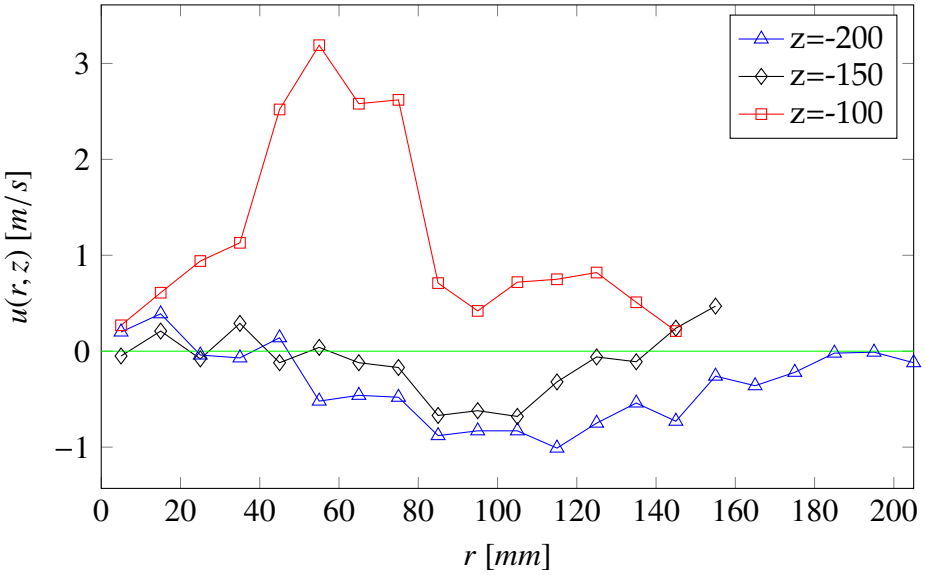

Figure 4.3: Median radial velocities $u(r, z)$ for different vertical distances from the bell measured with LDA. $\Pi_7 = 1.18 \cdot 10^{-2}$, M_0.

Tangential velocities $v(r, z)$ show a maximum for all z - distances at radial positions of about $r = 40 - 60$ mm (figure 4.4), which is at the edge of the bell, outside the tubular vortex. The tangential velocities approach 0 for $r \to 0$ mm and for large r. Due to rotational symmetry, the tangential velocity component does change droplet trajectories without altering the radial distribution significantly. The tangential velocities create a directly visible rotating flow structure.

The velocity profiles are obtained by measurements of small droplets, that almost perfectly follow the continuous phase for small Stokes numbers ($St << 1$). Due to the droplet size distributions, we certainly measure a deviation from the continuous flow velocity for detections caused by droplets which do not perfectly follow the continouus flow.

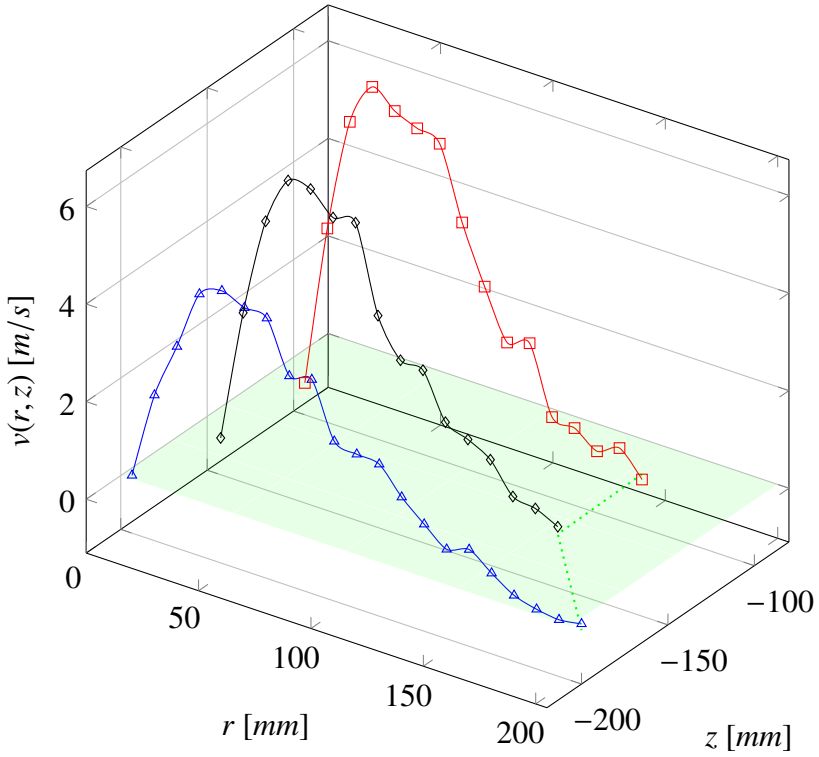

Figure 4.4: Median tangential velocities $v(r, z)$ for different vertical distances from the bell measured with LDA. The green surface indicates the zero velocity plane. $\Pi_7 = 1.18 \cdot 10^{-2}$, M_0.

It should be noted that the velocity profiles are measured without a target substrate, i.e. in a free jet. For a detailed case-specific modeling it is recommended to perform a dedicated measurement for the respective case in order to have an accurate data basis. It mostly becomes relevant in the outer region of the vortex at $z = -100$ mm and at $r = 50$ mm, as the flow field changes significantly in proximity of the solid substrate and locally high velocity gradients will appear, altering the droplet following behaviour and, thus, the trajectories.

The maximum non-averaged vertical velocity of individual droplets measured at $z = -200$ mm is 32 m/s, which is about four times larger than the maximum tangential velocity. The acceleration due to the amount of shaping air is the main factor here. The choice of nozzles and air rings on the atomizer changes both the swirl (tangential and radial velocity) and the vertical spray velocity. Depending on the application, a homogeneous velocity and droplet distribu-

tion for a free jet may be assumed for a distance of approximately 200*mm* from the bell edge.

4.3 Experimental determination of break–up values

The use of high resolution HSC imaging (see section 3.4) enables a variety of different analysis methods for the determination of ligament lengths, break-up diameter and the estimation of strain rates during break up. During the course of the project we established a method to analyze the individual and mean ligament lengths during the rotary bell atomization for serrated bell cups. The general procedure (described in detail in Oswald et al., 2019a) is shown in figure 4.5. After the raw image evaluation a more refined method using a skeleton method to determine individual ligament lengths in bulk, as well as ligament diameters can be applied. The obtained results by bulk averaging (Oswald, 2021) will not be discussed further in detail, but rather referred to if needed.

The summation and averaging of a large number of images delivers a mean overall ligament length, that can be obtained by analyzing the exact radial position, in regards to the center of the bell, of the maximum of the grey value gradient (see figure 4.7). However, the skeleton version (Oswald, 2021) delivers individual ligament lengths, as well as typical ligament length distributions (see figure 4.6). All ligament lengths used for the modeling (see section 4.6) are obtained by the developed skeleton method.

The optical determination of the ligament diameter during break up $d_{\mathrm{Lig,BU}}$ is impeded by resolution limitations, hence, relative uncertainties up to 50%, as well as motion blur due to high tangential velocities, resulting in illumination difficulties. Following an integral mass balance assuming equal fluid distribution between the serrations, the following expression can be derived

$$d_{\mathrm{Lig,BU}} = 2 \cdot \left(\frac{\dot{V}_l}{N_{\mathrm{Ser}} \cdot \pi \cdot u_{\mathrm{Lig,BU}}} \right)^{0.5} . \tag{4.1}$$

The volumetric flow rate $\dot{V}_l$ and the number of bell serrations (or ligaments) N_{Ser} are known. The radial and tangential velocity components of the ligament at its break up length, u and v, can be obtained following the kinematics of

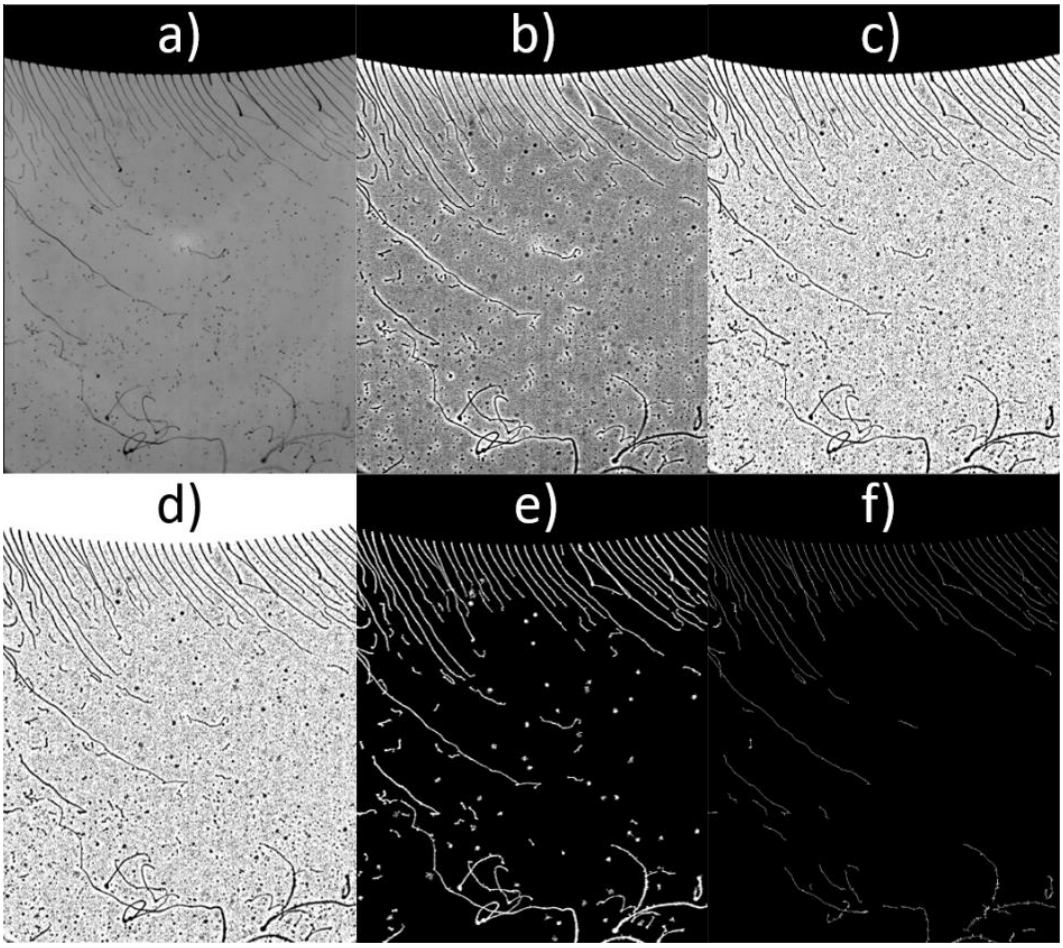

Figure 4.5: Step wise image processing: a) raw image, b) contrast enhancement, c) binarization, d) bell edge removal, e) inversion f) skeletonization (see Oswald, 2021).

the two–dimensional ligament discharge from a rotating bell. I.e. from two consecutive HSC images tracking a characteristic point of a ligament directly before or directly after disintegration (see figure 4.8) we obtain

$$u_{Lig,BU} = \left.\frac{\partial r}{\partial t}\right|_{BU} = \left.\frac{\Delta r}{\Delta t}\right|_{BU} = \frac{r_{BU,1} - r_{BU,0}}{t_1 - t_0}. \tag{4.2}$$

For two consecutive images the time difference Δt is the inverse of the image frame rate, here $\Delta t = \text{fps}^{-1} = 10^{-5}$s. For $\omega = 2094\ \text{s}^{-1}$, $\dot{V} = 200$ ml/min, $N_{\text{Ser}} = 480$, $R = 32.5$ mm, $1\ px \mathrel{\widehat{=}} 19.8\ \mu$m, 10^5 fps we obtain radial velocities in the range of

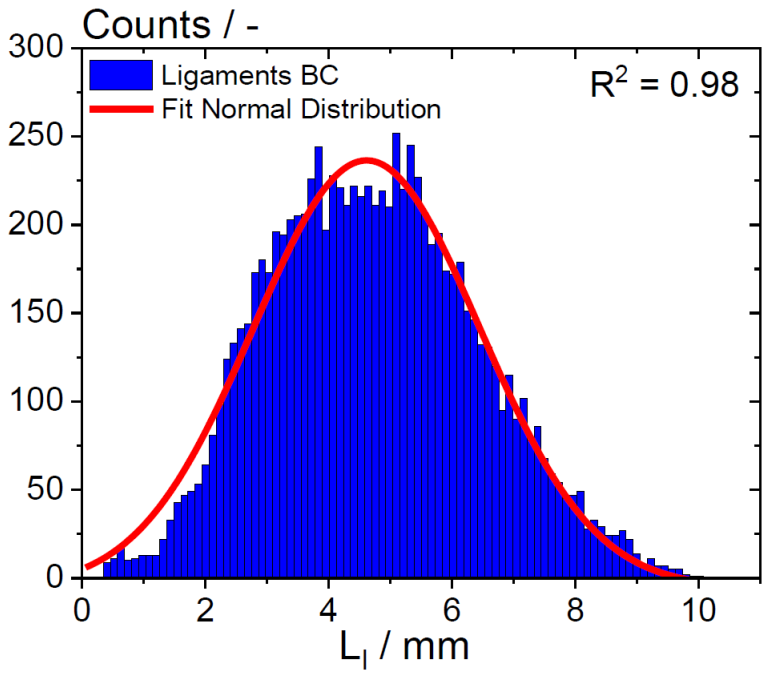

Figure 4.6: Typical probability distribution of l_{Lig} ($h_{\Delta l_1} = 0.16mm$) obtained by the skeleton method. The red curve is a normal distribution fitted to the experimental data (see Oswald, 2021).

$u_{Lig,BU} = 15.4 - 16.9$ m/s from analyzing multiple volume elements from different image pairs. Image resolution scaling is done by referring the tangential velocity at the bell edge $v_R = \omega R$ to Δt. Combining equations (4.1) and (4.2) yields exemplary break–up ligament diameters in the range of $d_{Lig,BU} = 22.8 - 24.0\,\mu m$.

Extending equation (2.10) by increasing the radial length by l_{Lig} and using the radial velocity during ligament break up $u_{Lig,BU}$ delivers a good approximation for the actual strain rate during the ligament break up, i.e.

$$\dot{\varepsilon}_{BU} = \frac{(R + l_{Lig}) \cdot \omega^2}{u_{Lig,BU}} = 8.8 \cdot 10^3 - 10^4 s^{-1}. \tag{4.3}$$

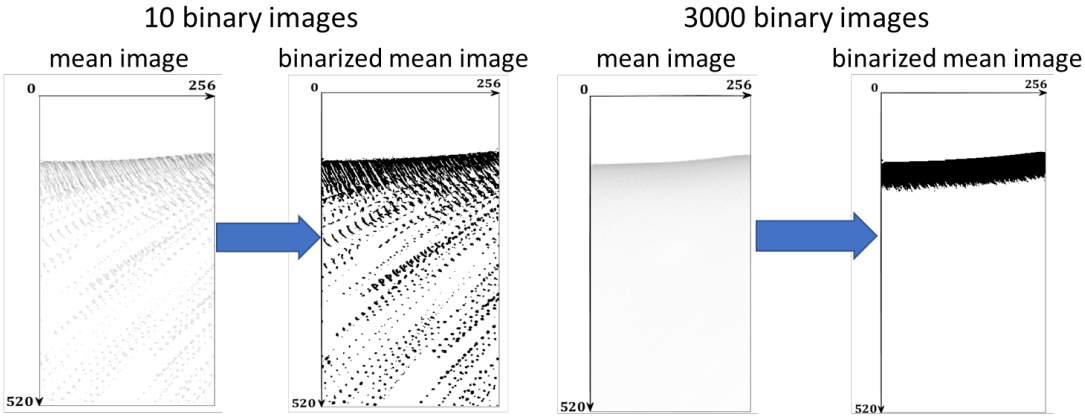

Figure 4.7: Summation of binarized images with subsequent averaging of grey values. Average ligament length visible in the image on the right (image provided by Oswald, W., 2020).

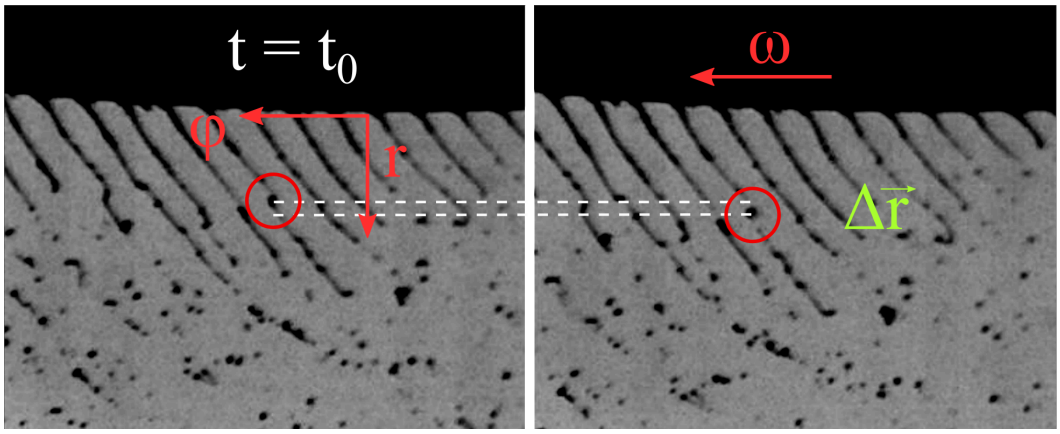

Figure 4.8: Emerging ligament and a fluid volume element in proximity of the break–up length. Consecutive images of the bell edge for volume element tracking. $\omega = 2094\ \mathrm{s}^{-1}$, $\dot{V}_l = 200$ ml/min, $N_{\mathrm{Ser}} = 480$, $R = 32.5$ mm, 1 px $\widehat{=}$ 19.8 μm, 10^5 fps, M_0.

4.4 Data evaluation – MATLAB and BSA postprocessing

The ideal ratio of phase differences is defined by geometric and aperture mask setup (see subsections 2.9.2 and 4.4.2). We accept certain deviations from this

ideal behavior, as research shows that sphericity can be assumed for a tolerance $\mathbb{S}_{tol}$ in the order of 10% (Onofri et al., 1996).

The software extension for particle analysis provides a wide variety of tools for droplet and particle size evaluation. However, this is limited to the selected sphericity tolerance value, as all invalid detections are discarded. Therefore, a subsequent change of sphericity tolerance value is impossible when using the BSA Flow software particle size analysis package. The subsequent analysis of the measured raw data (see table 4.1) is performed with a self–written MATLAB code (Illner, 2017 and Vetter, 2018) to obtain global information or clustered data sets for variable radial segments of the spray cone for count number, vertical spray velocities, size distributions and diameters. For the PDA measurements, a variation of validation tolerance is possible with the self–written code, enabling the analysis of sphericity influences in detail.

Table 4.1: PDA raw data format as provided by BSA Flow software

running index	**arrival time**	**transit time**	**velocity**	Φ_{12}	Φ_{13}	**droplet diameter**
[−]	[ms]	[ms]	[m/s]	[°]	[°]	[μm]
1	1648.861	9.4	-8.53	18.9	6.0	14.8
...	...	...	...	...	...	...
i						

The raw data obtained by the PDA system is exported as a .csv–file or a column separated .txt–file for each measurement point or for one traversing measurement. The algorithm scheme is shown in figure 4.9. After the initialization of the code, the parent folder of the data set is defined and the raw data is imported as an initial $i \times 7$-matrix M_o.

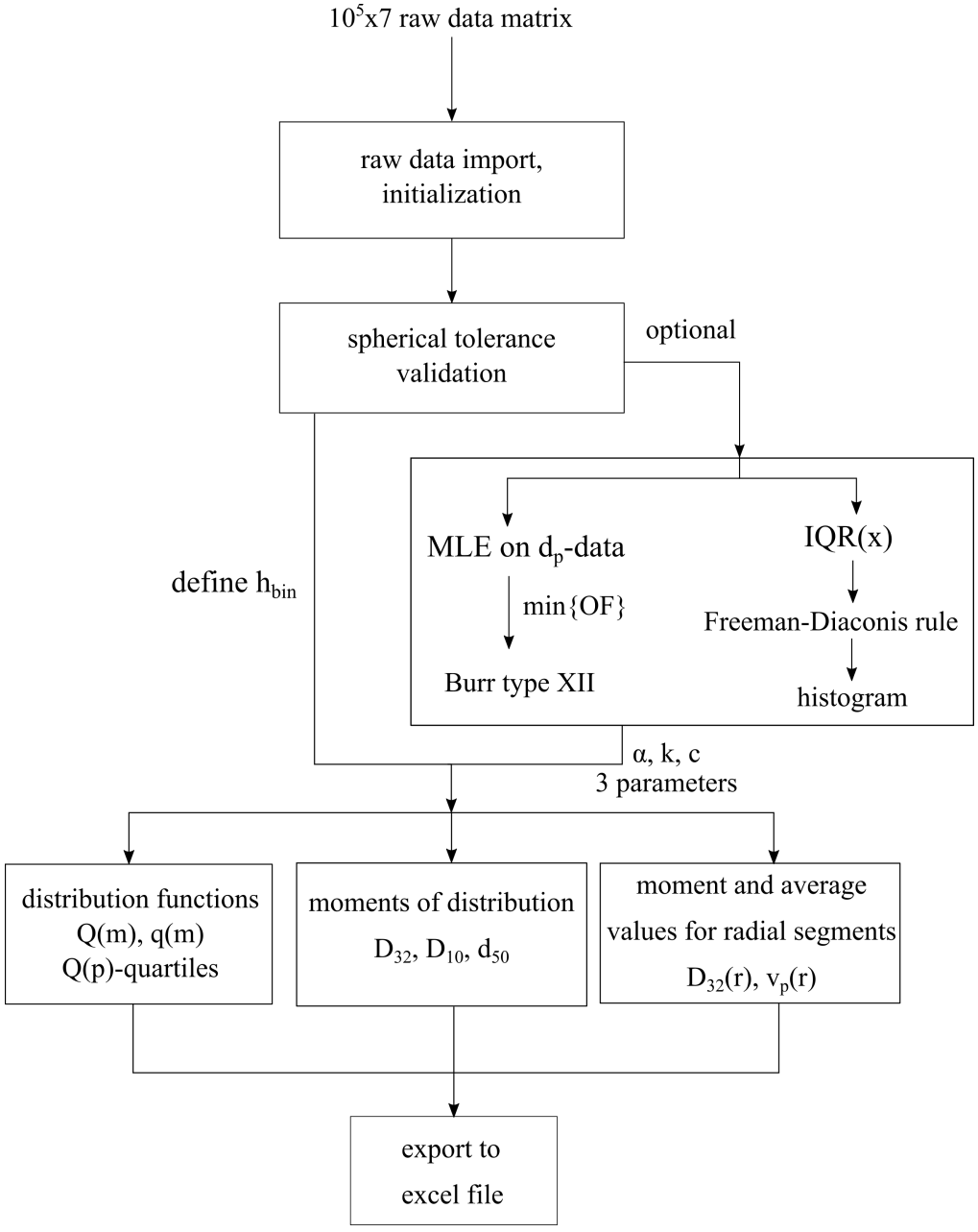

Figure 4.9: Algorithm for raw data refinement with post processing under variable sphericity tolerance

The first step is spherical validation, which is dependant on the front mask of the receiving unit, defining the ratio of phase shifts due to geometry (see section 3.2.2).

The slope of the ideal line is known for each mask, e.g. for mask B we have

$$\widehat{\Phi}_{ideal,B} = \left.\frac{\Phi_{12}}{\Phi_{13}}\right|_{ideal,B} = 2.5625. \tag{4.4}$$

To define a tolerance level, the distance from the ideal line in the phase plot (Φ_{12} over Φ_{13} plot, see figure 4.10) for each detection is limited. Increasing the tolerance, unsurprisingly leads to a higher validation rate while increasing the measurement uncertainty simultaneously.

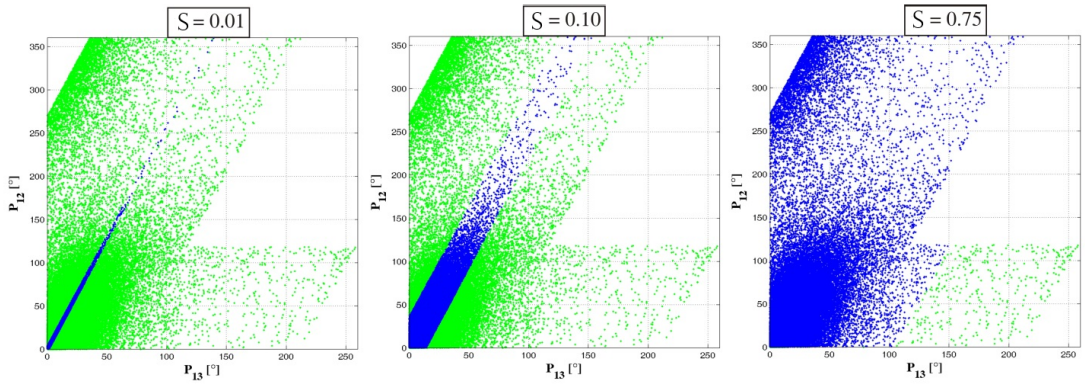

Figure 4.10: Phase plot for different sphericity tolerance values $\mathbb{S}_{\text{tol}}$. Validated droplets (blue) within the tolerance level are further processed. The slope is dependant on the type of mask used. See equation (4.4). Green dots are invalid detections.

This yields a $(i-j)\times 7$ matrix, reduced by all detections outside of the tolerance band, as well as all entries equal zero. For the TS, the data is already cleared of invalidated detections. A variation of tolerance levels is not intended for the user. Overall distribution parameters, mean values and moments, individual quantiles can be calculated from the obtained Burr Type XII functions.

Applying a maximum likelihood estimator (MLE) algorithm (Hedderich and Sachs, 2016, Saei et al., 2019, Wingo, 1983 and Wingo, 1993) the three parameters of the Burr Type XII function (α, k, c) are obtained from the refined droplet diameter data for each individual distribution. The MLE implemented in MATLAB finds these parameters by minimizing the negative log–likelihood

function (objective function OF):

$$min\{\mathrm{OF}\} = min\left\{-\log \prod_{x \epsilon X} P(x \mid \alpha, c, k)\right\}. \tag{4.5}$$

Erroneous raw data sets, for which no viable parameters can be fitted are discarded for the algorithm distribution fit and have to be analyzed manually.

Individual histograms are fitted using the internal functions in MATLAB. The Freedman-Diaconis rule (equation 2.30) used to define bin width and number of bins is based upon the interquartile range which is calculated by linear interpolation. The droplet sizes are stored in an array which is sorted by size and assigned to the $\frac{0.5}{n}, \frac{1.5}{n}, \ldots, \frac{[n-0.5]}{n}$ - quantiles. Probabilities for quantiles in between the basis values are interpolated (Langford, 2006). Not relying on the distribution function fit enables the calculation of histogram properties even when fitting the expected distribution function to the raw data fails. Subsequently the reprocessed matrix is used to calculate the following data per sample:

- count, volume and velocity histograms,
- radial segment histograms of droplet size,
- radial segment counts,
- radial segment size distribution moments (D_{10}, D_{30},D_{32}, d_{50}),
- threshold (e.g. $< 150\ \mu$m) droplet size comparison (D_{10}, D_{30},D_{32}, d_{50}),
- space-resolved individual droplet sizes and velocity.

The algorithm is equipped with an automatic identifier for available read-files that leads to a loop for individual raw data files. After evaluation with the given specifications, an .xls-file is exported (or newly created for the first export) and subsequently extended for each individual raw data file. Summarized post processing data can be accumulated in an overview sheet. Confidence intervals for the MLE parameters can be exported, however the use for the present study is unclear and will be referred to in section 4.7.

4.4.1 Phase–ratios and sphericity tolerance variation

The Dantec PDA software BSAFlow provides a variety of presets and setting options for the P60 burst spectrum analyzer. Geometric relations and hardware settings are essential to calculate droplet velocity and droplet diameter according to equations (2.34) and (2.35). This section deals solely with measurement results obtained with the PDA.

The standard sphericity tolerance $\mathbb{S}_{tol}$ is 10% for most applications. Variation of this value during post processing shows clear tendencies for the observed sprays. Reducing $\mathbb{S}_{tol}$ to values below 10% drastically diminishes the validated count numbers during measurement (figure 4.11).

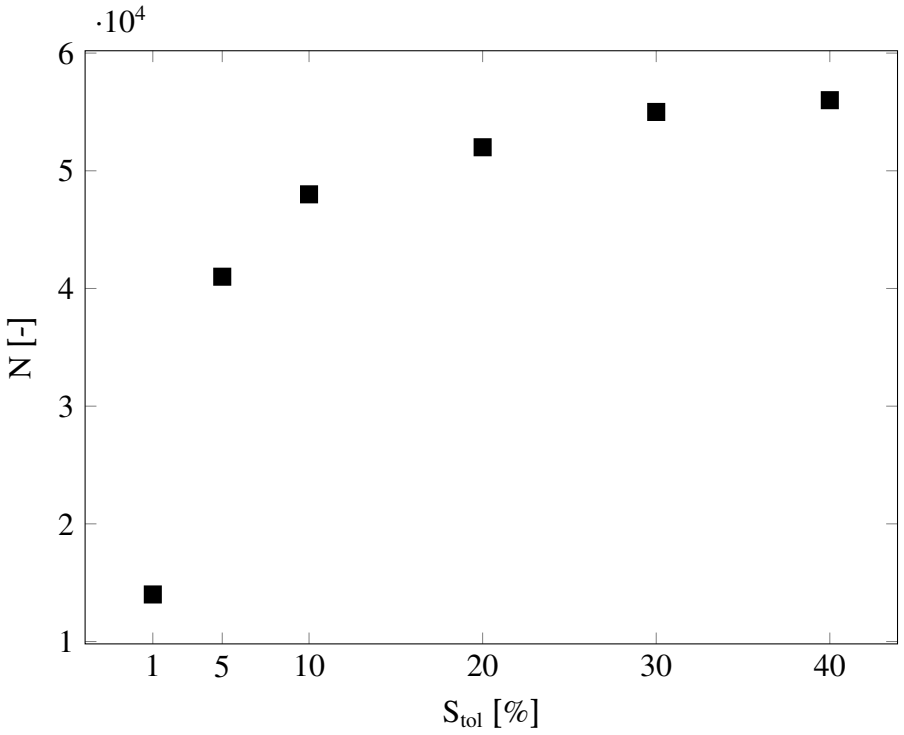

Figure 4.11: Total count numbers for PDA-measured droplet size number distributions after MATLAB processing as function of sphericity tolerance $\mathbb{S}_{tol}$. Re = $1.17 \cdot 10^4$, We = 12.6, $\Pi_7 = 1.18 \cdot 10^{-2}$, material M_1.

Rejecting disturbed signals, either due to non-ideal light reflection or due to non-spherical shape leads to lower data rates by lowering the validation rates while increasing the measurement security for spherical droplets. For

$\mathbb{S}_{tol} > 20\%$ no significant increase of validated droplet numbers can be found. A larger number of valid droplets increases the statistical certainty (see section 2.7) for the pay-off of accepting more non-spherical droplets. High-speed imaging shows that ligament fragments are partially discarded and form droplets besides the ideal break-up process. Larger droplets are prone to deformation by acceleration as the ratio of inertial and capillary forces increases (We increases).

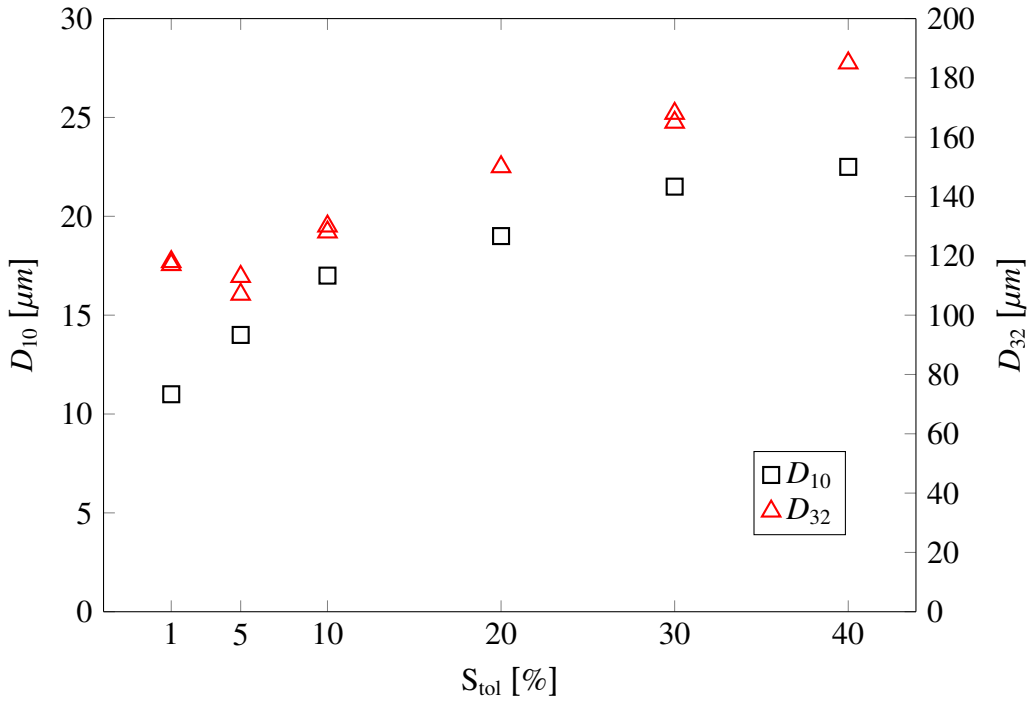

Figure 4.12: Number mean average diameter (D_{10}) and Sauter mean diameter (D_{32}) for PDA-measured droplet distributions after MATLAB processing as function of sphericity tolerance $\mathbb{S}_{tol}$. Re = $1.17 \cdot 10^4$, We = 12.6, $\Pi_7 = 1.18 \cdot 10^{-2}$, material M_1.

Lowering the tolerance rate $\mathbb{S}_{tol}$ performs a biased cut off at the upper end of the size spectrum. Nonetheless, droplets with $d_p > 250\,\mu$m can be observed for $\mathbb{S}_{tol} = 1\%$, hence, the decrease of count rates leads to an increase of statistical uncertainty, which is directly visible for D_{32} (figure 4.12, $\mathbb{S}_{tol} = 1\%$). Increasing $\mathbb{S}_{tol}$ is unbiased for D_{10} or D_{32} for $\mathbb{S}_{tol} < 40\%$. Further increasing the validation

rate leads to erroneous measurements of droplet sizes due to the Gaussian beam effect (Albrecht et al., 2014).

In conclusion it can be said that a sphericity tolerance of $10\% < \mathbb{S}_{\text{tol}} < 20\%$ is ideal to analyze opaque paint sprays during rotary bell atomization.

4.4.2 Influence of mask variation

Early measurements with the PDA (Mask B) and the SpraySpy® system show a non–negligible amount of droplets larger than 320 μm. These droplets can also be observed using high–speed imaging and are detectable on painted substrates and periphery with microscopic analysis. Thus, these large droplets are no false detection or data evaluation artifact.

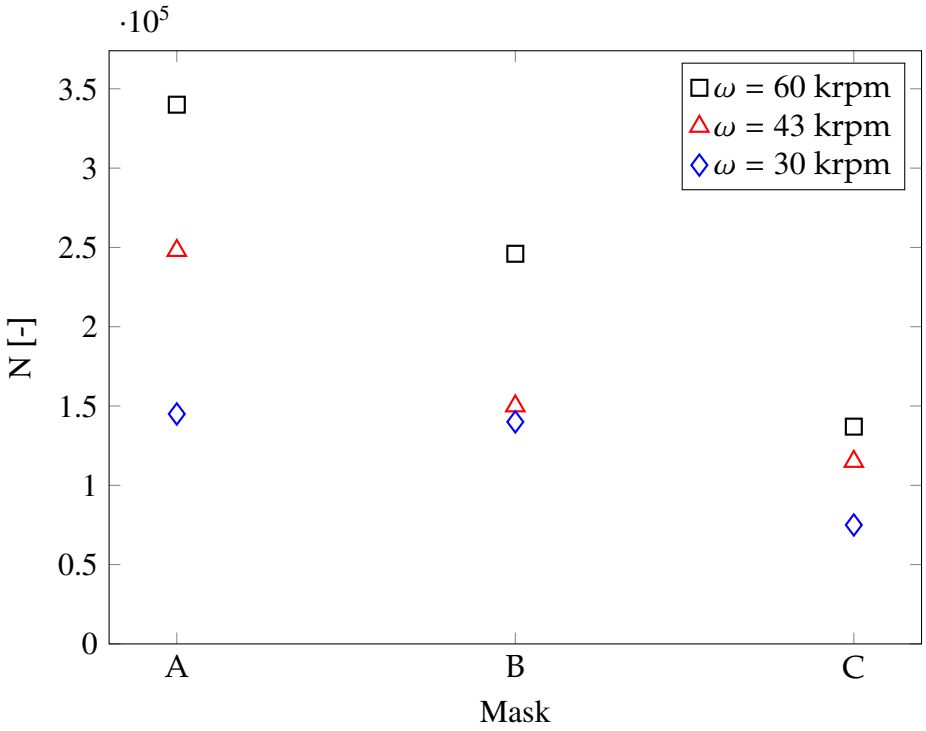

Figure 4.13: Total validated counts for the variation of masks A/B/C. EcoBell2, bell speed $\omega = 30/43/60 \cdot 10^3$rpm, $\dot{V}_l = 350$ ml/min. Material M_0, dark grey base coat.

Mask A is not capable of measuring these large droplets and the resulting distributions are biased towards smaller droplets. Neither the PDA (Mask C) nor the SpraySpy® measure a significant number of particles larger than 500 μm. Mask C under-represents the small particle fractions while having significantly lower data rates (see figures 4.13, 4.14 and table 4.2). The change in measured particle size distributions between Mask C and Mask B is significant for particles smaller than $d_p < 20\ \mu$m.

Table 4.2: Maximum detectable particle/droplet sizes for the Dantec PDA measurement apertures. Validated counts and resulting mean diameters. EcoBell2, bell speed $\omega = 43 \cdot 10^3$rpm, $\dot{V}_l = 350$ ml/min.

material	mask	counts [-]	max. meas. d_p [μm]	D_{10} [μm]	D_{32} [μm]
H_2O	A	340810	157.4	15.7	34.4
H_2O	B	245260	214.9	22.3	39.9
H_2O	C	140118	155.8	24.9	38.1
M_0	A	132232	235.6	14.7	43.6
M_0	B	89722	380.9	18.6	60.2
M_0	C	7345	897.2	28.2	61.8

Therefore, there is no significant loss of information for the larger droplet fractions by using Mask B for typical rotary atomizer sprays. Mask C on the other hand lacks information for the fine fraction. This, however, is nearly unnoticeable within the volume distribution compared to Mask B.

Mask B is the optimal choice to fully capture all relevant size fractions of the analyzed paint sprays (M_{0-3} and S_{1-5}). However, special applications might need more precise data for fractions on either end of the appearing size spectrum, which can be investigated by simply changing aperture masks and adapting the software parameters accordingly.

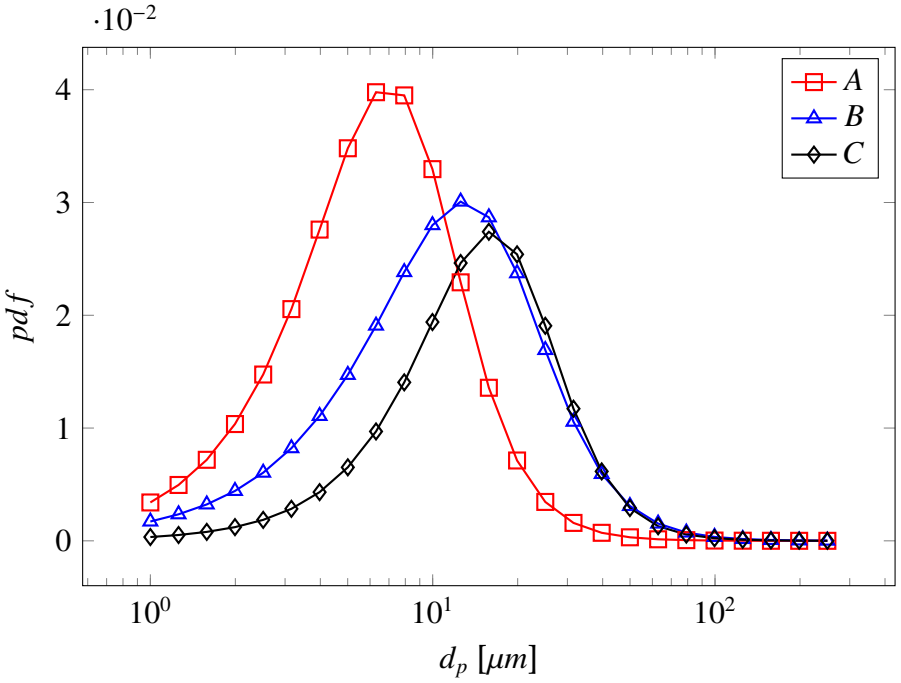

Figure 4.14: PDA measured number size distribution for droplet diameters. EcoBell2, R = 32.5 mm serrated cup, speed ω = $43 \cdot 10^3$rpm, $\dot{V}_l$ = 350 ml/min. Material M_0, dark grey base coat. α_1 = 9.4573, c_1 = 2.6515, k_1 = 0.4987, α_2 = 18.8678, c_2 = 2.3856, k_2 = 0.7948, α_3 = 20.9973, c_3 = 2.8590, k_3 = 0.7115.

4.5 Influence of pigments, material and process parameters

4.5.1 Influence of pigmentation on measurability and atomization

Most conventional coatings have shown to be measurable both with PDA and TS, depending on the type and concentration of added pigments and the incorporating base liquid. Clear base coat, the investigated Sterocoll mixtures and different paints with varying pigmentations behave differently in terms of atomization and measurability.

Figure 4.15 shows the influence of different added solid components to the basic clear coat material, as well as the complete coating material. Generally, a

decline in count rates is to be expected when altering the composition of the atomizing fluid that serves as the reference fluid during setup of the devices. During the experimental setup for a target liquid all settings are chosen optimally by preemptive measurements, thus leading to a semi–iterative process of refinement. These fine–tuned settings are always liquid specific and work within an acceptable range of deviations. Strong changes in fluid properties and interaction with the light do alter the results for different measurements. The conventional coating material shows the highest validation rate, as the

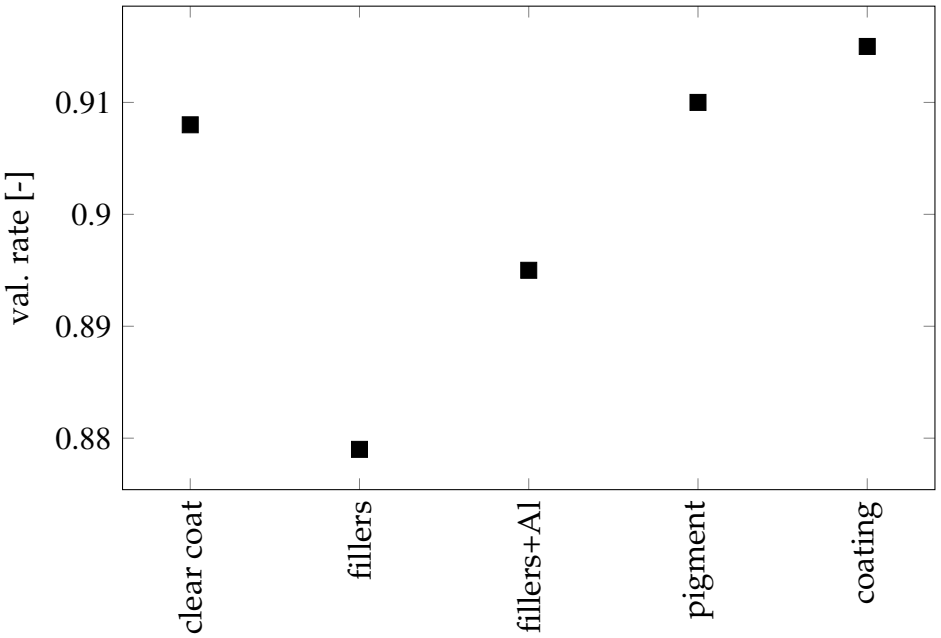

Figure 4.15: Variation of pigmentations from clear coat, clear coat with different additives to the complete paint.

setup is performed based upon ideal setting for pigmented paints, with the clear coat and the pigmented clear coat being comparable. The addition of fillers to the clear coat shows a stronger deviation for validation rates, which superimposes on the aluminum addition. Not all pigments and additives can be suspended in clear coat without different additives to account for wetting and clustering of the solids. In general the mean diameters are comparable for the pigmentation variants with a tendency of formation of larger droplets for the addition of fillers, aluminum and colour pigments (figure 4.16).

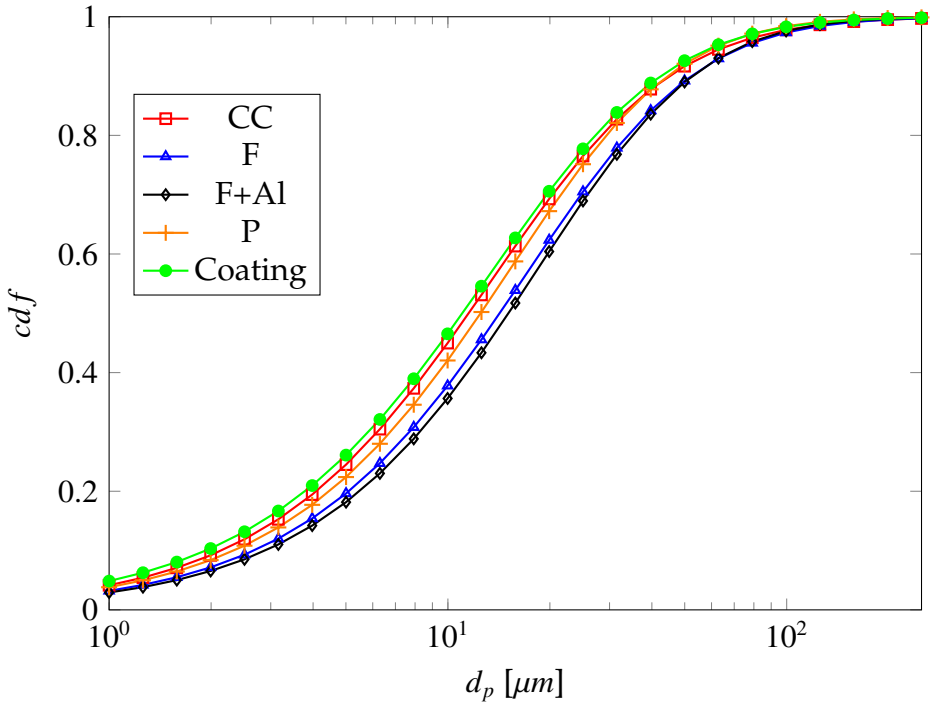

Figure 4.16: Cumulative distribution functions of clear coat and solid additive variations. Increase of the median diameter is below 5μm. D_{32} deviates between −5% and +14%. $\alpha_1 = 24.256$, $c_1 = 1.209$, $k_1 = 2.033$, $\alpha_2 = 36.116$, $c_2 = 1.201$, $k_2 = 2.455$, $\alpha_3 = 45.326$, $c_3 = 1.201$, $k_3 = 2.93$ $\alpha_4 = 30.64$, $c_4 = 1.148$, $k_4 = 2.571$, $\alpha_5 = 37.873$, $c_5 = 1.184$, $k_5 = 2.912$.

Validation rates of different fluid compositions do not behave uniformly during the measurements (see figure 4.17). Increasing the aluminum content improves the validation rate for clear coat while decreasing it for M_3 as base fluid. A reliable dependency on droplet diameters can not be found in the data, thus, we conclude that there is no bias for the calculation of D_{10} and D_{32}. However, as validation rates and absolute data rates change for different compositions it is necessary to ensure that local minimum count rate requirements are met. Decreasing the traversing velocity and/or a single repetition of the measurement can be sufficient to solve the problem.

A detailed analysis of the influence of different effect pigments and the resulting interactions with various clear coat compositions can be found in the work of Vetter (Vetter, 2018).

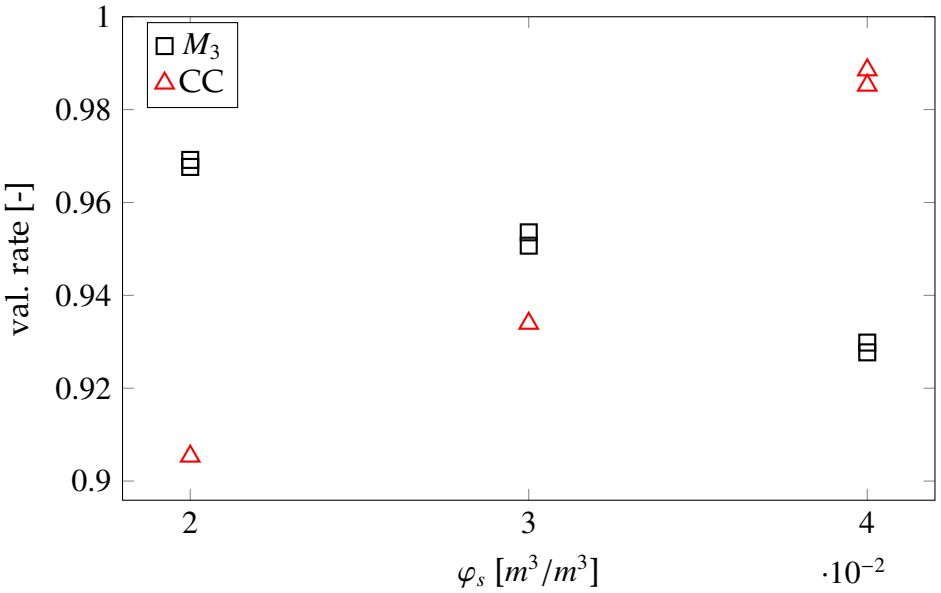

Figure 4.17: Change of validation rates for M_3 and clear coat depending on the amount of added aluminum particles.

4.5.2 Separation effects

Depending on material properties and process parameters the shape of the spray cone changes, widening up or narrowing down, exerting a change of local spray density (figure 4.18) and, depending on the paint bulk composition, of pigments and paint component distributions.

In extreme cases (e.g. high rotational speeds and short bell–to–substrate distances) centrifugal effects lead to a separation of the ideally mixed paint into two major fluid fractions: a low–pigmented nearly transparent finer fraction (T) and a heavily–pigmented non-transparent coarser fraction (NT). Substrate spray deposition trials and subsequent material analysis show non-linear depletion and enrichment behaviour of different solid additives in the liquid phase. Based upon the carrier liquid properties and process parameters, this leads to two similar but distinguishable spray components (see figure 4.19 T/NT, for more detail see Vetter, 2018 and Wigger et al., 2021). As shown by Illner, 2017 and Vetter, 2018 a radial distance dependency for count rates (e.g. spray density), local droplet sizes and T/NT - ratios for TS measurements (see figure 4.19) is found for various parameter combinations. The TS-measured

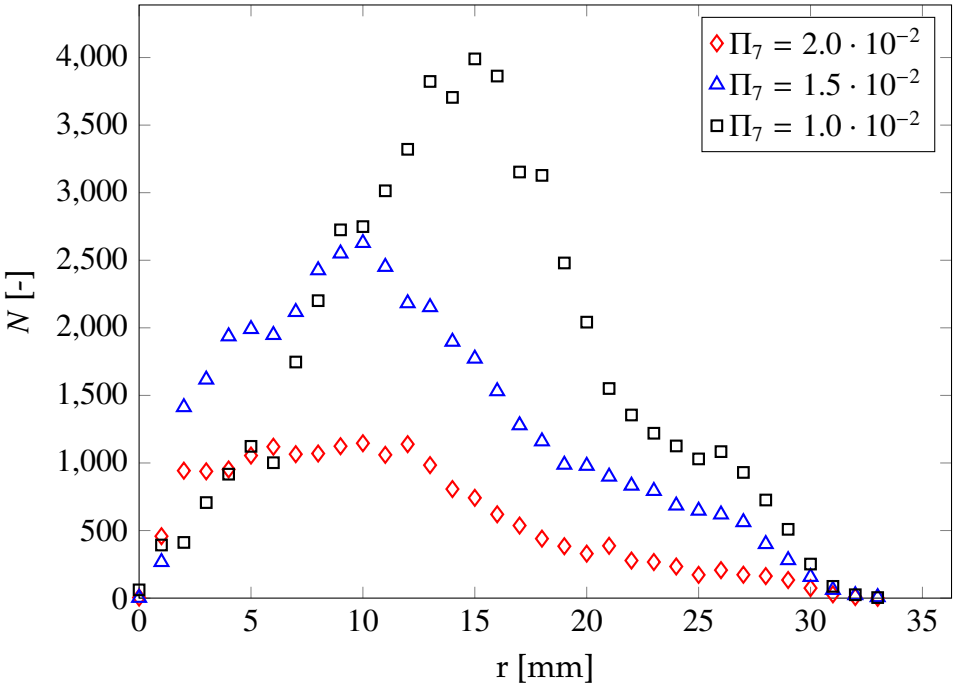

Figure 4.18: Count number N over radial distance r. Increasing bell speed increases count number and shifts the dense spray region in positive radial direction. Measured with PDA according to section 3.2.2.

transparent fraction is typically of smaller mean diameters and therefore be found closer to the center of the spray cone.

The sum of the individual radial distributions for both fractions (T/NT) measured subsequently with the TS device, without changing the experimental setup, is approximately equal to the distribution measured with the PDA. Both measurement methods establish the total maximum of the spray density at identical locations. The individual fractions T/NT do shift left and right off–center for TS measurement compared to PDA. The PDA measurement for small radial distances delivers a slightly higher relative count rate than for the TS measurement. As shown before (c.f. figure 3.11) the PDA does detect finer fractions slightly better. Both, PDA and TS do measure smaller droplet mean diameters for small radial distances from the center of the spray, underlining the initial assumption of an increase of spray coarseness with increasing r and, thus, with increasing degree of pigmentation and solid content. As of know

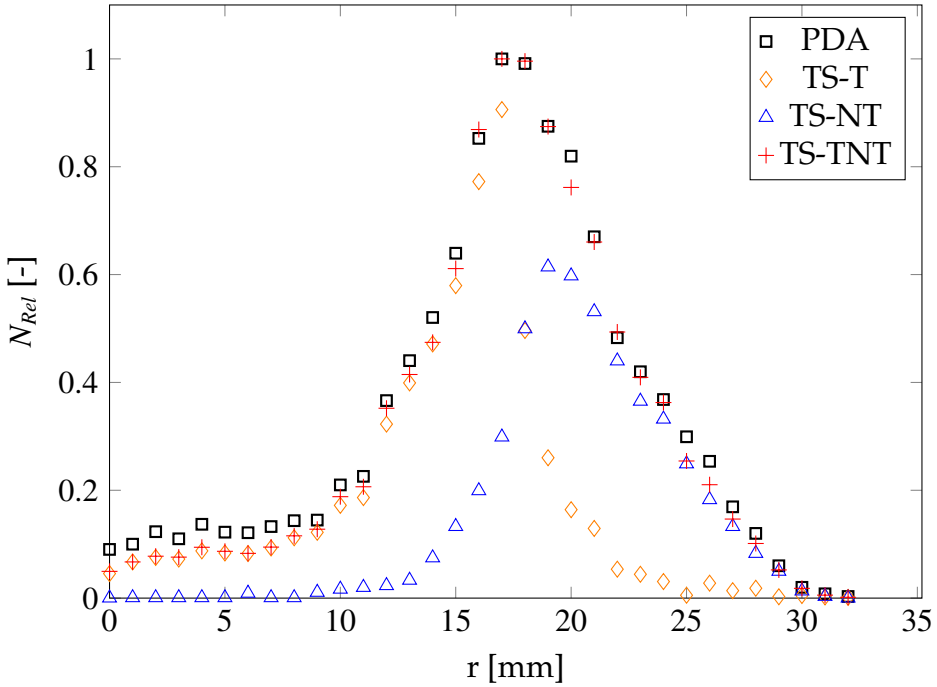

Figure 4.19: Radial distribution of relative amount of validated counts. General shape is valid for all analyzed sprays. Maximum count number per radial segment and T/NT curves shift depending on the operating parameters and material properties.

the TS is incapable of detecting the backflow towards the bell from the tubular vortex with the given setup, as it is direction dependant for the droplet detection (here flow direction from bell towards the substrate) in contrast to the PDA, which is capable of detecting droplets passing the measurement volume in both vertical directions and does so for small *r*-values.

The D_{32} is more sensitive to local data rate changes, spray flow fluctuations as well as the appearance of single large droplets than the D_{10}. This is directly visible in figure 4.20.

With the continuous increase of local data rates, or validated counts, the D_{32} becomes more stable, approaching a similar behaviour over r as the D_{10}. Again, this amplifies the necessity to cover the whole radial distribution spectrum of the spray for both PDA and TS-T/NT measurements. A shortened traversing measurement axis will inevitably alter the radial averaged (or global) mean

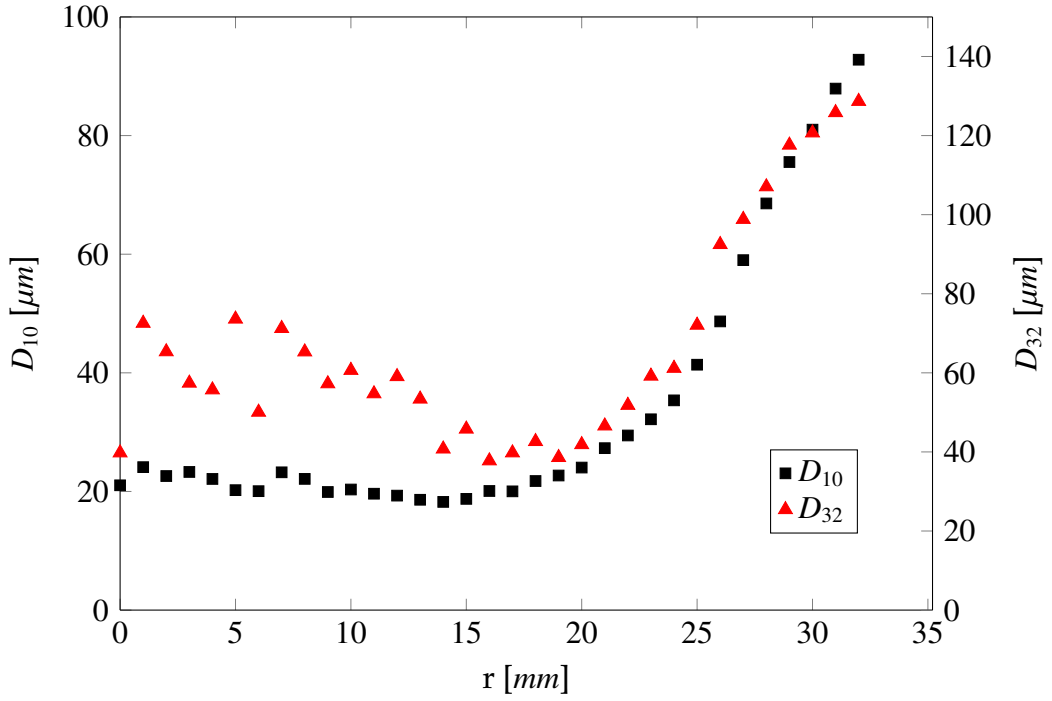

Figure 4.20: Radial distribution of D_{10} and D_{32} for a traversing measurement done in accordance to the standardized measurement method with PDA. General shape is valid for all analyzed sprays. Diameter values and radial position shift depending on the operating parameters and material properties.

droplet sizes due to a size–biased cut–off. In case of the radial distribution shown in figure 4.20, the locally averaged values may vary by a factor of three from minimum to maximum. However, for the typical coating process this is not a real issue, as turbulent flow remixing downstream of the vortex structures ($z \leq 200$ mm) homogenizes the droplet size distributions over r (Illner, 2017). This is further amplified by the spray cone movement optimization for transfer efficiency increase and spray cone overlapping during the automatized coating process.

4.6 Model development and uses in industry

Following the results of Buckinghams Π-theorem (see section 2.4) different generalized models can be approached by different combinations of the di-

mensionless groups. Ideally, the physics is captured correctly and the system can be described using these groups, defined as ratios of forces, pressures and characteristic time-scales, or their combinations. Equation (2.11) delivers a product of power-laws, i.e. the multiplication of the dimensionless groups powered with individual exponents enables simple mathematical modeling of physical influence parameters according to their exponent magnitudes. Note here that the dimensional analysis by itself does not deliver any functional structure for the modeling approach. However, known characteristics from experiments (e.g. viscosity plateaus, lamellae to ligament disintegration) help to structure the functional dependencies.

Modeling the dimensionless ligament length l^*_{Lig} and the droplet diameter d^*_p is imposed by several logical limitations. The general form of the function used must be able to reproduce the behaviour of the target value. Hence, we use

$$l^*_{\mathrm{Lig}} = f_1\left(\prod_{i>2} \Pi_i^{a_i}\right) \tag{4.6}$$

and

$$d^*_p = f_2\left(\prod_{i>2} \Pi_i^{a_i}\right). \tag{4.7}$$

A measured length or diameter can never be equal to zero, hence all groups, that can effectively become zero, used in a product of power laws for l^*_{Lig} or d^*_p, such as the solid content φ_s, have to be expressed in the general form of:

$$l^*_{\mathrm{Lig}} = (1 + \varphi_s)^{a_{\varphi_s}} \cdot g(\Pi_i) \tag{4.8}$$

and

$$d^*_p = (1 + \varphi_s)^{b_{\varphi_s}} \cdot h(\Pi_i). \tag{4.9}$$

For $\varphi_s = 0$ the corresponding term becomes equal to one, thus the influence in the product of powers disappears. This implementation of the solid content is a first approach to incorporate the influence of the solid particles for the product of power laws. This leads to an atypical order of magnitude for the exponents of the $(\varphi_s + 1)$ $-$ terms (Π_i, see equations (4.10) to (4.12)). Usually these exponent values range are in the order of -5 to $+5$. Due to the small

values of φ_s this leads to $\varphi_s + 1 \approx 1$, therefore to unusually large exponents for the different dependencies.

Of course this is limited to generally similar and thus comparable processes of ligament break up and droplet formation. Reducing (e.g.) the bell speed ω to different threshold values will still form ligaments and droplets within different break-up regimes (see Wozniak, 2003) and $\omega = 0$ may form droplets from dripping, but these mechanisms are certainly not similar. Different modeling functions may require different approaches for the embedding of various influence variables.

For an ideal case, the experimentally–determined individual exponents of l^*_{Lig} and d^*_p over $\Pi_{i>2}$ are entered in the equations (4.8) and (4.9) and deliver a modeling equation that both represents the underlying physics as well as a good regression for the experimental data.

This the case for the scaled ligament length l^*_{Lig} and the scaled droplet diameter d^*_p for the material M_2 from a measurement series with varied aluminum flake solid content (see figures 4.22 and 4.23). Each data point represents the scaled average value of one measurement series with given process and material parameters. The individual regression values R^2 for the functional dependencies of l^*_{Lig} and d^*_p are drastically lower than the overall regression shown in equations (4.10) and (4.11) for the combined product of power laws (c.f. figure 4.21). These are

$$l^*_{\mathrm{Lig,M_2}} = \left(\frac{\eta_g}{\eta_s}\right)^{-2.03} \cdot \left(\frac{c_{ax}}{\omega \cdot R}\right)^{0.464} \cdot {We_{ax,l}}^{0.206} \cdot {Re_{ax,l}}^{0.217} \cdot {De_{cap}}^{-0.37} \cdot (1+\varphi)^{-51.4}, \quad (4.10)$$

$$d^*_{p,M_2} = \left(\frac{\eta_g}{\eta_s}\right)^{-0.43} \cdot \left(\frac{c_{ax}}{\omega \cdot R}\right)^{0.160} \cdot {We_{ax,l}}^{0.001} \cdot {Re_{ax,l}}^{-0.017} \cdot {De_{cap}}^{-0.13} \cdot (1+\varphi)^{11.0}. \quad (4.11)$$

Even if the ideal case cannot be fully met, the product of power laws can be fitted to the data set, using the experimentally–determined exponents as starting values for a numerical exponent fitting, either by maximizing regression values, or, for example, by applying a log–likelihood estimation (see section 4.4).

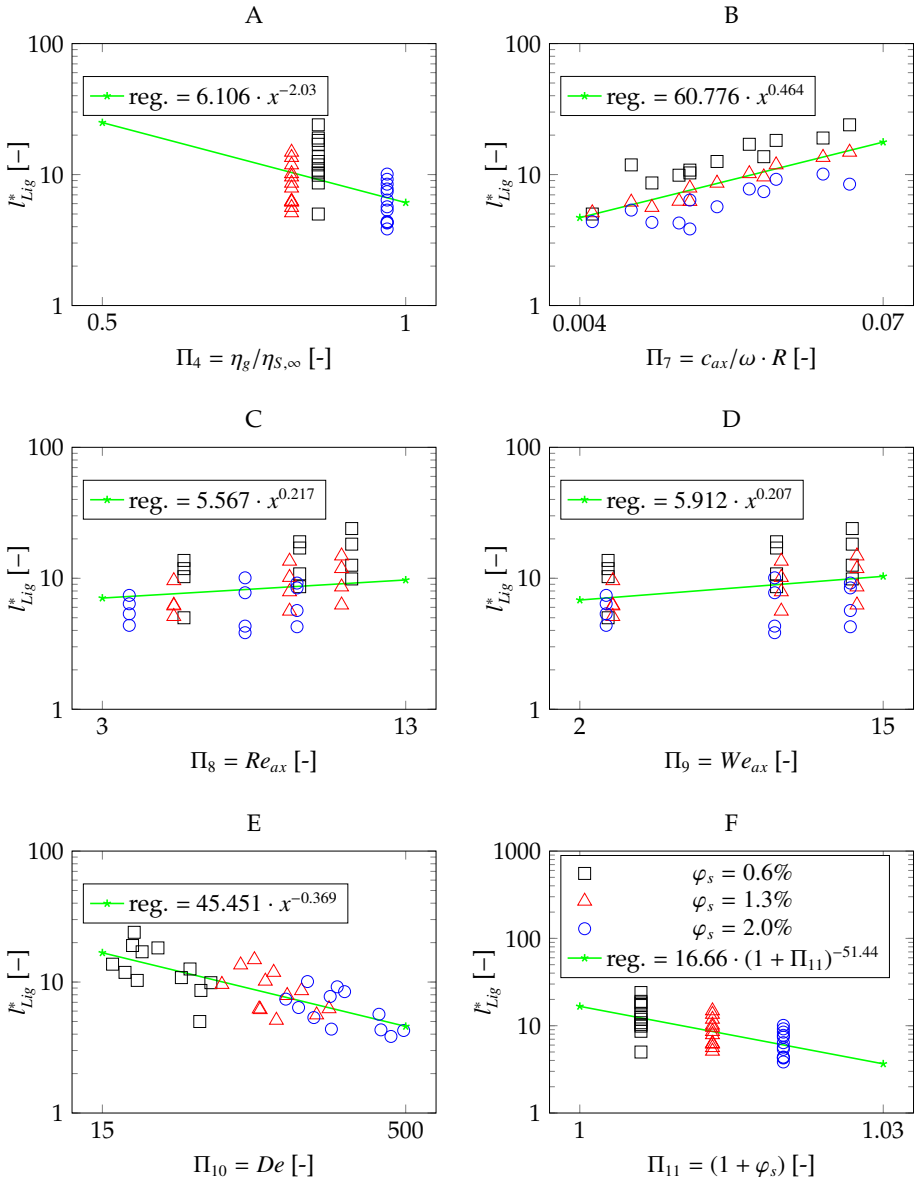

Figure 4.21: l^*_{Lig} over Π_i for M_2 with varying aluminum content φ_s as log-log-diagram, including the resulting exponent of the regression functions. $R^2_A = 0.165$, $R^2_B = 0.494$, $R^2_C = 0.028$, $R^2_D = 0.093$, $R^2_E = 0.578$, $R^2_F = 0.398$.

The obtained modeling equations will deliver a better regression towards the experimental data while conserving the physical dependencies. A fully math–based model, ideally for the entirety of the data, most likely determined by

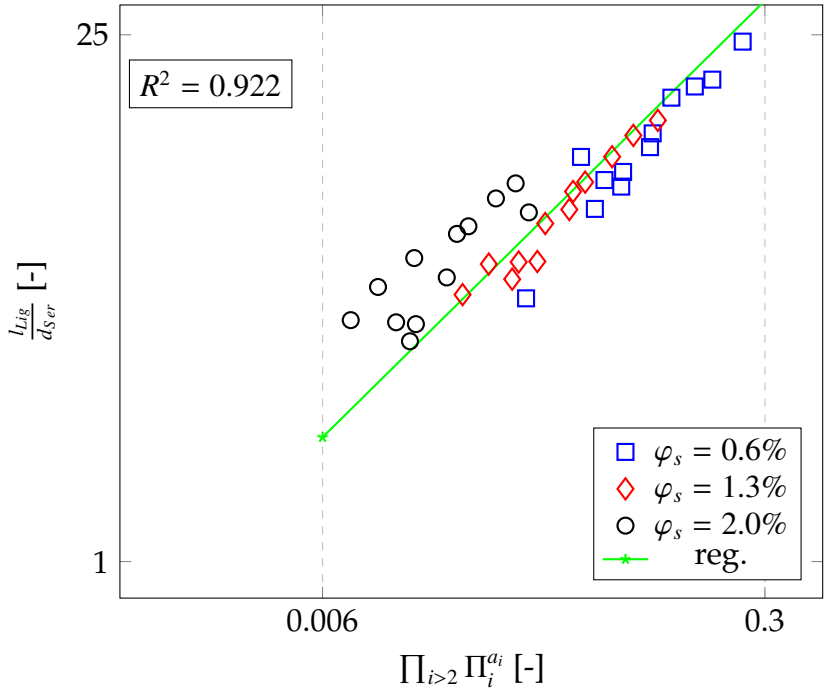

Figure 4.22: l^*_{Lig} over $\prod_{i>2} \Pi_i^{a_i}$ for M_2 with varying aluminum flake content.

automated machine learning, may deliver the best possible regression, while simultaneously eschewing the underlying physics.

Modeling equations for the materials M_1 and M_3 and their corresponding figures can be found in appendix A (see A.1, A.2, A.3, A.4).

Figures 4.24 and 4.25 show the resulting behaviour of the modeling equations (4.12) and (4.13) based on the measured data sets from the variation of different Sterocoll mixtures (see section 3.1.1, table 3.3) with added glass flakes as solid content shown in Goedeke et al., 2021. For both equations the power–law exponents are determined by multi–variant linear regression, thus do not fully represent physical dependencies but rather a global maximum of the mathematical regression. The modeling equations are

$$l^*_{Lig,Stero} = \frac{d_{Ser}}{R} \cdot \frac{\rho_g}{\rho_p} \cdot \frac{\eta_g}{\eta_s} \cdot \left(\frac{c_{ax}}{\omega \cdot R}\right)^{0.036} \cdot We_{ax,l}{}^{0.50} \cdot Re_{ax,l}{}^{-1.00} \cdot De_{cap}{}^{0.014} \cdot (1+\varphi)^{-88.0} \quad (4.12)$$

and

$$d^*_{p,Stero} = \frac{d_{Ser}}{R} \cdot \frac{\rho_g}{\rho_p} \cdot \frac{\eta_g}{\eta_s} \cdot \left(\frac{c_{ax}}{\omega \cdot R}\right)^{0.132} \cdot We_{ax,l}{}^{0.43} \cdot Re_{ax,l}{}^{-0.97} \cdot De_{cap}{}^{0.004} \cdot (1+\varphi)^{3.0} . \quad (4.13)$$

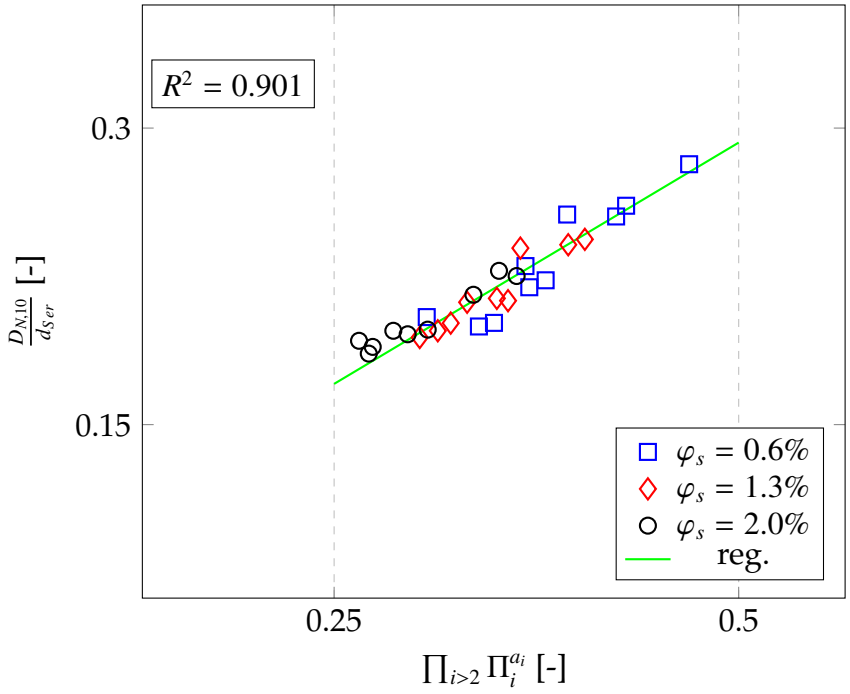

Figure 4.23: $d^*_{p,10}$ over $\prod_{i>2} \Pi_i^{a_i}$ for M_2 with varying aluminum flake content.

Both individual material groups, coatings and Sterocoll mixtures, show that generally similar materials can be successfully modeled using a product of power laws. Delivering a generalized modeling equation for the entirety of the experimentally determined data sets is not possible, as Sterocoll mixtures and different pigmented coatings can be modeled in a comparable way, but are not similar enough to deliver a reliable combined model.

These correlations for different dimensionless ligament lengths l^*_{Lig}, droplet diameters d^*_p and possibly *span*-values can serve as initial value estimators for numerical modeling or to deliver approximations for material development and research via similarity approaches. Developing models for the expected droplet diameters and validating these models by use of different measured data increases the probability of correct prediction models for operational values, such as the different appearance values (see section below).

Coating quality parameters such as surface waviness values (W_{a-d}, BYK-Gardner WaveScan), colour uniformity and flop performance (see Akafuah et al., 2016, Gómez et al., 2016 and Yomo and Tachi, 2021) are measurable and

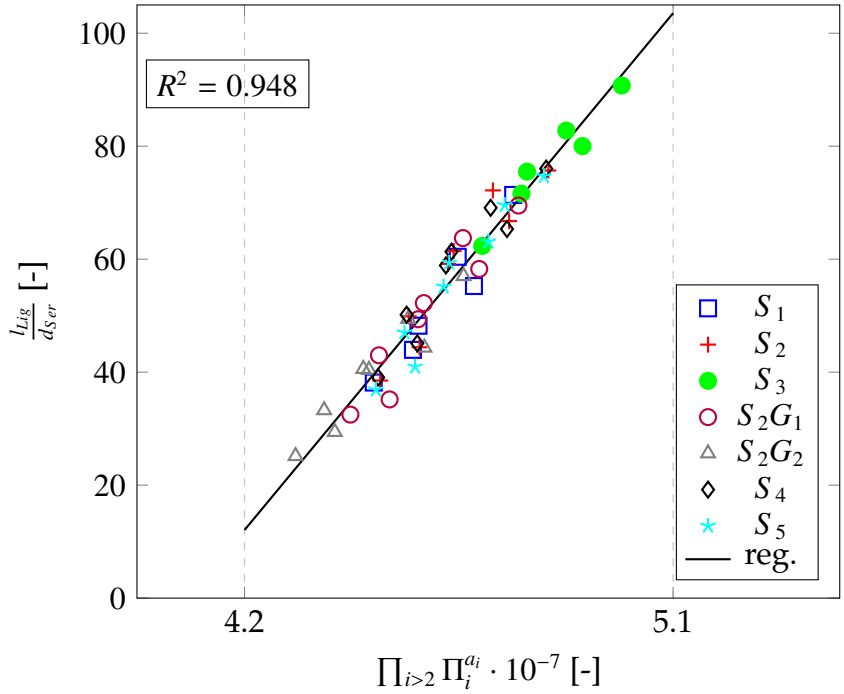

Figure 4.24: l^*_{Lig} over $\prod_{i>2} \Pi_i^{a_i}$ for Sterocoll with and without glass flakes. (Goedeke et al., 2021).

can be evaluated with different statistical methods, in regards to their subjective effects for the final customer. Accordingly, model development does target those values within their ranges and their optimal values. During this project we had mere contact points with different side-projects that analyze surface properties of different applied coating variations. In-depth model development for appearance parameters exceeds the experimental capacities of the project but appears promising, especially when combined with targeted properties development for new coatings and when trying to eliminate weaknesses of existing coating compositions. Ideally, different modeling functions can be derived from fully analyzing surface properties of different applied coatings, after methodically processing these samples depending on the application parameters (wetness, flashing). Existing correlation can be used to answer slight deviations observed during quality control by correction of process parameters *in-situ* to minimize subsequent time-consuming and therefore expensive coating repair.

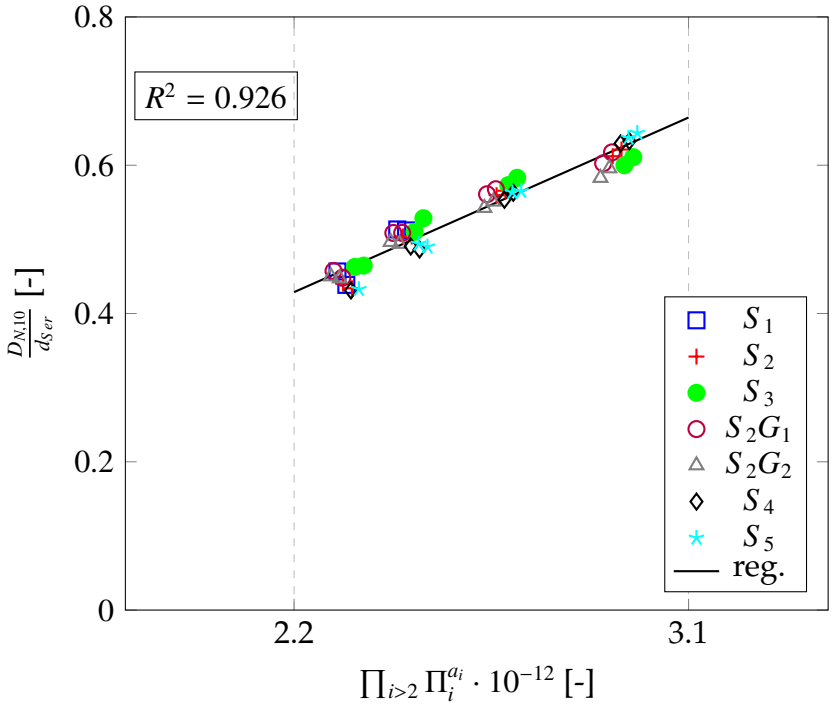

Figure 4.25: $d^*_{p,10}$ over $\prod_{i>2} \Pi_i^{a_i}$ for Sterocoll with and without glass flakes. (Goedeke et al., 2021).

Further expanding the possibilities of modelling approaches can be done by use of purely mathematical correlations that do not necessarily represent physics. The crux of the matter is to find the right modelling approach, even though today's commercial software does support with different multi-variable non-linear fitting tools for characteristic functions. Large data pools are destined to be analyzed using commercial AI-tools. This, however, exceeds the scope of this project and is highly recommended to be analyzed by data scientists and data engineers. The physical influences and the different dependencies discussed earlier enhance the quality of possible results by plausibility proof, as well as reducing the overall computational and modeling effort.

4.7 Error discussion

Although measurements are repeatedly performed with the same instruments, rarely are their values consistent. The occurrence of systematic and random

errors (or variance terms) results in deviations of measured parameters from their theoretical counterpart. The following briefly describes the quantification of the relevant measurement uncertainties. The mean square error of an estimated value is the combination of both of these error terms. Assuming that the sample size is sufficiently large ($N_{count} > 5000$, see section 2.7) the variance term diminishes.

Systematic errors occur due to the instruments used and are consistent in every measurement. LD, PDA and TS, the three different measurement techniques used here, are based on fundamentally different physics in regards to signal generation. At most, the difference between PDA and TS could be contentious. Accordingly, the measurement data obtained are associated with different aspects, that need to be addressed, as a variety of parameters can be obtained from the same particle. For example, with PDA and TS a number distribution is obtained, whereas the LD delivers a volume distribution. These distributions can be transformed into each other under certain conditions (see section 2.6.3). A relative error propagates cubically in the determination of the volume distribution (see Rawle, 2003) and linearly for the number distribution.

The PDA is a calibration-free measuring method. A systematic error for calibration processes can therefore be neglected. For an error-free measurement high accuracy is required for the alignment of the transmitting and receiving optics. The alignment must be planar, both components neither non-tilted nor rotated and in focus. Eventual errors are easily detected in the phase diagram. Depending on the alignment error, different specific shapes can be used to identify and correct the error. The BSA flow software guide (*BSA Flow Software users Guide v6.12* 2014) provides several troubleshooting examples, including the typical phase diagram patterns, and solution approaches. Likewise, detection data rates for a malaligned system are considerably lower than for a good alignment. Individual detection bursts are significantly out of phase or of different amplitude ratios. A unavoidable measurement uncertainty still occurs due to minimal alignment errors. Davis and Disimile refer to a relative measurement error of about 4% for the calculation of diameters by means of PDA measurement (Davis and Disimile, 2004).

Measured phase difference are influenced by various parameters, thus the calculation of d_p is dependant on:

- bias effects, Albrecht et al., 2014, see section 8.3,
- incorrect scattering angle, slight misalignment of components,
- incorrect software parameter settings,
- fluctuations of laser outlet power,
- inhomogeneities in the droplet, $\underline{n} \neq \text{const.}$,
- multi-scattering, high spray density in the measuring volume,
- secondary light refraction/reflection in the spray.

Minor laser power fluctuations lead to invalid droplet detections as the signal amplitudes temporarily diminish and may fall under a system–specific threshold. The assumption of a constant and homogeneous complex refractive index is necessary for the diameter calculation of droplet ensembles as there is no technically–possible method of dynamic determination of individual droplet fluid properties during flight time. Centrifugal effects underneath the bell lead to local density and pigment concentration differences in the film. Hence, the emerging spray is already inhomogeneous in its characteristics, apart from changes of the radial droplet size. During spray propagation towards the substrate, sufficient remixing in the turbulent flow is aimed for but not always possible. Elaborate analysis tools optimize spray patterns to minimize the effect on the overall coating appearance by overlapping the areas covered by the spray.

A problem discovered during the measurement of highly–pigmented or highly reflective (e.g. silver metallic and/or white coatings) is a drastic decrease in data and validation rates for both PDA and TS. The region around the measurement volume is brighter illuminated by reflected light. Repeated reflections from surrounding droplets in the same order of intensity are problematic for the receiver unit, leading to photo multiplier over saturation and distorted bursts. As a result, the number of identifiable detections decreases and data rates plummet in comparison to less reflective coating sprays.

The majority of these measurement uncertainties can be avoided or eliminated by careful initial hardware and software setup and if needed, appropriate adjustments. Errors due to geometric reasons can be assumed to be constant for a set of measurements. Depending on the measurement mode, scattering angle and different post processing steps, the error propagation will change accordingly.

Even with an optimal measurement setup and a hypothetically ideal alignment of the individual components, some possible error sources remain, which need to be addressed, namely

- ligament discharge pulsations, see Oswald et al., 2019a,
- inconsistent liquid volume flow, gear or piston pumps,
- bell speed deviations,
- volume–flow measurement errors,
- pigment segregation and aging of coatings in ring pipes.

HSC image analysis shows pulsations of the filament length (see Oswald et al., 2019a). The mounting socket of the dispenser plate underneath the bell is based upon three vertical struts. These cause a leading and a trailing wave front, propagating in the film underneath the bell towards the bell edge, causing minor ligament flow rate pulsations. Frequency analysis of the HSC images confirms the pulsation dependency on the bell speed. However, the influence on atomization is not measurable, as the construction of the dispenser plate mounting socket could not be varied within the projects scope but is highly advised in a separate study.

Measurement uncertainties for bell speed ω and volumetric flow rate $\dot{V}_l$ measurements are taken into account in regards to the error propagation. Regular calibration measurements in the application booth are performed to verify the accuracy for both parameters, as well as the ambient air parameters temperature, humidity, air pressure and vertical air velocity. The ambient conditions are treated as constant (T = 25°C, φ_{air} = 65%). Uncertainties for bell speed $\Delta\omega$ and volumetric flow rate $\Delta\dot{V}_l$ are listed in table 4.3.

Table 4.3: Relative uncertainties for different material and process parameters.

x_k	$(1+\varphi_s)$	ρ_l	σ	$\eta_{S,\infty}$	ω	$\dot{V}_l$	t_{λ_E}
$\left\lvert\frac{\Delta x_k}{x_k}\right\rvert$	0.01%	0.45 – 0.75%	0.63 – 1.25%	0.25 – 5.00%	1%	1%	4 – 15%

A random error of the PDA and TS measurements can be investigated by repetitive measurements. This is done on different days and with different product batches. According to the industry partner, deviation of material values, such as density and viscosity for the coatings from different batches, is below 1%. Hence, reproducibility can be regarded as very good. A series of measurements performed during the development of the standardized measurement method (subsection 3.5.2) shows that the TS device setup is rather insensitive to minor deviations of the setup (e.g. vertical offset, planar offset, bell tilt angle).

4.7.1 Error propagation

In general, Gaussian error propagation for a product of power laws can be expressed in the following form, as all groups are independent from one another, we obtain

$$\Delta\Pi_j = \sqrt{\sum\left(\frac{\partial\prod_i \Pi_i^{a_i}}{\partial x_k}\Delta x_k\right)^2}. \tag{4.14}$$

Equation (4.12) in the previous section describes the dimensionless ligament length l^* for different Sterocoll mixtures. We assume that the systematic error of the geometric dimensions can be neglected. Applying the Gaussian error propagation (4.14) to equation (4.12) in regards to the individual influence parameters and their specific uncertainties delivers a relative uncertainty for the resulting ligament length, when using the relative uncertainties instead of absolute deviations. Hence, we obtain

$$\begin{aligned}\frac{\Delta l^*_{Lig}}{l^*_{Lig}} = \Bigg[&\left(0.036\frac{\Delta\dot{V}}{\dot{V}}\right)^2 + \left(0.036\frac{\Delta\omega}{\omega}\right)^2 + \left(0.49\frac{\Delta\sigma_{lg}}{\sigma_{lg}}\right)^2 + \ldots \\ &\ldots + \left(0.51\frac{\Delta\rho_l}{\rho_l}\right)^2 + \left(88.0\frac{\Delta(1+\varphi_s)}{(1+\varphi_s)}\right)^2 + \left(0.014\frac{\Delta t_{\lambda_E}}{t_{\lambda_E}}\right)^2\Bigg]^{0.5}.\end{aligned} \tag{4.15}$$

The relative uncertainties are $\frac{\Delta l^*_{Lig}}{l^*_{Lig}} = \pm 1.21\%$ and $\frac{\Delta d^*_{p,10}}{d^*_{p,10}} = \pm 0.79\%$. The maximum deviations are 12.1% and 7.5%, respectively.

The resulting relative errors for the correlations given in section 4.6 can be found in the appendix A, table A.1.

4.8 Conclusion for the applicability of LD, TS and PDA for opaque paint sprays

Particle number and volume size distributions are highly dependent on the measuring method, whether it is done with a conventional PDA, TS or a LD device. To fully utilize the obtained knowledge, it is inevitable to provide encompassing and detailed information about the geometric measurement setup, technical details regarding hard- and software configuration and post-processing specifications for data-refinement. Simply by choosing different mask apertures or sphericity tolerances, we can shift the resulting particle size spectrum significantly, by truncating or over-representing different fractions of the spray. This can be problematic when working with provided data sets under the assumption that everything is covered.

As shown before, it is possible to measure a wide variety of different paint types with different fluid properties as well as different categories of added pigments. Depending on the shape, transparency and colour of the pigments, the detectability is influenced directly by the reflective and refractive light scattering characteristics.

It is recommended to plausibility check the obtained results for unfamiliar fluids either by usage of a different droplet size measurement device or by analyzing a test substrate for deposited droplets. Either way, the data rates must be sufficient and appropriate for the density of the spray. Typically a visual impression, even if subjective, shows a coarse or fine (dense) spray.

4.9 Summary

The initial target of the collaboration project between the BASF Coatings GmbH, the KIT Institute of Mechanical Process Engineering and Mechanics, Applied Mechanics Engineering (KIT/AME) and the TU Dortmund BCI Fluid Mechanics (BCI/SM) was to correlate process parameters, material properties and coating quality to one another. The results were to be refined for different modeling and prediction approaches to facilitate material development as well as fundamental research regarding the atomization of viscoelastic particle-laden fluids and their influence on coating appearance values and error sources.

Walter Oswald and Norbert Willenbacher (KIT/AME) investigated the rheological characterization of the coatings and the used model liquids in a parallel project with extensive exchange and research overlap between the involved partners. Accordingly, we (BCI/SM) were responsible for the measurement of in–flight droplet properties, such as droplet diameters and velocites, as well as the data refinement and subsequent model development. The BASF Coatings GmbH, most notably Georg Wigger, Dirk Eierhoff and Daniel Briesenick provided full support in Münster Hiltrup for accessing the automated robotic application center (RACe), for the individual composition of multiple test liquids for the application and, additionally, the procurement of the SpraySpy® measurement device. Initial measurements at the TU Dortmund (Witt, 2017 and Illner, 2017) highlighted different aspects that later showed to be difficult to solve during the coating application process in the RACe, e.g. spray cone–substrate interactions and measurability of different test liquids. Due to limited time schedules at the commercial facility, measurements were planned at a minimum to reduce needed material quantities while providing a full experimental data set, covering a wide variety of process parameters and material properties. All liquids used were either provided by the BASF coatings and fabricated at lab standard with known properties or pre–produced by W. Oswald in case of the different Sterocoll mixtures.

This work provides an introduction into the fundamentals of modern coating technologies while highlighting the individually important aspects for the studied cases, including error sources, general challenges during the applica-

tion process and possible solutions to these problems (ch. 1). The theoretical background is provided by various sources of information for further research.

Following the general definition of the process (section 2.1.1) and the basic description for shear thinning liquid rheology (section 2.2) an approach for the estimation of the shear and strain rates is presented. This estimation process is necessary, as conventional methods are not applicable within the scope of this work due to immense technical limitations during the bell–atomization process. A dimensional analysis is presented to define a set of dimensionless groups used for data presentation and modeling approaches that are based upon physical relations between the individual independent parameters (see section 2.4, Goedeke et al., 2021). The three parameter Burr Type XII function is presented to describe the measured droplet distributions and their moments to reduce large quantities of droplet data to a set of function variables. Subsequently, aspects of area averaging and the determination of the statistically necessary minimum droplet number are presented.

Ligament break-up and droplet impact phenomena are shortly discussed. The modeling of coating ligament break-up processes appears possible. Controlled bubble entrapment during droplet impact can be reproduced on a larger scale with simple experimental setups (Burzinski, 2018 and Grünendahl, 2017), whereas the occasional occurrence of entrapped bubbles during spray application is not fully resolved by now.

Chapter 2 of this work is concluded with a short presentation of the different measurement devices PDA, TS and LD and the specifics for the measurement of opaque fluid droplets. All,the LDA, the PDA the TS and the LD are commercially available devices with, in case of the LDA/PDA, a long history in non–invasive velocity and size measurement. The TS device provided by the industrial partner still underwent consecutive software and hardware development during the cooperation project. Thorough exchange with Walter Schäfer and Simon Rosenkranz from AOM Systems in Griesheim, Germany, enabled the necessary steps for the adaption of the SpraySpy® device as a plug–and–play solution for droplet size measurements.

Extensive preemptive measurement campaigns for both devices (PDA and TS), as well as multiple trials with the high-speed camera (HSC) system are con-

densed in chapter 3, *Experimental Setup*. Following the definition of ranges for the used liquid material properties and process parameters the exact setup for both size measurement devices PDA and TS, HSC and needed software configurations are established. Section 3.5 describes the development of a standardized measurement method that is used with both PDA and TS. This method leads to an accelerated measurement program and reduced material needs while simultaneously providing more flexible data that can be further evaluated using post-processing software or algorithms. The successful implementation of this method lead to U.S. Patent 20210262911 (see Wigger et al., 2021). Both, PDA and TS are able to mutually confirm each others result by use of this measurement method for a given spray.

Chapter 4 begins with the results from LDA measurements presenting an accurate, yet generally only qualitatively correct picture of the flow field underneath the bell. The measurements show the well–known vortex structure in proximity to the bell and a decline in absolute velocity values and a widening of the spray cone with increasing distance from the bell. This flow field will differ for each set of process parameters and fluid properties, resulting in a more narrow or wider spray cone, more so with a substrate as target surface. The combination with locally–averaged droplet sizes shows that for typical application distances (e.g. larger than 200 mm, due to electrostatic charging), a good homogeneous average droplet size and velocity distribution is achieved, diminishing the influence of individual droplet velocities for averaged droplet size values during deposition on the substrate. A clear dependency between droplet size and velocity cannot be confirmed, however, we suspect single large droplets with a high velocity to be relevant to occurring error patterns.

Based upon experimental HSC images of the filament lengths at the bell edge a validation of the aforementioned strain rate can be performed. Results are in good agreement with the theoretical values achieved in Kuhnhenn et al., 2018.

The obtained data are evaluated and refined using a self-written MATLAB code (see addendum). The functionality and general process patterns of this algorithm are explained in section 4.4. Conventional processing software provided by Dantec as well as AOM Systems works as intended, however, for research purpose we do need greater flexibility to analyze raw data and to dif-

fer between validated and non-validated values if possible. For the PDA the validation processes are well known and can be reproduced externally. As of now, this is not possible for the SpraySpy® due to internal storage limitations. A thorough investigation of the relevant hard- and software parameters on the PDA setup is performed and evaluated. The results obtained during the PDA measurement of different liquid-solid mixtures with different added pigments show no clear dependency of atomization properties and measurability on the type of pigment added. Depending on the setup minor deviations of measured sizes and data rates can be observed. As described in U.S. Patent 20210262911 (Wigger et al., 2021) a differentiation of a transparent (T) and a non-transparent (NT) fraction is possible by using the SpraySpy® device. The sum of both individual measurements (T and NT measurement) delivers the both opacity fractions of the spray, resulting in a cumulative distribution, comparable to the distribution obtained by PDA measurement. This shows that separation effects inside the spray can be relevant depending on the remixing characteristics of the flow. Insufficient remixing will lead to inhomogeneities in the final film on the substrate. The tendency to T/NT separation is dependant on liquid–solid interactions (wetting, clustering) in the paint dispersion, as described in the U.S. Patent 20210262911 (Wigger et al., 2021). Locally different average size distributions, velocity values, data rates and T/NT–ratios are plausible and reproducible for all sprays when abiding to the standardized method, resulting in a full capturing of the entire spray.

The experimentally–obtained ligament lengths and droplet sizes can be used to define modeling functions for the scaled target values. Ideally, the exponents of the product–of–power–law functions can be determined by a double–logarithmic plot of the the droplet size or ligament lengths values against the individual dimensionless groups defined in section 2.4. This delivers good regression values for the Material M_2. Subsequent modeling of these exponents does increase the R^2-values. However, the representation of the underlying physical effects decreases with the increase of purely mathematical modeling. The modeling approach can be verified using different Sterocoll mixtures. However, universal modeling function for the entirety of the obtained data can not be obtained within acceptable R^2-values. This suggests that eventually some assumptions and simplifications made during the dimensional analysis

and the modeling approaches are only accurate for different subsets of the used liquid–solid combinations.

A thorough error discussion highlights different influences that distort the quality of obtained data sets. The general approach for the characterization of the spray does not account for variable material properties, changing from droplet to droplet directly at the ligament breakup and during flight time. An ideal experimental setup minimizes the influence of external parameters, as both PDA and TS are rather robust when set up correctly. However, flow fluctuations, process parameter uncertainties and segregation effects can not by fully avoided. The uncertainties for measured values can be evaluated by use of Gaussian error propagation.

The conclusion for the measurement of opaque liquids with PDA and TS is, that both devices are capable, within their technical limitations, to fully determine the characteristics of a developed spray cone. Different influencing parameters lead partially to drastic changes of the obtained values, often highly biased in one direction of the size distribution. It is therefore inevitable to provide the full set of parameters for the geometrical configuration of the device used as well as the setting used in the evaluation software.

Whenever possible, it is advised to use a standardized method of traversing measurement for rotary bell atomizers.

Bibliography

(1) Adams, A. J.; Chappie, A. C.; Hall, F. R. In *Pesticide Formulations and Application Systems: 10th Volume*; ASTM International: 1990.

(2) Akafuah, N. K.; Poozesh, S.; Salaimeh, A.; Patrick, G.; Lawler, K.; Saito, K. Evolution of the Automotive Body Coating Process—A Review. *Coatings* **2016**, *6*.

(3) Albrecht, H. E.; Damaschke, N.; Borys, M.; Tropea, C., *Laser Doppler and Phase Doppler Measurement Techniques*; Experimental Fluid Mechanics; Springer Berlin Heidelberg: 2014.

(4) Baehr, H. D.; Kabelac, S., *Thermodynamik: Grundlagen und technische Anwendungen*; Springer Berlin Heidelberg: 2012; Chapter 4.

(5) BASF SE High-tech no thicker than a human hair, https://www.basf-coatings.com/global/en/products-and-solutions/automotive_oem_coatings/exterior_solutions.html, accessed: 2021-12-15, 2021.

(6) Bothe, M. Theoretische Betrachtung des laminaren Strahlzerfalls am Rotationszerstäuber, Masters's Thesis, TU Dortmund, 2018.

(7) *BSA Flow Software users Guide v6.12*; Dantec Dynamics A/S: 2014.

(8) Buckingham, E. On Physically Similar Systems; Illustrations of the Use of Dimensional Equations. *Physical Reviews* **1914**, *4*, 345–376.

(9) Burr, I. W. Cumulative Frequency Functions. *Annals of Mathematical Statistics* **1942**, *13*, 215–232.

(10) Burzinski, F. Experimentelle Untersuchung des dynamischen Prozesses zum Blaseneinschluss durch Tropfenaufprall auf festen Oberflächen, Bachelor's Thesis, TU Dortmund, 2018.

(11) Davis, J. M.; Disimile, P. J. In *14th Halon Options Technical Working Conference*, 2004.

(12) Decent, S. P.; King, A. C.; Simmons, M. J. H.; Părău, E. I.; Wallwork, I. M.; Gurney, C. J.; Uddin, J. The trajectory and stability of a spiralling liquid jet: Viscous theory. *Applied Mathematical Modelling* **2009**, *33*, 4283–4302.

(13) Dodge, L. G.; Rhodes, D. J.; Reitz, R. D. Drop-size measurement techniques for sprays: comparison of Malvern laser-diffraction and Aerometrics phase/Doppler. *Applied Optics* **1987**, *26*, 2144–2154.

(14) Domnick, J.; Scheibe, A.; Ye, Q. The Simulation of the Electrostatic Spray Painting Process with High-Speed Rotary Bell Atomizers. Part I: Direct Charging. *Particle & Particle Systems Characterization* **2005**, *22*, 141–150.

(15) Dunning, T.; Ertl, O. Computing extremely accurate quantiles using t-digests. *arXiv:1902.04023* **2019**.

(16) Freedman, D.; Diaconis, P., *On the Histogram as a Density Estimator: L 2 Theory*, 1981.

(17) Glasurit Lackschadenratgeber, https://www.glasurit.com/de-de/lackschaedenratgeber/, accessed: 2021-12-15, 2021.

(18) Goedeke, L.; Oswald, W.; Willenbacher, N.; Ehrhard, P. Dimensional analysis of droplet size and ligament length during high-speed rotary bell atomization. *Journal of Coatings Technology and Research* **2021**, *18*, 75–81.

(19) Gómez, O.; Perales, E.; Chorro, E.; Burgos, F. J.; Viqueira, V.; Vilaseca, M.; Martínez-Verdú, F. M.; Pujol, J. Visual and instrumental assessments of color differences in automotive coatings. *Color Research & Application* **2016**, *41*, 384–391.

(20) Gooch, J. W., *Power law (Ostwald-deWaele model)*; Springer New York: 2007, p 781.

(21) Gramlich, S.; Piesche, M. Numerical and experimental investigations on the breakup of particle laden liquid jets in the centrifugal field. *Chemical Engineering Science* **2012**, *84*, 408–416.

(22) Grünendahl, S. Experimentelle Untersuchung zum Blaseneinschluss durch Tropfenaufprall auf festen Oberflächen. Masters's Thesis, TU Dortmund, 2017.

(23) Haenlein, A., *Über den Zerfall eines Flüssigkeitsstrahles*; VDI-Verlag: 1931.

(24) Hawkins, V. L.; Gurney, C. J.; Decent, S. P.; Simmons, M. J. H.; Uddin, J. Unstable waves on a curved non-Newtonian liquid jet. *Journal of Physics A: Mathematical and Theoretical* **2010**, *43*, 055501.

(25) Hecht, E., *Optics*; Pearson: 2003.

(26) Hedderich, J.; Sachs, L., *Angewandte Statistik: Methodensammlung mit R*; Springer Berlin Heidelberg: 2016.

(27) Illner, M. Experimentelle Untersuchung der Zerstäubung von wasserbasierten Lacken/nicht-Newtonischen Flüssigkeiten am Hochrotationszerstäuber, Masters's Thesis, TU Dortmund, 2017.

(28) Kalmbach, T.; Gramlich, S.; Piesche, M., *Movement and Hydrodynamic Instabilities of Particle-Laden Liquid Jets in the Centrifugal Field Influenced by a Gas Flow*; Fritsching, U., Ed.; Process-Spray: Functional Particles Produced in Spray Processes; Springer International Publishing: 2016, pp 171–204.

(29) Kuhnhenn, M.; Joensen, T. V.; Reck, M.; Roisman, I. V.; Tropea, C. Study of the internal flow in a rotary atomizer and its influence on the properties of the resulting spray. *International Journal of Multiphase Flow* **2018**, *100*, 30–40.

(30) Langford, E. Quartiles in Elementary Statistics. *Journal of Statistics Education* **2006**, *14*.

(31) Lefebvre, A. H.; McDonell, V. G., *Atomization and sprays*; CRC press: 2017.

(32) Macosko, C. W., *Rheology: Principles, measurements, and applications.* Wiley-VCH: 1994.

(33) Mansour, A.; Chigier, N. Air-blast atomization of non-Newtonian liquids. *Journal of Non-Newtonian Fluid Mechanics* **1995**, *58*, 161–194.

(34) Mescher, A. Einfluss der Gasführung in Sprühtrocknern auf den Fadenzerfall an Rotationszerstäubern, Ph.D. Thesis, TU Dortmund, 2012.

(35) Onofri, F.; Girasole, T.; Gréhan, G.; Gouesbet, G.; Brenn, G.; Domnick, J.; Xu, T.-H.; Tropea, C. Phase-Doppler Anemometry with the Dual Burst Technique for measurement of refractive index and absorption coefficient simultaneously with size and velocity. *Particle & Particle Systems Characterization* **1996**, *13*, 112–124.

(36) Oswald, W. Experimental study on high-speed rotary bell atomization of viscoelastic suspensions, Ph.D. Thesis, KIT, 2021.

(37) Oswald, W.; Goedeke, L.; Ehrhard, P.; Willenbacher, N. Influence of the elongational flow resistance and pigmentation of coating fluids on high-speed rotary bell atomization. *Atomization and Sprays* **2020**, *29*.

(38) Oswald, W.; Lauk, J.; Goedeke, L.; Ehrhard, P.; Willenbacher, N. Analysis of Paint Flow Pulsations during High-Speed Rotary Bell Atomization. *Coatings* **2019**, *9*, 674.

(39) Oswald, W.; Recktenwald, S.; Willenbacher, N. What controls filament thinning in uniaxial extension? *Korea-Australia Rheology Journal* **2019**, *31*, 195–201.

(40) Oswald, W.; Willenbacher, N. Controlling the elongational flow behavior of complex shear-thinning fluids without affecting shear viscosity. *Rheologica Acta* **2019**, *58*.

(41) Oswald, W., *personal communication*, 2020.

(42) Panckow, R.; Maaß, S.; Emmerich, J.; Kraume, M. Automatisierte Quantifizierung von Blasengrößenverteilungen in einem gerührten Luft/Wasser-System. *Chemie Ingenieur Technik* **2013**, *85*, 1036–1045.

(43) Rawle, A. F. Basic of principles of particle-size analysis. *Surface coatings international. Part A, Coatings Journal* **2003**, *86*, 58–65.

(44) Ray, R. Evaporation of Spray from a Rotary Bell Atomizer, Ph.D. Thesis, University of Windsor, 2015.

(45) Saei, S.; Mohammadi, M.; Fekriseri, M.; Jenab, K. A computational method for estimating Burr XII parameters with complete and multiple censored data. *arXiv:1901.09299* **2019**.

(46) Saranjam, N.; Chandra, S. Bubble Clustering in Drying Paint Films. *Industrial & Engineering Chemistry Research* **2016**, *55*, 12825–12835.

(47) Saranjam, N.; Chandra, S.; Mostaghimi, J.; Fan, H.; Simmer, J. Orange peel formation due to surface tension-driven flows within drying paint films. *Journal of Coatings Technology and Research* **2016**, *13*, 413–426.

(48) Schaefer, W.; Tropea, C.; Wigger, G.; Eierhoff, D. Spray measurements with the time-shift technique. *Measurement Science and Technology* **2021**, *32*, 105202.

(49) Schäfer, W.; Rosenkranz, S.; Tropea, C. In *ILASS Americas 27th annual conference on liquid atomization and spray systems*, 2015.

(50) Scholz, T., *Experimentelle Untersuchungen zur Mehrphasenströmung im Sprühkegel eines elektrostatisch unterstützten Hochrotationszerstäubers*; Fortschritt-Berichte VDI. Reihe 7, Strömungstechnik; VDI-Verlag: 1998.

(51) Siekmann, H. E., *Strömungslehre: Grundlagen*; Springer Berlin Heidelberg: 2000; Chapter 5.

(52) Spurk, J. H., *Dimensionsanalyse in der Strömungslehre*; Springer Berlin Heidelberg: 1992; Chapter 3.

(53) Stelter, M.; Brenn, G.; Yarin, A. L.; Singh, R. P.; Durst, F. Validation and application of a novel elongational device for polymer solutions. *Journal of Rheology* **2000**, *44*, 595–616.

(54) Stieß, M. In *Mechanische Verfahrenstechnik-Partikeltechnologie 1*; Springer: 2009, pp 161–260.

(55) Streitberger, H.; Goldschmidt, A., *BASF Handbook Basics of Coating Technology: 3rd Revised Edition*; European Coatings Library; Vincentz Network: 2018.

(56) Tadikamalla, P. R. A Look at the Burr and Related Distributions. *International Statistical Review* **1980**, *48*, 337–344.

(57) Thoroddsen, S. T.; Etoh, T. G.; Takehara, K.; Ootsuka, N.; Hatsuki, Y. The air bubble entrapped under a drop impacting on a solid surface. *Journal of Fluid Mechanics* **2005**, *545*, 203–212.

(58) Tratnig, A.; Brenn, G.; Strixner, T.; Fankhauser, P.; Laubacher, N.; Stranzinger, N. Characterization of spray formation from emulsions by pressure-swirl atomizers for spray drying. *Journal of Food Engineering* **2009**, *95*, 126–134.

(59) Utan, Y. Experimentelle Untersuchung optisch inhomogener Festkörperpartikel verschiedener Formfaktoren mittels Phasen-Doppler-Anemometrie (PDA), Masters's Thesis, TU Dortmund, 2019.

(60) Vetter, F. Impact of pigment morphology and binder concepts on filament formation and atomization in car coating systems (confidential BASF), Masters's Thesis, Hochschule Bremerhaven, 2018.

(61) Wallwork, I. M.; Decent, S. P.; King, A. C.; Schulkes, R. M. S. M. The trajectory and stability of a spiralling liquid jet. Part 1. Inviscid theory. *Journal of Fluid Mechanics* **2002**, *459*, 43–65.

(62) Weber, C. Zum Zerfall eines Flüssigkeitsstrahles. *ZAMM - Journal of Applied Mathematics and Mechanics* **1931**, *11*, 136–154.

(63) Weckerle, G. Beschichtung hochwertiger Karosserieoberflächen mit Pulver-Slurry, Ph.D. Thesis, Universität Stuttgart, 2003.

(64) Wigger, G.; Briesenick, D., *personal communication in Münster Hiltrup*, 2017.

(65) Wigger, G.; Briesenick, D.; Eierhoff, D.; Bornemann, C.; Riediger, S.; Goedeke, L.; Ehrhard, P. Method for determining the droplet size distribution during atomization and screening method based theron on paint development, U.S. Patent 20210262911, 2021.

(66) Wingo, D. R. Maximum Likelihood Methods for Fitting the Burr Type XII Distribution to Life Test Data. *Biometrical Journal* **1983**, *25*, 77–84.

(67) Wingo, D. R. Maximum likelihood methods for fitting the Burr Type XII distribution to multiply (progressively) censored life test data. *Metrika* **1993**, *40*, 203–210.

(68) Witt, L. Experimentelle Untersuchung von Sprühstrahlen mittels LDA/PDA und Time-Shift-Verfahren, Masters's Thesis, TU Dortmund, 2017.

(69) Wozniak, G., *Zerstäubungstechnik: Prinzipien, Verfahren, Geräte*; Springer Berlin Heidelberg: 2003; Chapter 5.3.

(70) Yomo, S.; Tachi, K. Improving the Appearance of a 3-Coat-1-Bake Coating Film by Minimizing the Shrinkage Difference between the Three Layers. *Coatings* **2021**, *11*.

Appendix A

Addendum

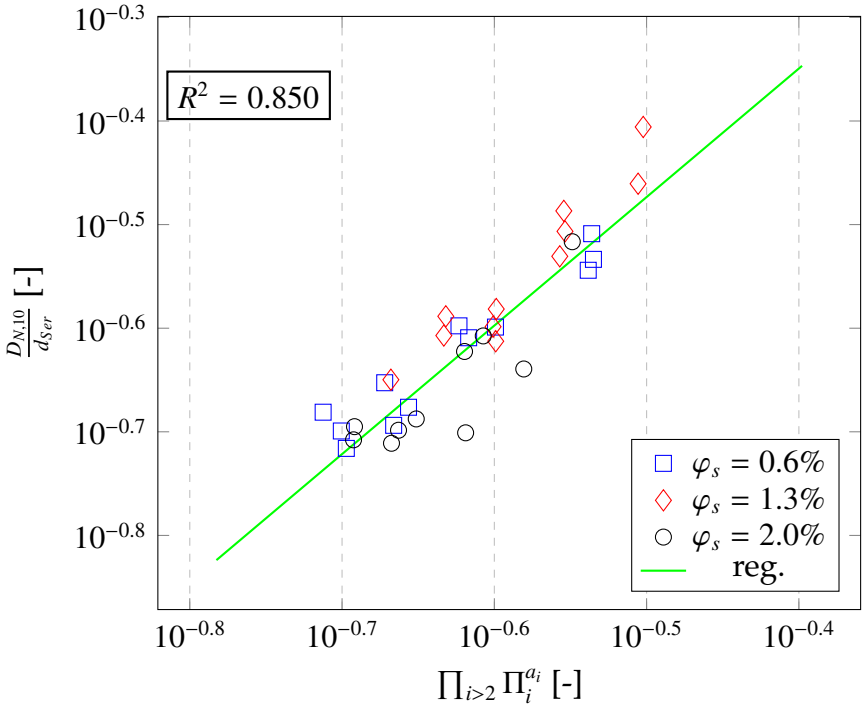

Figure A.1: $d^*_{p,10}$ over $\prod_{i>2} \Pi_i^{a_i}$ for M_1 with varying aluminum flake content.

$$l^*_{\mathrm{Lig,M_1}} = \left(\frac{\eta_g}{\eta_s}\right)^{-0.65} \cdot \left(\frac{c_{ax}}{\omega \cdot R}\right)^{0.461} \cdot We_{ax,l}{}^{0.34} \cdot Re_{ax,l}{}^{0.697} \cdot De_{cap}{}^{-0.58} \cdot (1+\varphi)^{-89.3}, \quad \text{(A.1)}$$

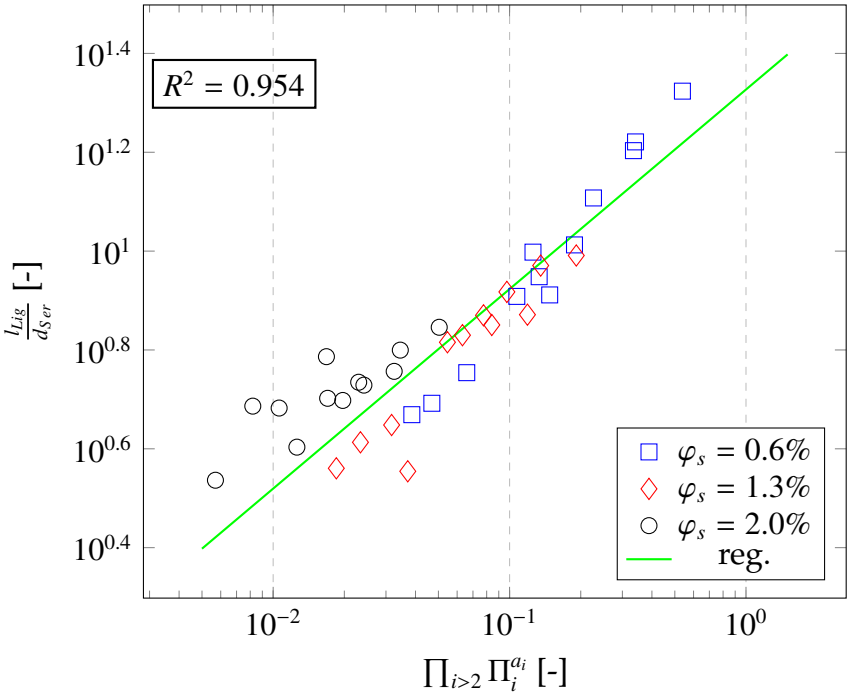

Figure A.2: l^*_{Lig} over $\prod_{i>2} \Pi_i^{a_i}$ for M_1 with varying aluminum flake content.

$$d^*_{p,M_1} = \left(\frac{\eta_g}{\eta_s}\right)^{-0.85} \cdot \left(\frac{c_{ax}}{\omega \cdot R}\right)^{0.160} \cdot We_{ax,l}{}^{0.003} \cdot Re_{ax,l}{}^{-0.150} \cdot De_{cap}{}^{-0.16} \cdot (1+\varphi)^{8.0}, \quad \text{(A.2)}$$

$$l^*_{\mathrm{Lig,M_3}} = \left(\frac{\eta_g}{\eta_s}\right)^{3.28} \cdot \left(\frac{c_{ax}}{\omega \cdot R}\right)^{0.307} \cdot We_{ax,l}{}^{0.206} \cdot Re_{ax,l}{}^{0.217} \cdot De_{cap}{}^{-0.38} \cdot (1+\varphi)^{-20.0}, \quad \text{(A.3)}$$

$$d^*_{p,M_3} = \left(\frac{\eta_g}{\eta_s}\right)^{-4.80} \cdot \left(\frac{c_{ax}}{\omega \cdot R}\right)^{0.254} \cdot We_{ax,l}{}^{0.011} \cdot Re_{ax,l}{}^{-0.440} \cdot De_{cap}{}^{0.19} \cdot (1+\varphi)^{12.0}. \quad \text{(A.4)}$$

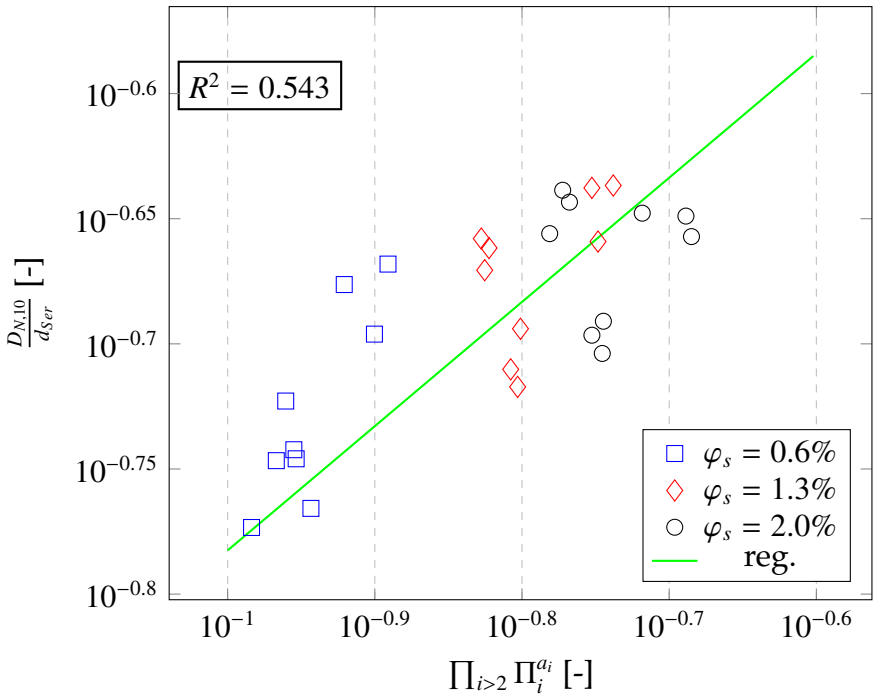

Figure A.3: $d^*_{p,10}$ over $\prod_{i>2} \Pi_i^{a_i}$ for M_3 with varying aluminum flake content.

Table A.1: Relative propagated errors for the different modeling functions.

[%]	M_1	M_2	M_3	$Stero$
$\frac{\Delta l^*_{Lig}}{l^*_{Lig}}$	±6.34	±4.38	±5.31	±1.21
$\frac{\Delta d^*_{p,10}}{d^*_{p,10}}$	±1.69	±1.40	±5.61	±0.79

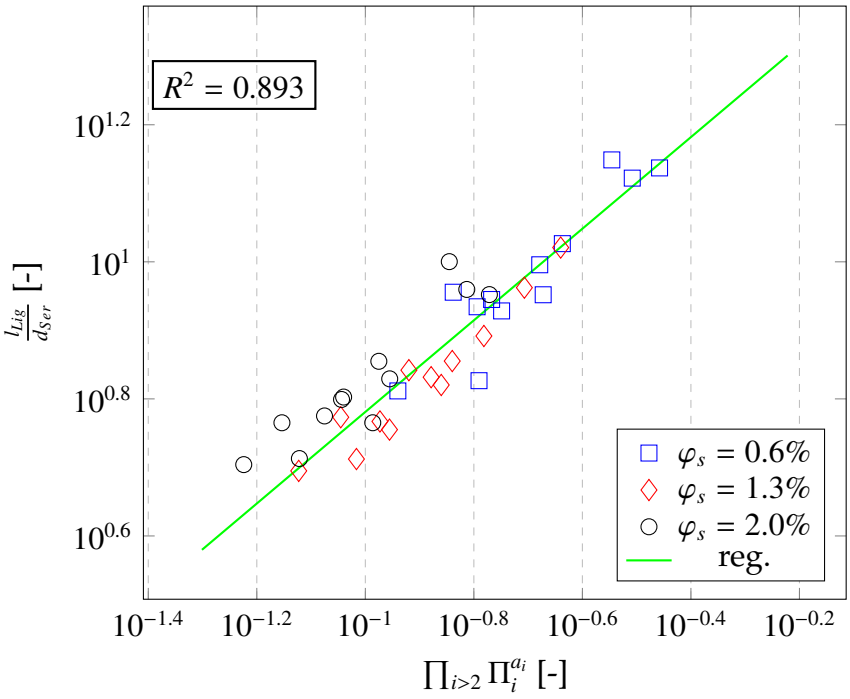

Figure A.4: l^*_{Lig} over $\prod_{i>2} \Pi_i^{a_i}$ for M_3 with varying aluminum flake content.

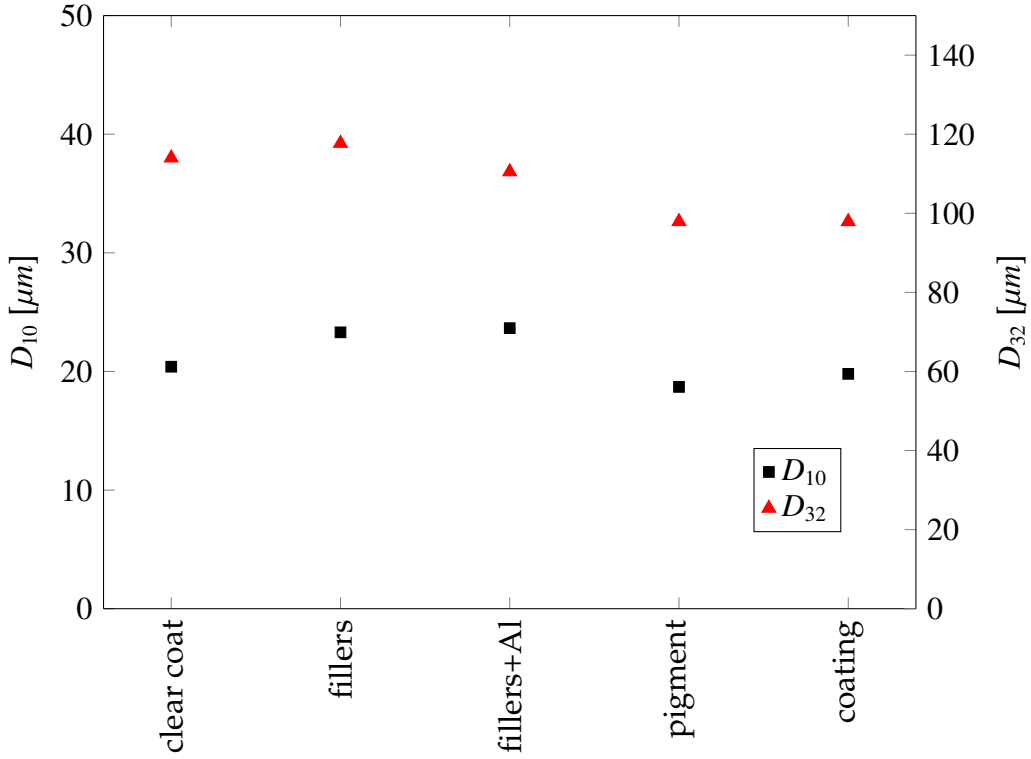

Figure A.5: Variation of pigmentations from clear coat, clear coat with different additives to the complete paint.

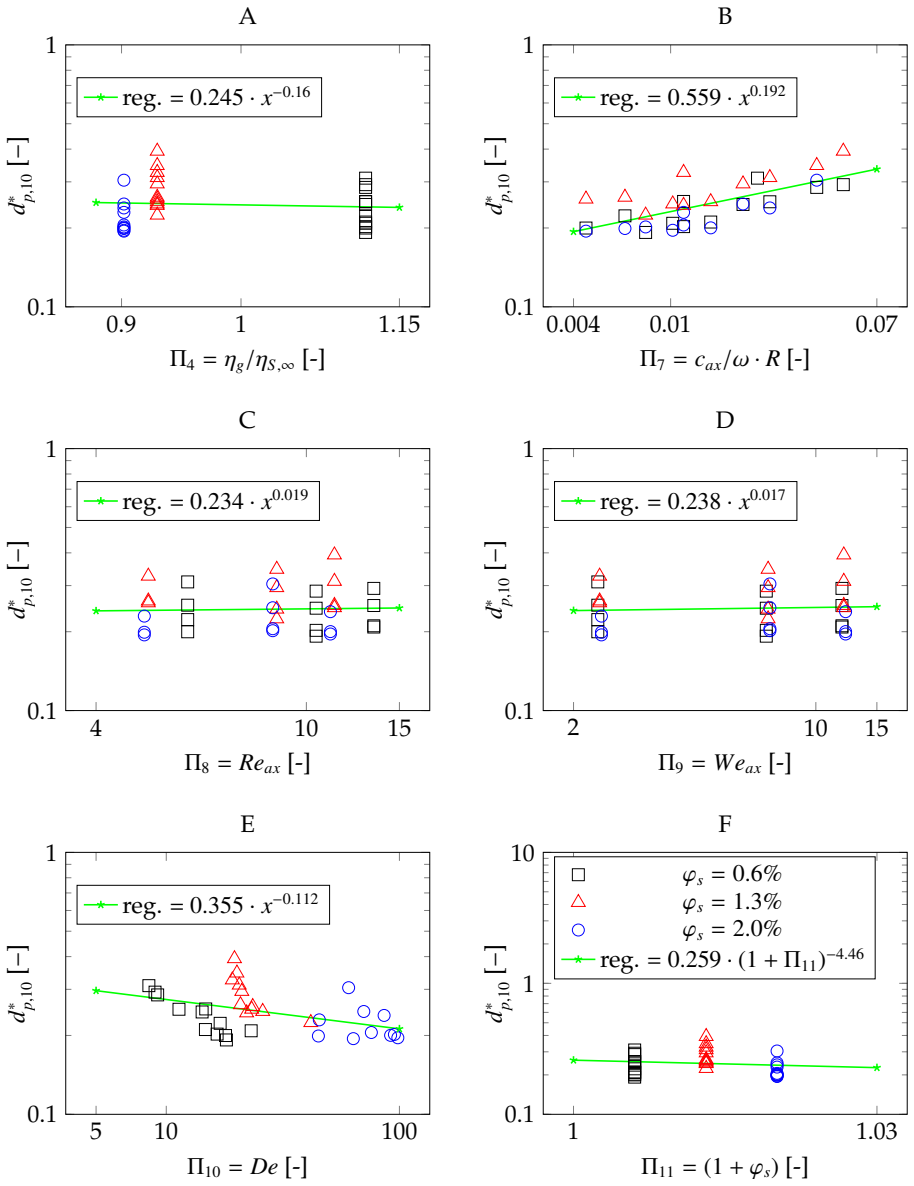

Figure A.6: $d^*_{p,10}$ over Π_i for M_1 with varying aluminum content φ_s as log-log-diagram, including the resulting exponent of the regression functions. $R^2_A = 0.010$, $R^2_B = 0.556$, $R^2_C = 0.001$, $R^2_D = 0.005$, $R^2_E = 0.169$, $R^2_F = 0.014$.

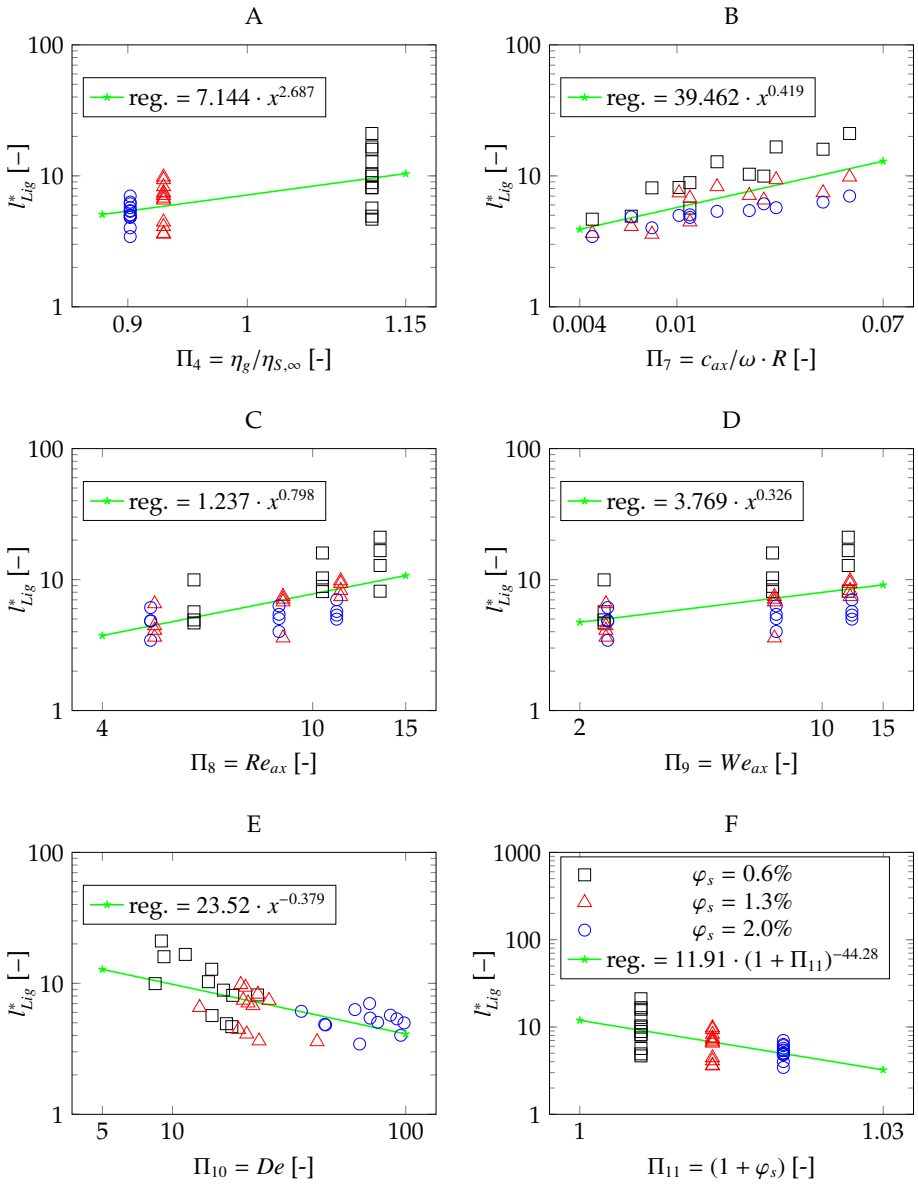

Figure A.7: l^*_{Lig} over Π_i for M_1 with varying aluminum content φ_s as log-log-diagram, including the resulting exponent of the regression functions. $R^2_A = 0.344$, $R^2_B = 0.348$, $R^2_C = 0.399$, $R^2_D = 0.209$, $R^2_E = 0.231$, $R^2_F = 0.319$.

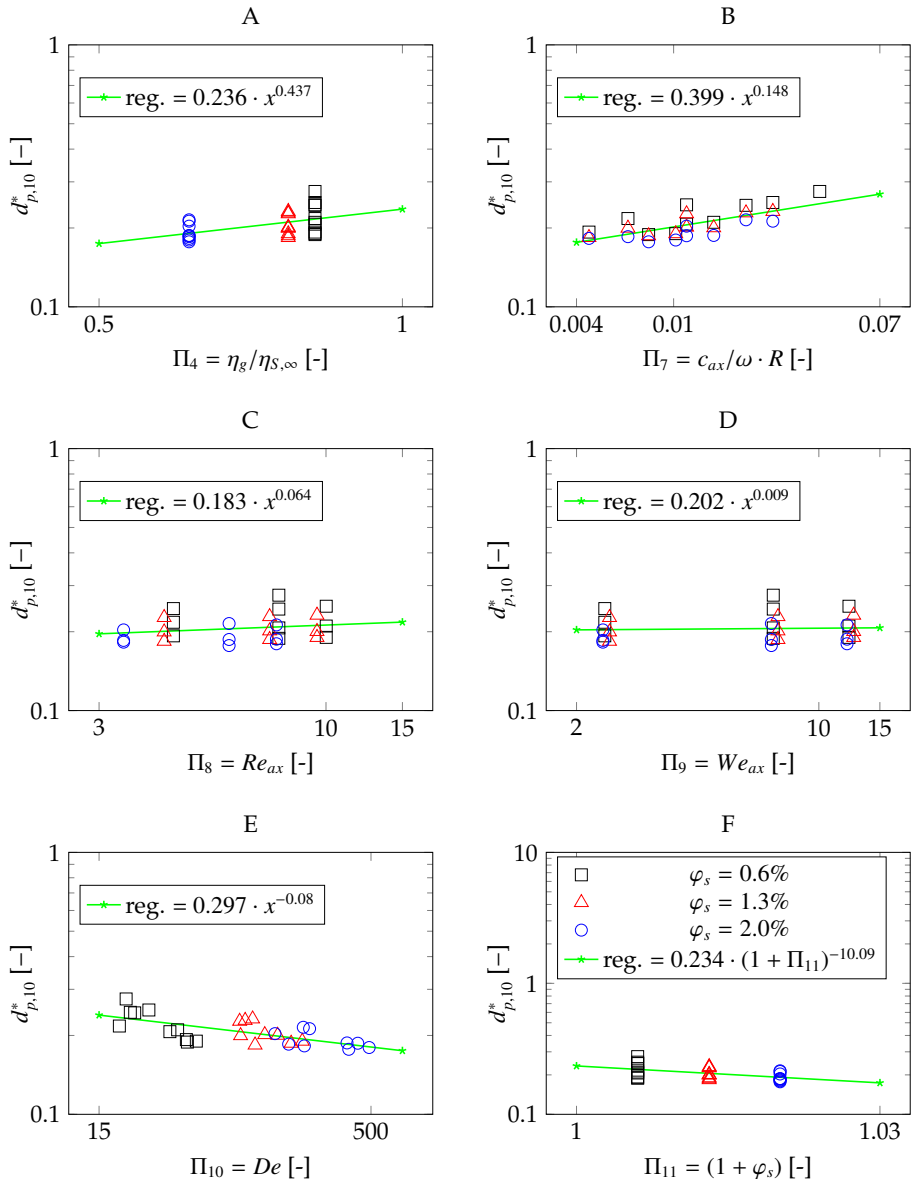

Figure A.8: $d^*_{p,10}$ over Π_i for M_2 with varying aluminum content φ_s as log-log-diagram, including the resulting exponent of the regression functions. $R^2_A = 0.225$, $R^2_B = 0.612$, $R^2_C = 0.039$, $R^2_D = 0.001$, $R^2_E = 0.336$, $R^2_F = 0.256$.

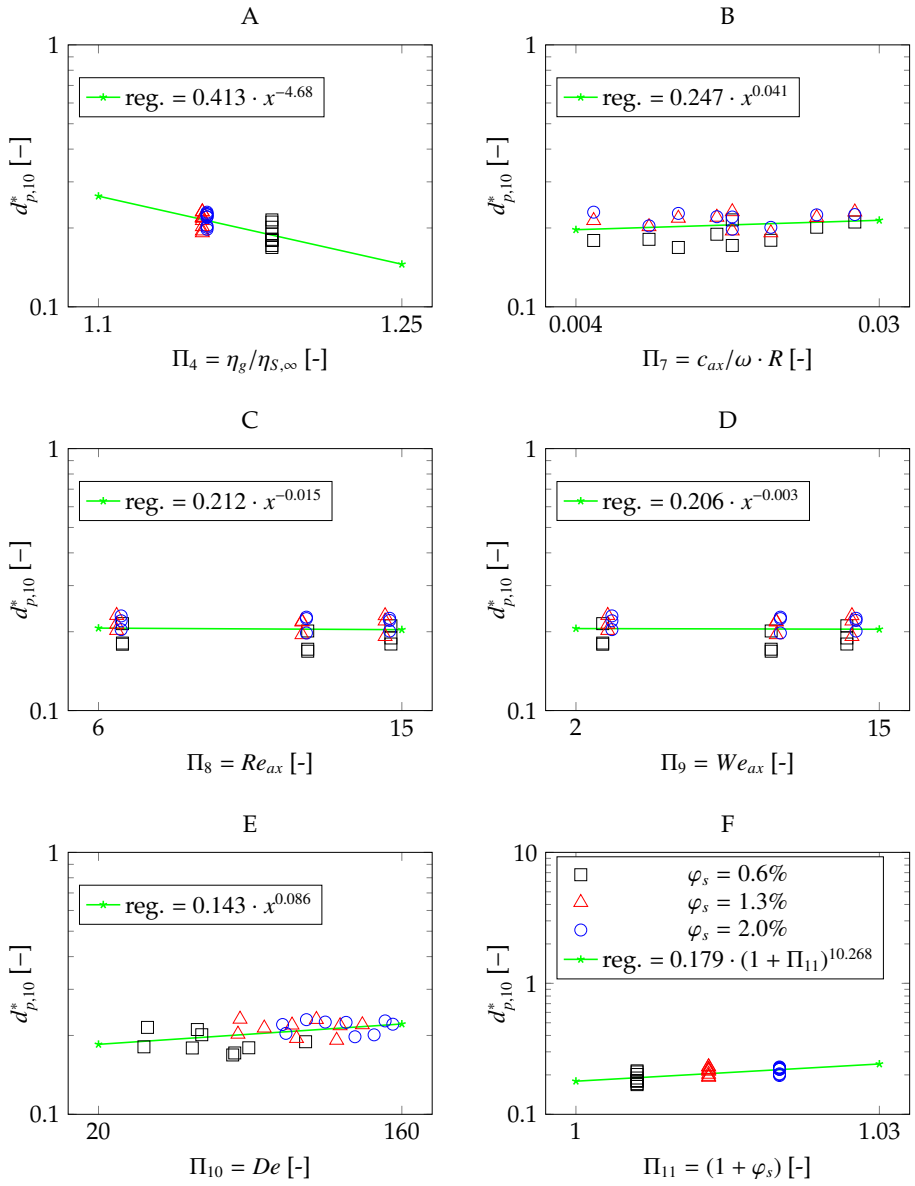

Figure A.9: $d^*_{p,10}$ over Π_i for M_3 with varying aluminum content φ_s as log-log-diagram, including the resulting exponent of the regression functions. $R^2_A = 0.446$, $R^2_B = 0.077$, $R^2_C = 0.002$, $R^2_D = 0.0001$, $R^2_E = 0.181$, $R^2_F = 0.383$.

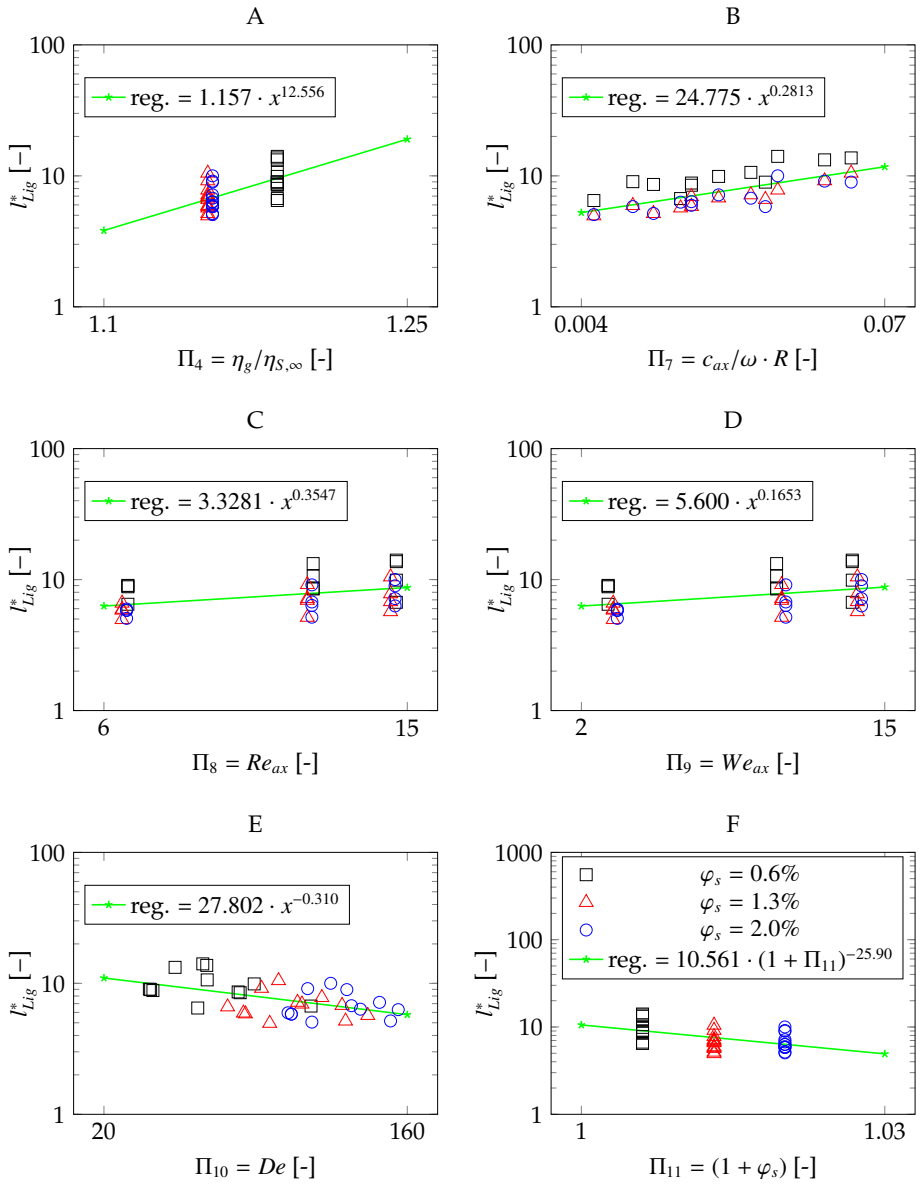

Figure A.10: l^*_{Lig} over Π_i for M_3 with varying aluminum content φ_s as log-log-diagram, including the resulting exponent of the regression functions. $R^2_A = 0.355$, $R^2_B = 0.456$, $R^2_C = 0.176$, $R^2_D = 0.144$, $R^2_E = 0.241$, $R^2_F = 0.268$.

Appendix B

Nomenclature

The following list of symbols contains all abbreviations, symbols, constants and dimensionless groups. Units refer to the dimension-related quantity.

Abbreviations

Abbreviation	Meaning
BSA	burst spectrum analyzer
CaBER	capillary breakup elongational rheometry
cdf	cumulative distribution function
ddf	distribution density function
EPD	electrophoretic disposition
EX	explosive
fps	frames per second
IQR	interquartile range
LDA	laser–Doppler anemometer/anemometry
MLE	maximum likelihood estimator
Nd:YAG	neodymium-doped yttrium aluminum garnet
NT	non–transparent fraction
PDA	phase–Doppler anemometer/anemometry
pdf	probability density function
RACe	robotic application center
RMS	root mean square
SHT	Sterocoll HT
SMD	Sauter mean diameter

SXT	Sterocoll XT
T	transparent fraction
TE	transfer efficiency
TS	time–shift

Greek symbols

Symbol	Explanation	Unit
α	Burr Type XII parameter	–
β	bell inclination angle	$^\circ$
$\dot{\gamma}$	shear rate	1/s
δ	film thickness	m
$\dot{\varepsilon}$	strain rate	1/s
η	dynamic viscosity	Pa s
θ	beam intersection angle	–
κ	exp. intensity decay/absorption coeff.	–
λ	wavelength	m
ξ	Burr Type XII scaling parameter	–
Π	product function	–
ϱ	density	kg/m^3
σ	surface tension	N/m
ς	power–law amplitude factor	–
Σ	sum function	–
$\varphi_{s/air}$	relative solid content/humidity	m^3/m^3
ϕ	light scattering/measurement angle	$^\circ$
Φ	reflected light phase	rad
φ	azimutal coordinate direction	–
ω	bell speed	1/s

Latin symbols

Symbol	Explanation	Unit
a	power–law exponent	–
A	area	m^2
b	power–law exponent	–
B	power–law fluid exponent	–
c	volumetrically averaged flow velocity	m/s

C	concentration	g/m^3
d	diameter	m
D	diameter distribution moment	m
$E(x^j)$	j-th moment of a distribution of x	$[x^j]$
f	function	–
$\vec{g}$	earth gravity vector	m/s^2
ⓖ	gas	–
F	antiderivative	–
h	histogram bin width	m
k	Burr Type XII parameter	–
K	evaporation constant	m^2/s
l	length	m
①	liquid	–
m	index variable	–
n	index variable	–
$\underline{n}$	complex refractive index	–
$\mathfrak{n}$	phase velocity related refractive index	–
N	number, quantity	–
$\vec{n}$	unit normal vector	–
p	quantile variable	–
r	coordinate in radial direction	m
R	bell radius	m
$\vec{r}$	location vector in cylindrical coordinates	m,rad,m
ⓢ	solid	-
t	time	s
$\vec{t}$	unit tangent vector	–
T	temperature	°C
u	velocity component in x/r-direction	m/s
v	velocity component in y/φ-direction	m/s
V	volume	m^3
w	velocity component in z-direction	m/s
$\vec{w}$	velocity vector	m/s
x	coordinate in dir. of propagation, size variable	m
$\vec{x}$	location vector in Cartesian coordinates	m
y	coordinate perpendicular to x and z	m
z	coordinate in plate-perpendicular/axial direction	m

Mathematical symbols

Symbol	Explanation	Unit
$\lceil \dots \rceil$	ceiling function	–
$\lfloor \dots \rfloor$	floor function	–
$\sim$	in the order of	–
$\propto$	proportional to	–
$\dot{x}$	derivative of x with respect to time	$[x]/s$
$\bar{x}$	spatial mean value of x	$[x]$

Superscript and subscript indices

Symbol	Explanation
0	initial state of a variable
∞	bulk value, asymptotic value
avg	average value of a variable
ax	axial
bin	bin related
br	breakup related
cap	capillary related
$count$	count related
$crit$	critical value of a variable
end	ending value of variable
E	elongational
FDR	Freeman-Diaconis Rule
g	in gas
i	index variable
j	index variable
l	in liquid
λ	relaxation time related
Lig	ligament related
lg	liquid-gaseous
max	maximum value of a variable
min	minimum value of a variable
N	number related
p	particle related
rad	radial
s	in solid
S	shear related

$_{Ser}$	serration related
$_{tan}$	tangential
$_{V}$	volume related

Dimensionless Groups

Symbol	Explanation	Unit
De	Deborah number	–
Re	Reynolds number	–
We	Weber number	–

Constants

Constant	Explanation
$g = 9,81\ \mathrm{m/s^2}$	gravitational constant
$\pi \approx 3,141592653589$	

Appendix C

Code

MATLAB code

```
%% start of programm
    clc
    clear all
    close all
    format long eng

 myDir = uigetdir; % gets directory
myFiles = dir(fullfile(myDir,'*.txt')); % Added closing parenthese!
for k = 1:length(myFiles)
    baseFileName = myFiles(k).name;
    fullFileName = fullfile(myDir, baseFileName);  % Changed myFolder to myDir
    fprintf(1, 'Now reading %s\n', fullFileName);



 %% Set parameter input (from txt or UI)
        vm= 2;  %velocity of rotary bell. Not rotary speed! [mm/s]
        lim_1   = 250;
        lim_2   = 150;
        lim_3   = 100;
        cut     = 500;
        cluster = 1;
        incrementx = 1;
        incrementd = 5;
        increment_cont = 1;

        uz=3; %mm/s
```

```
28          vr1=0.2; %über Validationstoleranz vr1-4 öknnen beliebige Streifen ...
                aus dem Phaseplot äausgewhlt werden.
29          vr2=0.00;
30          vr3=vr2;
31          vr4=vr1;
32
33  %         dz1='30k';
34  %         dz2='43k';
35
36  %         q1='350 ml/min';
37  %         q2='350 ml/min';
38
39
40
41
42
43  %% Collecting of input data
44          filename1 = fullFileName; %weist Dateinamen zu
45  %         filename2 = '20170227_2aM1(1)_000002.txt'; %weist Dateinamen zu
46          [filePath,fileName,fileExtension] = fileparts(filename1);
47          fileName    = strrep(fileName,'_Modified','');
48          fileName    = strrep(fileName,'_T','');
49  %% Preparation of output data
50          location    = 'E:\Stick\Sterocoll\';
51          excel       = fullfile(location,'Output.xlsx');
52          histogramd  = strcat(location, 'probabilitesd_', fileName);
53          histogramw  = strcat(location, 'probabilitesw_', fileName);
54          histogramv  = strcat(location, 'probabilitesv_', fileName);
55          dvsw    = strcat(location, 'dvsw_', fileName);
56          tvs     = strcat(location, 'tvs_', fileName);
57          xvsd    = strcat(location, 'xvsd_', fileName);
58          xvsw    = strcat(location, 'xvsw_', fileName);
59          xvs     = strcat(location, 'xvs_', fileName);
60          intervalsx = strcat(location, 'intervalsx_', fileName);
61          countf   = strcat(location, 'count_', fileName);
62          cont    = strcat(location, 'cont_', fileName);
63          intervalsd = strcat(location, 'intervalsd_', fileName);
64          intervalsv = strcat(location, 'intervalsv_', fileName);
65          decrease = strcat(location, 'decrease_', fileName);
66          cutter  = strcat(location, 'cutter_', fileName);
67  %%%%%%%%%%%%%%%%%%%%%%%%%%%%%%%%%%%%%%%%%%%%%%%%%%%%RECHNUNG ANFANG%%%%%%%%%%%%%%%%%%%%%%%%%%%%%%%%%%%%%%%%%%%%%%%%%%%%
68
69          fid3 =   fopen( filename1, 'r');
70          info    = textscan(fid3,'%s %s %s','Headerlines',3);
71          Zerstaeuber = 'Eco2';
72          Duese = '1,3mm';
73          LLring = '40';
74          Glocke = info{1,1}{2,1};
75          Glocke=strtok(Glocke,'e');
76          LL = info{1,2}{1,1};
77          [token_LL,remain_LL] =strtok(LL,';');
```

```
78          LL = remain_LL;
79          LL = LL(2:4);
80          DZ = info{1,3}{1,1};
81          [token_DZ,remain_DZ] =strtok(DZ,';');
82          DZ = remain_DZ;
83          DZ = DZ(2:3);
84          LM = info{1,1}{1,1};
85          [token_LM,remain_LM] =strtok(LM,';');
86          LM = remain_LM;
87          LM = LM(2:4);
88
89
90
91  if vr1<vr2 || vr4<vr3
92     error('Warnung: Wenn vr1<vr2 oder vr4<vr3 werden im jeweiligen Streifen ...
           keine Werte ausgelesen'),
93  end
94
95     atotal=2.5625;   %Steigung der Phaseplotgeraden, optisch ausgelesen
96     Δ=360;      %das Δü ber und unter der Phaseplotgeraden
97
98
99
100    fid1 =   fopen( filename1, 'r');
101
102
103    data1=textscan(fid1, '%f %f %f %f %f %f %f', 'headerlines', 6);
104
105
106        num1    = data1{1,1};
107        t01     = data1{1,2};
108        tt1     = data1{1,3};
109        v1      = data1{1,4};
110        P121    = data1{1,5};
111        P131    = data1{1,6};
112        d1      = data1{1,7};
113        count1  = nnz(d1(:,1));
114
115 %        num2    = data2{1,1};
116 %        t02     = data2{1,2};
117 %        tt2     = data2{1,3};
118 %        v2      = data2{1,4};
119 %        P122    = data2{1,5};
120 %        P132    = data2{1,6};
121 %        d2      = data2{1,7};
122 %        count2  = nnz(d2(:,1));
123
124    fclose('all');
125
126
127
```

```
128       [n1,m1]=size(t01);
129 %       [n2,m2]=size(t02);
130
131       tmin1=t01(1);
132       t1=t01(:)-tmin1;
133       r1=uz*1e-3*t1(:);
134       tmax1=t1(n1);
135       rmax1=tmax1*1e-3*uz;
136       moved1    = tmax1*uz;
137       RW01=[r1 v1 d1 t1 tt1 P121 P131];
138       [nn1,mm1]=size(P121);
139       RW11=zeros(n1,7);
140
141                 for j1=1:nn1
142
143             if (P121(j1,1)<atotal*P131(j1,1)+vr1*Δ && ...
                    P121(j1,1)>atotal*P131(j1,1)+vr2*Δ) || ...
                    (P121(j1,1)<atotal*P131(j1,1)-vr3*Δ && ...
                    P121(j1,1)>atotal*P131(j1,1)-vr4*Δ) && P131(j1,1)>0 && P121(j1,1)>0
144                 RW11(j1,:)=RW01(j1,:);
145
146             else
147               1;
148             end
149
150
151                 end
152
153
154             RW31=[RW11(:,3) RW11(:,2) RW11(:,4)];  %Matrix die alle Daten äenthlt
155             RW31( all(¬RW31,2), : ) = []; % Remove zero rows
156
157
158
159 %       tmin2=t01(1);
160 % %       t2=t02(:)-tmin2;
161 %       r2=uz*1e-3*t2(:);
162 %       tmax2=t2(n2);
163 %       rmax2=tmax2*1e-3*uz;
164 %       moved2    = tmax2*uz;
165 %       RW02=[r2 v2 d2 t2 tt2 P122 P132];
166 %       [nn2,mm2]=size(P122);
167 %       RW12=zeros(n2,7);
168
169
170
171 %           for j2=1:nn2
172 %
173 %           if (P122(j2,1)<atotal*P132(j2,1)+vr1*Δ && ...
        P122(j2,1)>atotal*P132(j2,1)+vr2*Δ) || ...
```

```
        (P122(j2,1)<atotal*P132(j2,1)-vr3*Δ && ...
        P122(j2,1)>atotal*P132(j2,1)-vr4*Δ) && P132(j2,1)>0 && P122(j2,1)>0
174 %               RW12(j2,:)=RW02(j2,:);
175 %
176 %           else
177 %             1;
178 %           end
179 %
180 %
181 %           end
182 %
183 %
184 %           RW32=[RW12(:,3) RW12(:,2) RW12(:,4)];  %Matrix die alle Daten äenthlt
185 %           RW32( all(~RW32,2), : ) = []; % Remove zero rows
186 %
187       dv1 = RW31(:,1);
188       vv1 = RW31(:,2);
189       tv1 = RW31(:,3);
190       rv1 = uz*1e-3*tv1(:);
191       v_abs1 = abs(vv1);
192       n12=length(dv1);
193
194
195 %       dv2 = RW32(:,1);
196 %       vv2 = RW32(:,2);
197 %       tv2 = RW32(:,3);
198 %       rv2 = uz*1e-3*tv2(:);
199 %       v_abs2 = abs(vv2);
200 %       n22=length(dv2);
201
202
203       collector1    = [dv1 vv1 tv1 rv1];
204
205           viglobal1     = collector1(:,1).^3*pi/6;
206           siglobal1     = collector1(:,1).^2*pi;
207           D32mean1      = 6*(sum(viglobal1)/sum(siglobal1));
208           D10mean1      = mean (collector1(:,1)); %d 1 0
209           Dmedian1      = median (collector1(:,1));
210           D30mean1      = (sum(viglobal1)/n12)^(1/3);
211           deviationd1   = std(collector1(:,1));
212           deviationv1   = std(collector1(:,2));
213           varianced1    = var(collector1(:,1));
214           variancev1    = var(collector1(:,2));
215           d101          = prctile(collector1(:,1),10);% d 10
216           d501          = prctile(collector1(:,1),50);
217           d901          = prctile(collector1(:,1),90);
218           v101          = prctile(collector1(:,2),10);
219           v901          = prctile(collector1(:,2),90);
220           count_tol1    = n12;
221           count_svr           = count_tol1/count1;
222
```

```
223 if count_tol1 > 400;
224
225 x_burr= dv1+0.001;
226 pd = fitdist(x_burr,'burr');
227
228 alpha = pd.ParameterValues(1);
229 c = pd.ParameterValues(2);
230 k = pd.ParameterValues(3);
231
232 max_dv1 =max(dv1);
233 h_0 = max_dv1/(2*count_tol1^(1/3));
234 n_0=round(max_dv1/h_0,0);
235 hist_1 = histcounts(x_burr,n_0);
236 hist_fd = histcounts(x_burr,'BinMethod','fd');
237 N_fd=length(hist_fd);
238 h_fd=max_dv1/N_fd;
239
240 hist_1_inv = histcounts(x_burr,n_0).';
241 hist_fd_inv = histcounts(x_burr,'BinMethod','fd').';
242 end
243         d       = dv1;
244         w       = vv1;
245         t       = tv1*1e-3;
246         data    = [d w t];
247         d       = data(:,1);
248         w       = abs(data(:,2));
249         t       = data(:,3);
250         v       = d.^3*pi/6;
251
252         [n,m]=  size(d);
253         wm=uz;
254
255 % basic calculation
256         moved   = max(t)*wm;
257         x       = t*wm;
258         collector   = [d w t x];
259
260         deviationd  = std(d(:,1));
261         deviationw  = std(w(:,1));
262         varianced   = var(d(:,1));
263         variancew   = var(w(:,1));
264         d10         = prctile(d(:,1),10);% d 10
265         d50         = prctile(d(:,1),50);
266         d90         = prctile(d(:,1),90);
267         w10         = prctile(w(:,1),10);
268         w90         = prctile(w(:,1),90);
269
270
271         % Cutter-Data
272         ci      = zeros(10,1);
273         share   = zeros(10,1);
```

```
274         d32c    = zeros(10,1);
275         d30c    = zeros(10,1);
276         dmc     = zeros(10,1);
277         d10c    = zeros(10,1);
278         vic     = zeros(10,1);
279         sic     = zeros(10,1);
280         countc  = zeros(10,1);
281
282         for i=1:10;
283             ci(i,1)     = cut*i/10;
284 %             ci(i,1)     = max(d)*i/10;
285             share(i,1)  = i/10;
286             cutteri     = [d w];
287             cutteri (cutteri(:,1)> ci(i,1) )=0;
288             cutteri (cutteri(:,1) == 0, :) = [];
289             countc(i,1)       = nnz(cutteri(:,1));
290             vic(i,1)    = sum(cutteri(:,1).^3*pi/6);
291             sic(i,1)    = sum(cutteri(:,1).^2*pi);
292             d32c(i,1)   = 6*(vic(i,1)/sic(i,1));
293             d10c(i,1)   = mean (cutteri(:,1)); %d 1 0
294             dmc(i,1)    = median (cutteri(:,1));
295             d30c(i,1)   = (vic(i,1)/countc(i,1))^(1/3);
296         end
297
298 %% Ausgabe in Excel
299         %Closes all Excel applications!
300         try
301             exHandle = actxGetRunningServer( 'Excel.Application' );
302             exHandle.Quit;
303             delete(exHandle)
304         catch MExc
305             disp('Excel is not running')
306         end
307
308         %Generates Design
309         linea = {'Sample','Zerstaeuber','Duese','LL-Ring','Glocke','LL'
310         ,'DZ','LM',[],[],[],[],[],[],[],[],[],[],[],[],[],[],[],[],
311         [],[],[],[],[],[]}; %31 Elemente
312         lineb = {fileName,Zerstaeuber,Duese,LLring,Glocke,LL,DZ,LM,
313         [],[],[],[],[],[],[],[],[],[],[],[],[],[],[],[],[],[],[],[],
314         [],[],[]}; %31 Elemente
315         line1 = {'counts','d_{10} [$\mu$m]','d_{30} [$\mu$m]','d_{32} [$\mu$m]',
316         'd_{median} [$\mu$m]',[],'std_d [-]','std_w [-]','var_d [-]',
317         'var_w [-]','d_{10} [$\mu$m]','d_{50} [$\mu$m]','d_{90} [$\mu$m]',
318         'w_{10} [m/s]','w_{90} [m/s]',['alpha'],['c'],['k'],['h_0'],
319         ['h_fd'],[],[],[],[],[],[],[],[],[],[],[]}; %31 Elemente
320         line2 = {n,d10c(10,1),d30c(10,1),d32c(10,1),dmc(10,1),[],
321         deviationd,deviationw,varianced,variancew,d10,d50,d90,w10,
322         w90,alpha,c,k,h_0,h_fd,[],[],[],[],[],[],[],[],[],[],[]};
323         empty = {[],[],[],[],[],[],[],[],[],[],[],[],[],[],[],[],[],
324         [],[],[],[],[],[],[],[],[],[],[],[],[],[],[]}; %31 Elemente
```

```
325         line3 = {'d [$\mu$m]','w [m/s]','t [s]','x [mm]',[],'class [-]',
326         'd_{10,x} [$\mu$m]','d_{30,x} [$\mu$m]','d_{32,x} [$\mu$m]','d_{v50}',
327         'd_{median,x} [$\mu$m]',[],'time [s]','counts [-]',[],'P(d) [-]',
328         'P(w) [-]',[],'share [-]','d_{10,c} [$\mu$m]','d_{30,c} [$\mu$m]',
329         'd_{32,c} [$\mu$m]','d_{m,c} [$\mu$m]','count_c',[],'interval',
330         'd_{10,d} [$\mu$m]','d_{30,d} [$\mu$m]','d_{32,d} [$\mu$m]','d_{m,d} ...
                [$\mu$m]',
331         'count_d'}; %31 Elemente
332         design = [linea;lineb;line1;line2;empty;line3];
333
334         try %check if path is existing
335             xlswrite(excel, design, fileName, 'A1:AE6')
336         catch ME
337             disp (['Error in path:',excel]);
338         end
339
340         xlswrite(excel, d, fileName, 'A7')
341         xlswrite(excel, w, fileName, 'B7')
342         xlswrite(excel, t, fileName, 'C7')
343         xlswrite(excel, x, fileName, 'D7')
344          xlswrite(excel, hist_1_inv, fileName, 'P7')
345          xlswrite(excel, hist_fd_inv, fileName, 'Q7')
346
347 %%%
348 %%%          disp 'Excel done';
349
350 %% Is this the End?
351         disp 'Ende';
352         end
```